

University of São Paulo
Faculty of Philosophy, Sciences and Letters of Ribeirão Preto
Department of Physics

**Study and evaluation of correction factors applied to
ionization chambers in radiotherapy photon beams**

Corrected version

Cristiano Queiroz Melo dos Reis

Ribeirão Preto - SP
Brazil

2015

Universidade de São Paulo

Faculdade de Filosofia Ciências e Letras de Ribeirão Preto

Departamento de Física

Estudo e avaliação de fatores de correção aplicados a câmaras de ionização em feixes de fótons radioaterápicos

Versão corrigida

Cristiano Queiroz Melo dos Reis

Ribeirão Preto - SP
Brasil

2015

Cristiano Queiroz Melo dos Reis

**Study and evaluation of correction factors applied to
ionization chambers in radiotherapy photon beams**

Corrected version

A thesis submitted to the Graduate Program of
Physics Applied to Medicine and Biology, of the
Faculty of Philosophy, Sciences and Letters of
Ribeirão Preto, University of São Paulo, in par-
tial fulfilment of the requirements for the degree
of Doctor of Philosophy - Search Field: Physics
Applied to Medicine and Biology

Supervisor: Prof. Dr. Patrícia Nicolucci

Ribeirão Preto - SP
Brazil

2015

I AUTHORIZE THE REPRODUCTION AND TOTAL OR PARTIAL
DISCLOSURE OF THIS THESIS, BY ANY CONVENTIONAL OR
ELECTRONIC MEANS, FOR PURPOSES OF STUDY AND RESEARCH,
PROVIDED THAT THE SOURCE IS MENTIONED.

CATALOGUE FORM

Reis, Cristiano Queiroz Melo.

Study and evaluation of correction factors applied to ionization chambers in
radiotherapy photon beams.

Ribeirão Preto, 2015.

195p. : il.; 30 cm

Thesis submitted to the Department of Physics of the Faculty of Philosophy,
Sciences and Letters of Ribeirão Preto, University of São Paulo.

Search Field: Physics Applied to Medicine and Biology

Supervisor: Patrícia Nicolucci

1. Radiotherapy 2. Dosimetry 3. Beam quality correction factor 4. Monte
Carlo simulation.

DEDICATION

This document is dedicated to my wife,
Karla, who has been a great companion throughout my journey.

I am eternally thankful for her love, patience and dedication.

It is also dedicated to my family,
especially my parents *Marlúcia* and *José*, and my in-laws, *Martha* and *Alberto*
(in memoriam). I am totally thankful for having your bet, trust and love.

ACKNOWLEDGEMENTS

First and foremost I would like to express my sincere appreciation to my supervisor, **Dr. Patrícia Nicolucci**, for the valuable teachings and guidance in this study and without whose support this research project would not have been accomplished. I want to thank her for having me since my undergraduate research until the conclusion of this Ph.D. project. It has been a pleasure to be her student and to learn with her. She has all my respect and I am eternally grateful for her attention, dedication and patience through all my researcher career.

I would also like to thank my supervisor in Canada, **Dr. David W. O. Rogers**, who gave me an opportunity to work with him during the sandwich-period of my Ph.D. at Carleton University in Canada. I am grateful for his kindness, patience and dedication. His guidance was very important for developing a significant part of this study. It has been a great pleasure to work and to learn with such an admirable person.

I also had the amazing opportunity to work closely with several people at the Carleton Laboratory for Radiotherapy Physics (CLRP) of the Physics Department of Carleton University. I want to thank the professors **Dr. Rowan Thomson** and **Dr. Gabriel Sawakuchi** for the warm and supportive welcome to the extremely cold Canadian winter. I also want to thank my colleagues there, **Bryan Muir**, **Leila Lukhumaidze**, **Manuel Rodriguez**, **Martin Martinov**, **Marielle Lesperance**, **Justin Sutherland**, **Nima Sherafati** and **Victor Malkov**. I want to thank them for their help and valuable discussions. In particular, I want to thank **Bryan Muir**

for the help with `egs_chamber` user code and for helpful comments and suggestions to this research. I also want to thank the Systems and Network Administrator **Bill Jack** with issues about using the computer cluster at Carleton.

I want to thank our Brazilian friends in Canada, **Caio, Evelen, Adriano** and **Karla** for the amazing moments that we shared together. They made our stay there much more happy and funny. Their friendship is one of the great treasures that we brought from there. I also want to thank our dear Canadian friend **Ivy** who was a great support and helped us with the challenge in the new country. We are also very happy for having her friendship.

I would like to thank the staff and professors of the Physics Department (DFM) of the Faculty of Philosophy, Science and Letters of Ribeirão Preto (FFCLRP) of the University of São Paulo (USP) for the support and teachings during my Ph.D.. In particular, I would like to thank the professors **Dr. Luciano Bachmann** and **Dr. Thomaz Gillardi Neto** for supporting me with references letter to professor David Rogers. I also want to thank the secretary of Physics Department, **Nilza Leone**, for her attention and kindness, and the system analyst **Ali Taha Faiez** with issues about the use of the Educational Computer Cluster of the Computer Centre of Ribeirão Preto (CIRP) of the University of São Paulo.

I wish to thank all of my colleagues and friends of our research group Monte Carlo Simulation Applied to Radiotherapy (SMART) at the Instrumentation Centre on Dosimetry and Radiation Protection (CIDRA) of the Physics Department. I thank **Mirko, Thatiane, Franciely, Mairon, Gustavo, Laura, Eduardo** and **Ana Luiza**, for the company and valuable discussions. In particular I would like to thank

Dr. Cassiana Viccari Saciloto for all the support and friendship.

I also wish to thank my dear friends **Carolina, Luís Alberto, Davidson, Sandra** and **Gustavo** for the friendship, joy and help in difficult time.

I would like to thank **my whole family**, who was the greatest and permanent support during this research. To my lovely wife **Karla**, for her patience and support while this project was in progress. To my mother **Marlúcia**, my father **José**, and my siblings **Ana Paula** and **Fabiano**. To my in-laws **Martha, Alberto** (in memoriam), **Paola** and **Cristian**. To my wonderful nephews, **Gabriel, Felipe, Mateo** and my godson **Enzo**, who have brought lots of happiness to my life. Thank you all of you for the love and bet.

Finally, I want to thank the **Brazilian Federal Agency for Support and Evaluation of Graduate Education(CAPES)** which supported me with a scholarship in order to conduct part of my doctoral research as a visiting graduate student at Carleton University.

EPIGRAPH

A poet once said, "The whole universe is in a glass of wine". We will probably never know in what sense he meant that, for poets do not write to be understood. But it is true that if we look at a glass of wine closely enough we see the entire universe. There are the things of physics: the twisting liquid which evaporates depending on the wind and weather, the reflections in the glass, and our imagination adds the atoms. The glass is a distillation of the earth's rocks, and in its composition we see the secrets of the universe's age, and the evolution of stars. What strange array of chemicals are in the wine? How did they come to be? There are the ferments, the enzymes, the substrates, and the products. There in wine is found the great generalization: all life is fermentation. Nobody can discover the chemistry of wine without discovering, as did Louis Pasteur, the cause of much disease. How vivid is the claret, pressing its existence into consciousness that watches it! If our small minds, for some convenience, divide this glass of wine, this universe, into parts - physics, biology, geology, astronomy, psychology, and so on - remember that nature does not know it! So let us put it all back together, not forgetting ultimately what it is for. Let it give us one more final pleasure: drink it and forget it all!

Richard Feynman

ABSTRACT

The use of a beam quality correction factor, k_{Q,Q_0} is needed in dosimetry of radiotherapy beams for correcting differences between chamber responses at the calibration beam quality, Q_0 and at the quality beam of the user, Q . The purpose of this study is to determine the beam quality correction factor for the NE2571 ionization chamber widely used in radiotherapy and its dependence with the stopping-power and the chamber perturbation factors. In addition, an investigation of the use of parallel plate chambers for determining surface doses in photon beams is also performed using the EGSrnc Monte Carlo code system. Results obtained with PENELOPE shows that simulations with phase-space files appropriately scored can be up to ten times shorter than using a full spectrum in the input-file. Values of k_{Q,Q_0} and its components show good agreement with published values in the literature and are provided with typical statistical uncertainties of 0.2%. Values of k_{Q,Q_0} and absorbed dose to water conversion factors obtained with egs_chamber user code for parallel plate chambers are also provided with maximum statistical uncertainty of 0.7%. Therefore, the results obtained are expected to contribute with improving dosimetry protocols and the quality of life of radiotherapy patients.

Key-words: Radiotherapy, dosimetry, beam quality correction factor, surface doses, Monte Carlo simulations.

RESUMO

O uso de uma fator de correção para a qualidade do feixe, k_{Q,Q_0} , é necessário em dosimetria de feixes radioterápicos para a correção das diferenças entre a resposta de câmaras de ionização nas qualidades do feixe de calibração, Q_0 e do usuário Q . O propósito deste trabalho consiste em determinar o fator de correção da qualidade de feixe para a câmara de ionização NE2571 amplamente utilizada em radioterapia e sua dependência com o *stopping-power* e os fatores de perturbação da câmara. Além disso, uma investigação do uso de câmaras de placas paralelas para determinar doses na superfície em feixes de fótons é também realizada usando o sistema de códigos em Monte Carlo EGSnrc. Resultados obtidos com o PENELOPE mostram que simulações usando *phase-space*, podem ser cerca de dez vezes menos longa do que simulações usando um espectro completo no arquivo de entrada. Valores de k_{Q,Q_0} e suas componentes mostraram boa concordância com dados publicados na literatura e são fornecidos com incertezas estatísticas típicas de 0.2%. Valores de k_{Q,Q_0} e fatores de conversão pra dose absorvida na água obtidos para as câmaras de placas paralelas com o código de usuário egs_chamber são também fornecidos com incerteza estatística máxima de 0.7%. Deste modo, espera-se que os resultados obtidos possa contribuir com o aperfeiçoamento de protocolos de dosimetria e com a qualidade de vida de pacientes radioterápicos.

Palavras-chave: Radioterapia, dosimetria, fator de correção da qualidade do feixe, doses em superfície, simulação Monte Carlo.

TABLE OF CONTENTS

CATALOGUE FORM	iv
DEDICATION	v
ACKNOWLEDGEMENTS	vi
EPIGRAPH	ix
ABSTRACT	x
RESUMO	xi
LIST OF TABLES	xiv
LIST OF FIGURES	xviii
1 Introduction	1
1.1 General Introduction	1
1.2 Reference dosimetry	2
1.3 Surface dosimetry	3
1.4 Purposes	8
2 Theory	9
2.1 Dosimetry quantities and equilibrium conditions	9
2.1.1 Absorbed dose vs KERMA	9
2.1.2 Radiation and charged particle equilibrium	12
2.2 Cavity Theory	19
2.2.1 Bragg-Gray cavity theory	20
2.2.2 Spencer-Attix cavity theory	22
2.2.3 Cavity theory vs. ion chambers: Correction factors	26
2.3 Ionization chambers	32
2.4 Clinical dosimetry	37
2.4.1 Theoretical determination of k_{Q,Q_0}	39

2.5	Absorbed dose determination with extrapolation chambers	43
2.6	Monte Carlo simulations	45
2.6.1	Condensed vs Detailed simulations	49
2.6.2	Class-I and class-II algorithms	51
2.6.3	Monte Carlo codes	52
3	Methodology	67
3.1	Calculations of k_Q for reference dosimetry using PENELOPE	67
3.1.1	Parameters and features of PENELOPE code	67
3.1.2	Radiation sources and the TPR_{10}^{20} beam quality specifier	68
3.1.3	Phase space file methodology for reducing time simulations	69
3.1.4	Restricted stopping-power calculations	70
3.1.5	Absorbed doses and correction factors calculations	71
3.2	Buildup and surface calculations using the EGSnrc system	77
3.2.1	Radiation sources	77
3.2.2	Calculation of surface water depth doses	79
3.2.3	Evaluation of extrapolation chambers response	80
3.2.4	Monte Carlo dose conversion factors for parallel plate chambers	83
4	Results and Discussions	88
4.1	k_Q and correction factors calculations with PENELOPE	88
4.1.1	The TPR_{10}^{20} beam quality specifier	88
4.1.2	Phase space file vs Beam simulations	91
4.1.3	Restricted stopping power ratio	92
4.1.4	Perturbation and beam quality correction factors	94
4.2	Buildup and surface dose calculations with EGSnrc system	108
4.2.1	Surface depth dose curves	108
4.2.2	Extrapolation chamber responses	112
4.2.3	Parallel plate chamber dose conversion factors	125
5	Conclusions	147
	Appendix A: MATLAB program for calculating average restricted stopping power ratios	148
	REFERENCES	157

LIST OF TABLES

Table	page
3-1 Beam quality specifiers for the Elekta SL25 and ^{60}Co Eldorado 6 full BEAMnrc models. Values of $\%dd(10)_x$ are calculated using DOSRZnrc code, and TPR_{10}^{20} are calculated with Kalach and Rogers formula.	78
3-2 Physical characteristics of the extrapolation chambers modelled in this study according to data from the literature. The chambers are designated here as ExCh 1 (Nislon and Montelius) and ExCh 2 (Gerbi and Khan PTW 30-360). Active radius of the cavity in mm are given together with the total (active and guard region) radius in parentheses. The range of electrode separations (s) shown on third column corresponds to the minimum and maximum values used experimentally.	80
3-3 Major dimensions and materials for the four plane-parallel plate ion chambers investigated in this study. The radius of the active region of the chambers are given in the fourth column with the total radius (active and guard region) in parenthesis. Chamber materials are MYLAR, graphite (Gr, 1.7 g/cm ³ density), rexolite (cross-linked polystyrene, Rex), air-equivalent plastic (C552), polyoxymethylene (POM, trade name Delrin), polystyrene-equivalent plastic (D400), Kapton and polymethylmethacrylate (PMMA). The abbreviation Gr'd refers to a graphited material, i.e., a thin layer of graphite applied to the material in question.	84

4-1	The photon component of the percentage depth-dose at 10 cm depth ($\%dd(10)_x$) for a 10 x 10 cm ² field on the surface of the water phantom as a beam quality specifier for the radiation sources used in this study. Our calculated values (third column) are compared with those obtained by Muir and Rogers (fourth column) and Wulff <i>et al.</i> (last column). The relative difference with our values are shown between parentheses. Maximum relative statistical uncertainties on Muir and Rogers and Wulff <i>et al</i> values are 0.1% and 0.3% respectively.	89
4-2	Radiation sources and Monte Carlo calculated TPR_{10}^{20} quality specifier for the 5 energy beams used in this study. Comparisons are made between our results (third column) and those obtained by other authors that used the same energy spectra. The values between parentheses represent the relative percentage difference with our values. Our results were obtained from the calculated $\%dd(10)_x$ presented in table 4-1 and using equation 3.1.	90
4-3	Absorbed energies to water calculated in a disc with 1.0 cm radius and 0.025 cm thickness at and SSD = 100 using a full spectrum beam and a phase space file (psf) in PENELOPE input-files.	92
4-4	Monte Carlo calculated k_Q factors for the NE2571 ion chamber and differences to results found in the literature. Fitting curves provides the values of k_Q for the same TPR_{10}^{20} used in this study. The uncertainties to our calculated values are shown in parentheses besides each value.	105
4-5	Fit parameters to a cubic polynomial of type $k_Q = a + b (TPR_{10}^{20}) + c (TPR_{10}^{20})^2 + d (TPR_{10}^{20})^3$ for calculating k_Q values as a function of the TPR_{10}^{20}	106
4-6	Surface ($z = 0.5 \mu\text{m}$) and skin depth ($z = 0.07 \text{ mm}$) percentage depth doses for high energy photon beams with and without contaminant electrons. Values are normalized by the maximum dose without contaminant electrons. Statistical uncertainties in brackets are in the last digits.	111

4-7 Surface ($z = \text{EPOM}$) relative doses in polystyrene phantom for a $10 \times 10 \text{ cm}^2$ field in ^{60}Co , 6 MV, 10 MV and 25 MV beams. The first column shows the experimental values considered to be extrapolated by Nilson and Montelius [1] ($z = 0.01 \text{ mm}$) and Gerbi and Khan [2] ($z = 0.03 \text{ mm}$). The values calculated with the `egs_chamber` user code (second column) for the respective chambers in polystyrene using 0.1 mm plate separation were considered as the extrapolated values for the respective chambers. The percentage dose to the medium ($\%D_{med}$) values were also calculated with the same MC code and are shown in the last column at the corresponding depths (front window) of the chambers for comparison. 124

4-8 Dose ratio D_w/D_{ch} and perturbation factors for parallel plate chambers in ^{60}Co beam. The values were averaged over the depths $0.5 \text{ cm} \leq z \leq 1.1 \text{ cm}$ in a $30 \times 30 \times 30 \text{ cm}^3$ water phantom. 127

4-9 Dose ratio D_w/D_{ch} and perturbation factors for parallel plate chambers in 6, 10 and 25 MV beams. The values were averaged over the depths beyond the depths of maximum dose (z_{max}) for each beam in a $30 \times 30 \times 30 \text{ cm}^3$ water phantom. Depths of maximum dose were found to be on average 1.5 cm, 2.3 cm and 3.7 cm for 6, 10 and 25 MV beams respectively. 133

4-10 Fitting parameters for equation 4.7 for providing D_w/D_{ch} conversion factors in the buildup region of ^{60}Co , 6 MV, 10 MV and 25 MV beams. The corresponding rms deviation of the data from the fit are given in percentage in the last column. The fits are valid for depths $z \geq 0.113 \text{ cm}$, and 0.26 cm for the Roos and NACP02 chambers respectively. For the Exradin A10 and P11TW fits are valid for depths $z \geq 0.204 \text{ cm}$. The fits also apply until depths z of 1.1 cm, 2.1 cm, 3.1 cm and 6.4 cm for ^{60}Co , 6 MV, 10 MV and 25 MV beams respectively. 135

4-11	Fitting parameters for equation 4.7 for providing surface dose to water conversion factors as a function depth for the Exradin A10 and P11TW parallel plate chambers. The fits are valid for using those chambers at depths z within $0.03 \text{ mm} \leq z \leq 1.03 \text{ mm}$ in solid water phantom in ^{60}Co , 6 MV, 10 MV and 25 MV photon beams.	140
4-12	Dose ratios D_w/D_{ch-SW} for the Exradin A10 and P11TW ion chambers positioned with their EPOM at the skin depth ($z = 0.07 \text{ mm}$) in a solid water phantom. Values were obtained with equation 4.7 and fit parameters given in table 4-11 for each photon beam.	141
4-13	Fitting parameters for equation 4.7 for providing k_Q values at the surface of water phantom from measurements with the Exradin A10 and P11TW ion chambers in solid water. The fit is valid for using the chambers in depths $0.03 \text{ mm} \leq z \leq 1.03 \text{ mm}$. The rms deviation of the data from the fits are given in percentage in the last column.	146

LIST OF FIGURES

<u>Figure</u>	<u>page</u>
2-1 Schematic representation of the two stage process of transfer of energy to the medium by photons. In (a) a photon with energy $h\nu$ interacts with an electron of the medium and gives it a kinetic energy $h\nu - h\nu'$. This electron will then spend its kinetic energy by emitting bremsstrahlung photons ($h\nu''$) when interacting with atomic nucleus and by collision with other electrons. Relatively violent collisions electron-electron also gives rise delta-ray which is another electron track. Kerma correspond to the transfer of energy at (a) while absorbed dose corresponds to the imparted energy along (b). Adapted from <i>The physics of radiology</i> , Johns and Cunningham, 1983.	10
2-2 Illustration of the definitions of energy transferred, net energy transferred and energy imparted for the case of a photon with energy $h\nu_1$ interacting (via Compton) in a volume V with mass m . The energy transferred, net energy transferred and energy imparted are given respectively by $\epsilon_{tr} = T = h\nu_1 - h\nu_2$, $\epsilon_{tr}^{net} = T - (h\nu_3 + h\nu_4)$ and $\epsilon = h\nu_1 - (h\nu_2 + h\nu_3 + T')$. Reproduced from <i>Introduction to Radiological Physics and Radiation Dosimetry</i> , F. H. Attix, 1986.	12
2-3 Schematic illustration of how kerma and absorbed dose vary with depth in charged particle equilibrium (CPE) in (a) and transient charged particle equilibrium (TCPE) in (b). In (a) a non-realistic situation is considered where the photon beam is not attenuated. In (b) a more realistic situation considers an attenuation of the primary particles of 5% at each depth corresponding to a distance between consecutive squares. Adapted from <i>The physics of radiology</i> , Johns and Cunningham, 1983.	15

2-4	Illustration of transient charged particle equilibrium (TCPE) where absorbed dose (D) is proportional to collision kerma (K_c). TCPE occurs beyond the maximum depth of penetration (t_{max}) of secondary charged particles. Radiative losses are assumed to be absent ($K_r = 0$) and then $K = K_c$. Reproduced from Basic Radiation Interactions, Jeffrey V. et al in <i>Clinical Dosimetry Measurements in Radiotherapy</i> , Rogers and Cygler, 2009.	18
2-5	Determination of D_{med} from D_{det} . Reproduced from Cavity theory, stopping power ratios, correction factors, A. E. Nahum in <i>Clinical Dosimetry Measurements in Radiotherapy</i> , Rogers and Cygler, 2009.	20
2-6	A gas filled cavity in a medium traversed by electron tracks. Reproduced from Cavity theory, stopping power ratios, correction factors, A. E. Nahum in <i>Clinical Dosimetry Measurements in Radiotherapy</i> , Rogers and Cygler, 2009.	23
2-7	Illustration of practical ionization chamber showing its different components that can be a source for Bragg-Gray detector condition deviations. Reproduced from Cavity theory, stopping power ratios, correction factors, A. E. Nahum in <i>Clinical Dosimetry Measurements in Radiotherapy</i> , Rogers and Cygler, 2009.	27
2-8	Illustration of the adoption of an effective point of measurement P_{eff} for cylindrical chambers.(a) The chamber is positioned with its P_{eff} at the reference depth, z_{ref} , and then $P_{gr} = 1.00$. d_c represents the shift for the P_{eff} related to the center of the chamber. If the chamber is positioned with its center in z_{ref} (b), then P_{gr} is not equal 1.00. Reproduced from TRS-398, IAEA, 2001.	29

2-9	Illustration of the electron fluence perturbation effects caused by a low-density material cavity inserted in a phantom with higher density and irradiated by an electron beam. The paths of the electrons are idealized in order to emphasize the effects being shown. The electron tracks that would exist in the absence of the cavity are represented by the dashed lines.(a) The fluence in the cavity is increased compared to the situation without the cavity because the in-scatter effects are dominant over the out-scatter ones.(b) On the other hand, the obliquity effects decreases the fluence in the cavity because the electron paths are shorter (straighter) in a lower-density medium (gas). Reproduced from <i>Introduction to Radiological Physics and Radiation Dosimetry</i> , F. H. Attix, 1986.	31
2-10	Response of an ion chamber as a function of the voltage applied between its electrodes. Reproduced from <i>Ionization Chamber Instrumentation</i> , Larry A. DeWerd et al in <i>Clinical Dosimetry Measurements in Radiotherapy</i> , Rogers and Cygler, 2009.	33
2-11	Simplified representation of an ionization chamber connected to a charge reading electrometer. Reproduced from <i>Ionization Chamber Instrumentation</i> , Larry A. DeWerd et al in <i>Clinical Dosimetry Measurements in Radiotherapy</i> , Rogers and Cygler, 2009	34
2-12	Schematic illustration of a plane parallel plate chamber (a) and a Farmer type (thimble) chamber (b). The electric field is represented by the dashed lines between the electrodes of the chambers. In (a) the nominal volume of the chamber is defined by the separation between the electrode (g), the radius of the collector (r_c) and the radius of the inner edge of the guard (r_g). Reproduced from <i>Ionization Chamber Instrumentation</i> , Larry A. DeWerd et al in <i>Clinical Dosimetry Measurements in Radiotherapy</i> , Rogers and Cygler, 2009.	36
2-13	Compiling and running PENELOPE code.	54

- 2-14 2-D representation of the XCSE technique in *egs_chamber* by showing interaction sites (blue dots) of approximately 500 hundred 6 MeV photons. The box (dashed line) represents a small region inside the water phantom where the cross section is increased by 512. Reproduced from *Medical Physics*, "Efficiency improvements for ion chamber calculations in high energy photon beams", Wulff *et al*, vol 35, pp. 1328 - 1336, 2008. 61
- 2-15 Representation of the combined application of IPSS and XCSE techniques in two positions of an ion chamber inside a phantom. The dashed line box and dashed circles represent the shells of phantom material with enhanced cross sections involving the IPSS volume (solid line box) and chamber (solid line circle) respectively. As soon as the particles get into the IPSS volume their transport is terminated and the phase space of photons and electrons is stored (left). This phase space is then used as a source at the two different positions of the ion chamber (middle and right). However, electrons that do not start inside the XCSE region of the respective ion chamber geometry (dashed circles) must survive a *Russian Roulette* game. We can see from the illustration that IPSS electrons originating from photon A will not survive the game for the first chamber position (middle) and neither electrons from photon B will survive for the second position (right). Reproduced from *Medical Physics*, "Efficiency improvements for ion chamber calculations in high energy photon beams", Wulff *et al*, vol 35, pp. 1328 - 1336, 2008. 63
- 2-16 Representation of the correlated samplig method. Particle *A* represents a main history that is transported only once since it never enter the correlated sampling region (solid line circle). For particle *B* its main history (solid line) is transported only once, and thus only the split history (dashed lines) is repeated for each geometry option. Since the particle enters the CS region with the same parameters in both geometry options, it will follow similar trajectories and quantities (energy deposition) will be highly correlated. Reproduced from *Medical Physics*, "Efficiency improvements for ion chamber calculations in high energy photon beams", Wulff *et al*, vol 35, pp. 1328 - 1336, 2008. 65

3-1	Simulation geometries of the NE2571 farmer chamber built with the PENGEOM package of PENELOPE for calculating correction factors. In (a) a complete geometry of the chamber (for calculating D_{ch}) is shown in comparison with the geometry without electrode (b) (for calculating D_{noel}) and also with the geometry corresponding only to the bare air cavity of the chamber in (c) (for calculating D_{air}).	72
3-2	Comparison of electron energy fluence distributions of the phase space file stored with different numbers of primary histories for ^{60}Co (a), 4 MV (b), 6 MV (c), 10 MV (d) and 25 MV (e) photon beams. . .	75
3-3	Comparison of photon energy fluence distributions of the phase space file stored with different numbers of primary histories for ^{60}Co (a), 4 MV (b), 6 MV (c), 10 MV (d) and 25 MV (e) photon beams. . .	76
3-4	Monte Carlo models of the extrapolation chambers used by Nilson and Montelius (a) which will be referred here as ExCh 1, and the PTW 30-360 used by Gerbi and Khan (b) referred as ExCh 2. Some of its characteristics are given on table 3-2.	81
3-5	Monte Carlo models of the Roos (a), NACP02 (b), A10 (c) and P11TW (d) plane parallel plate chambers created with the geometry viewer package of EGSnrc C++ class library. Main materials that compose the chambers are indicated in the legend with their corresponding density.	85
4-1	Spencer-Attix water to air stopping-power ratios calculated by Monte Carlo simulation. Our values calculated with PENELOPE (black circles) are shown together with a cubic fit (straight line) given by $(\bar{L}/\rho)_{air}^{water} = 1.7736 - 3.1476(TPR_{10}^{20}) + 5.2889(TPR_{10}^{20})^2 - 3.0527(TPR_{10}^{20})^3$ with rms deviation of 0.07%. Data from the fit provided in TRS-398 are shown in red dashed line. A fit from Rogers and Kalach for $TPR_{10}^{20} \geq 0.63$ plus the stopping power ratio for a ^{60}Co beam from Rogers and Yang is also shown (dotted line with blue triangles).	93

- 4-2 Monte Carlo calculated overall perturbation factor for the NE2571 ionization chamber as a function of the beam quality TPR_{10}^{20} . Our data (solid black circles) are shown in comparison with the results from Wulff *et al* (open red squares) and Erazo and Lallena (solid blue triangles). A fit of type $p_Q = a + b * TPR_{10}^{20}$ with $a = 0.952 \pm 0.003$, $b = 0.053 \pm 0.004$ and $r^2 = 0.98$ is given (black straight line). 95
- 4-3 The P_{repl} correction factor which accounts for the combined effect of the dose gradient in the absence of the chamber (P_{grad}) and secondary electron fluence perturbation (P_{fl}). Our results (black solid circles) for the NE2571 ion chamber are shown in comparison with those ones obtained by Wulff *et al* (open red squares) and Wang and Rogers (blue triangles). A linear fit of type $P_{repl} = a + b * TPR_{10}^{20}$ with $a = 0.990 \pm 0.002$, $b = 0.010 \pm 0.002$ and $r^2 = 0.85$ is proposed to our data. 97
- 4-4 The wall perturbation factor for the NE2571 chamber. Our calculated values (solid black circles) for $P_{(wall+sleeve+steam)}$ are shown in comparison with the the values for this same factor from Wulff *et al* (open red squares). The figure also shows the values of $P_{(wall+sleeve)}$ calculated by Wulff *et al* (solid orange squares) and Buckley and Rogers (solid blue triangles). A linear fit $P_{wall} = a + b(TPR_{10}^{20})$ with $a = 0.969 \pm 0.004$, $b = 0.041 \pm 0.006$ and $r^2 = 0.93$ is shown (black straight line) to our data. 99
- 4-5 The central electrode correction factor, P_{cel} , for the NE2571 ionization chamber. Values calculated in this study (solid black circles) are shown in comparison with those ones obtained by Wulff *et al* (open red squares) for the same chamber. A linear fit $P_{cel} = a + b(TPR_{10}^{20})$ with $a = 0.989 \pm 0.01$, $b = 0.007 \pm 0.002$ and $r^2 = 0.83$ is proposed to our data. 102

4-6	The beam quality correction factor for the NE2571 ionization chamber. Data points are from our results (solid black circles), TRS-398 (open squares) and TG-51 (blue triangle up). Fit to Monte Carlo calculated data are from Muir and Rogers (dashed red line), Wulff <i>et al</i> (dotted blue line) and Erazo and Lallena (point dashed orange line). A fit to experimental data compiled by Andreo and given by Wulff <i>et al</i> is also plotted (solid black line) for comparison with Monte Carlo results. Values measured by McEwen are also shown (green triangles down).	103
4-7	Beam quality correction factor, k_Q , and its components for the NE2571 ionization chamber as a function of the TPR_{10}^{20} . The components are given by the ratio in two beam qualities of the water to air restricted stopping power ratio $(SPR)_{60Co}^Q$ and the overall perturbation factor $(P_Q)_{60Co}^Q$, as well as the factors, $(P_{wall})_{60Co}^Q$, $(P_{repl})_{60Co}^Q$, and $(P_{cel})_{60Co}^Q$ assumed to be independent of each other.	107
4-8	Surface percentage depth dose curves for high energy photon beams as a function of depths between 0.5 μm and 0.1 mm in a cylindrical water phantom with 15 cm radius and about 30 cm height. For all energy beams a field of 10 x 10 cm^2 is defined at an SSD = 100 cm. Surface and skin depths are considered to be at $z = 0.5 \mu\text{m}$ and $z = 0.07 \text{ mm}$ respectively. Values are normalized by the maximum dose without electron contamination.	109
4-9	Photon component of the surface percentage depth dose curves shown in figure 4-8. Electron contamination is removed by choosing only photon particles from the beams produced in BEAMnrc simulations and also making ECUT = 30 MeV for the air between the head accelerator and the water phantom in DOSRZnrc. Values are normalized by the maximum photon component dose (without electron contamination).	110
4-10	Simulated (closed symbols) and measured (open symbols) response for the ExCh 1 extrapolation chamber at $z = 0.01 \text{ mm}$ in polystyrene phantom for ^{60}Co (circles) and 6 MV (squares) beam as a function of the electrode separations. Results are normalized to D_{max} obtained with $s = 1 \text{ mm}$. Values of calculated $\%D_{med}$ at $z = 0.01 \text{ mm}$ are also shown (dotted and dashed lines) for comparison.	113

4–11 Monte Carlo calculated values of the replacement perturbation factors, P_{repl} , for the ExCh 1 extrapolation chamber in ^{60}Co (circles) and 6 MV (squares) beams as a function of depth z in the buildup region of a polystyrene phantom. Calculations were done for 2 different electrode separations, $s = 0.1$ mm (open symbols) and $s = 10$ mm (closed symbols).	115
4–12 Difference between the percentage depth ionizations (PDI's) obtained with extrapolation chamber ExCh 2 and a fixed parallel plate Markus chamber in the buildup region in solid water for ^{60}Co (circles) and 25 MV (squares) beams. The over-responses of the Markus chamber are shown as a function of depth z normalized to the depth of maximum dose (z_{max}) for a 10×10 cm ² field at an SSD = 100 cm. Experimental data (open symbols) are from Gerbi and Khan with root-mean-square deviation of about 1%. Monte Carlo calculated data (solid symbol) with egs_chamber were simulated by considering responses of the ExCh 2 chamber with $s = 0.1$ mm as the extrapolated values against the response of the Markus chamber. The blue base line represents null difference (no over-response).	117
4–13 Markus chamber over-response for 6 MV (a) and 10 MV (b) beams when compared to the extrapolated values obtained with the ExCh 2. Monte Carlo calculated data (black solid circles) are compared to experimental data obtained by Gerbi and Khan and Mellenberg. In this study extrapolated data were calculated with $s = 0.1$ mm for the ExCh 2. The blue base line represents no over-response.	119
4–14 Extrapolation chambers responses ($\%D_{gas}$) as a function of the electrode separations with the EPOM at $z = 0.5$ cm depth in polystyrene phantom in a ^{60}Co beam. For each plate separation, s , the responses of the chambers are normalized to their maximum reading at $z = 0.4$ cm. The dashed blue line corresponds to the calculated percentage dose ($\%D_{med}$) value of $99.71\% \pm 0.02\%$ at the corresponding depth in polystyrene.	120

4–15	Percentage depth dose PDD curves for 6 MV (a) and 10 MV (b) photon beams. Data from Pena <i>et al</i> correspond to PDI’s measurements obtained with a PTW30001 ion chamber and multiplied by a Monte Carlo depth dependent conversion factor (D_w/D_{ch}). Extrapolated measurements in solid water with a radiochromic film was used by Butson <i>et al</i> . All the other experimental data as well as our calculated results (black circles) are from extrapolated PDI’s with extrapolation chambers. Monte Carlo calculated PDD’s are also plotted (blue triangle right) for comparison.	122
4–16	Dose to water conversion factor (D_w/D_{ch}) as a function of depth in the buildup region of a water phantom in ^{60}Co beam. Factors are calculated for the Roos (black circles), NACP02 (open red squares), Exradin A10 (solid blue squares) and Exradin P11TW (orange triangles) parallel plate chambers. The water-to-air restricted stopping-power ratio (at reference depth) is also shown for comparison.	126
4–17	Dose to water conversions factors (D_w/D_{ch}) for parallel plate chambers in the buildup region of a 6 MV beam. Values of D_w and D_{ch} were calculated as a function of depth z for each chamber in a 30 x 30 x 30 cm^3 water phantom. The water-to-air restricted stopping-power ratio (at reference depth) is also shown for comparison.	129
4–18	Dose to water conversion factors D_w/D_{ch} for Roos, NACP02, Exradin A10 and P11TW parallel plate chambers as a function of depth in the buildup region of a 10 MV beam. Calculations were done in a 30 x 30 x 30 cm^3 water phantom. The water-to-air restricted stopping-power ratio (at reference depth) is also shown for comparison.	130
4–19	Dose to water conversion factors D_w/D_{ch} for Roos, NACP02, Exradin A10 and P11TW parallel plate chambers as a function of depth in the buildup region of a 25 MV beam. Calculations were done in a 30 x 30 x 30 cm^3 water phantom. The water-to-air restricted stopping-power ratio (at reference depth) is also shown for comparison.	131
4–20	Surface dose to water conversion factor (D_w/D_{ch-SW}) as a function of depth within $0.03 \text{ mm} \leq z \leq 1.03 \text{ mm}$ for the Exradin A10 ion chamber. Curves are for ^{60}Co , 6 MV, 10 MV and 25 MV beams. .	136

4-21	Surface dose to water conversion factor (D_w/D_{ch-SW}) as a function of depth within $0.03 \text{ mm} \leq z \leq 1.03 \text{ mm}$ for the Exradin P11TW ion chamber. Curves are for ^{60}Co , 6 MV, 10 MV and 25 MV beams.	138
4-22	Comparison of surface ($0.03 \text{ mm} \leq z \leq 1.03 \text{ mm}$) dose to water conversion factors (D_w/D_{ch-SW}) for the Exradin A10 and P11TW chambers in ^{60}Co (a), 6 MV (b), 10 MV (c), and 25 MV (d). Values of $(\bar{L}_\Delta/\rho)_{air}^{water}$ as a function of depth are also plotted for comparison.	139
4-23	The beam quality correction factors, k_{Q,Q_0} , as a function of depth calculated as the ratio in two beam qualities (Q and ^{60}Co) of D_w/D_{ch-SW} for the Exradin A10 chamber. Values are shown for different depths within $0.03 \text{ mm} \leq z \leq 1.03 \text{ mm}$ at the surface of the phantom in 6 MV, 10 MV and 25 MV photon beams.	142
4-24	Same as shown in figure 4-23 but now for the Exradin P11TW ion chamber.	144
4-25	Comparison of the values of k_Q as a function of depth obtained for the A10 (solid green circles) and P11TW (open blue squares) ion chambers in 6 MV (a), 10 MV (b) and 25 MV (c) beams. Polynomial fits for the A10 (solid green line) and P11TW (dashed blue line) are shown for providing k_Q values within the range $0.03 \text{ m} \leq z \leq 1.03 \text{ mm}$	145

CHAPTER 1 Introduction

1.1 General Introduction

Radiotherapy consists in using ionizing radiation beams (usually photons or electrons) for treating patients with cancer. However, radiotherapy can cause damage to healthy tissues adjacent to the tumor, which makes it important the accurate knowledge of absorbed doses [3]. The often stated goal is -5% to +7% accuracy in dose deliver to the tumor, which can also be understood as a tolerance for the deviation between the prescribed dose and the dose delivered to the target volume [4, 5].

The accurate knowledge of doses delivered in treatments depends on both the procedures used in clinical reference dosimetry held in radiotherapy services and the calibration standard of the dosimeter used. According to international dosimetry protocols such as the TRS-398 [5] of the International Atomic Energy Agency (IAEA) and the TG-51 [6] of the American Association of Physicists in Medicine (AAPM), the calibration of clinical dosimeters must be performed adopting water as the standard calibration medium and at the user energy spectrum in order to reduce uncertainties on dose determination [7, 8]. The reason for this is related to the fact that although the quantity of interest is absorbed dose to water, previous dosimetry protocols such as the TRS-277 [9] and TG-21 [10], were based on the use of exposure or air kerma calibration factors. Therefore, the conversion of quantities in air, determined at the

standardizing dosimetry laboratories, in quantities in water at hospitals, by means of a series of equations, makes it the use of dosimetry protocols a complex task. In addition, that procedure used to contribute for increasing uncertainties in the calculation of final quantities.

1.2 Reference dosimetry

Ionization chambers are usually calibrated in absorbed dose to water in ^{60}Co photon beams. This means that the calibration factor needs to be corrected when those dosimeters are used in an energy beam different from the calibration one. Except when using ionization chambers in ^{60}Co beam, the calibration beam quality Q_0 will always be different from the user's beam quality Q . This brings up the definition of the beam quality correction factor k_{Q,Q_0} as the ratio, at the qualities Q and Q_0 , of the calibration factors in terms of absorbed dose to water [5–8]. In this sense, k_{Q,Q_0} corrects for the effects of the difference between the reference beam quality Q_0 and the actual user quality Q . The corrections thus applied are related to the differences in response of clinical dosimeters at different radiation spectra. They also incorporate the restrictions for applying the theoretical background in the procedures for determining absorbed doses [11].

The background theory adopted in most dosimetry protocols is based on Spencer-Attix cavity theory [12]. Ionization chambers should meet the assumptions of the cavity theory adopted in order to provide the absorbed dose to the medium from its reading. Since most practical chambers will not perfectly meet those assumptions, one must know the corrections for departures of ionization chambers from theoretical

conditions. In this sense, the main corrections applied to ionization chamber readings are related to the perturbation that the cavity, the wall and the electrode cause to the fluence of photons and electrons [13, 14]. An effective point of measurement (EPOM) is usually defined within the chamber volume in order to reduce corrections due to the cavity. In addition, cutoff energy values (Δ) for the water-to-air restricted stopping power ratio are defined according to cavity features and radiation spectrum with the purpose to adapt the chamber to the demands of the theory.

Absorbed dose calibration factors are determined under reference conditions that are defined as a set of values of influence quantities for which the calibration factor is valid without further corrections [5]. It is important to point out that correction factors used in dosimetry of photon and electron beams can give rise uncertainties with the same degree of the required accuracy in reference dose determination. In this way, improvements of accuracy in dose determination in radiotherapy can be achieved by means of a detailed study of the correction factors applied to the response of dosimeters as well as an investigation of the methodology proposed in clinical protocols.

1.3 Surface dosimetry

The penetrating power of ionizing radiation increases with increasing the energy of radiotherapy beams and as consequence the maximum dose is deposited at larger depths in the medium. However, this does not imply that the dose deposited at the skin of the patient is negligible. Skin doses are usually a limiting factor in dose delivering even in treatments where tumors are deep-stated. For specific treatments where targets are very close to the surface, such as in treatment of skin, chest wall

irradiation for breast cancer and treatment of head-and-neck cancers, the evaluation of doses delivered at superficial depths is an important issue [15–19]. In stereotactic body radiotherapy (SBRT), the use of potentially overlapping multiple treatment fields combined with hypofractionated dose prescription scheme makes the skin one of the critical organs at risk (OAR) [20]. Several biological consequences such as increased erythema, fibrosis, necrosis and epilation are related to increase in surface dose as well as in the build-up region of radiation therapy beams. In this sense, surface dose distribution must also be accurately determined in order to avoid unnecessary skin reactions or under-dosage of near surface target volumes.

The tough nature of the skin makes its dosimetry a hard challenge. The different structures of the skin and its corresponding depths vary not only between patients but also between different parts of the human body (e.g., 0.02-0.06 mm for trunk and face and more than 0.16 mm for the finger tips) [21–23]. According to the International Commission on Radiological Protection (ICRP) and the International Commission on Radiation Units and Measurements (ICRU) [24] the basal and dermal layers are assessed for practical purposes at 0.07 mm and 1.0 mm respectively. Then skin dose is often considered as the dose in the basal layer or the dose to tissue at a depth of 0.07 mm (7 mg cm^{-2}) which is in turn the critical layer for carcinogenesis [25, 26]. On the other hand the knowledge of the dose distribution in and beyond the skin can be very important, such as in cases where the lymphatic system (at 0.5 mm depth) must be treated, in order to ensure that it will be adequately covered by the radiation.

Surface dose can be understood as the absorbed dose within an infinitesimally small mass of tissue at the surface of a phantom. However, there is no dosimeter with an infinitesimally small sensitive volume making the evaluation of surface doses inherently difficult [27]. In this sense it is important to point out that the term surface dose used by previous authors [1,2,28,29] does not correspond to the dose at $z = 0$ as some of them considered. When using a dosimeter the dose is assumed to correspond to the depth of its EPOM, which ranges from several micrometers (e.g., Capintec PS-033, Exradin A10, P11TW chambers and MD-810 GAFCHROMIC film) to a few millimeters (Roos and NACP chambers) [5]. For parallel plate chambers, the EPOM is considered to be the inside face of the entrance window. Therefore the dose at $z = 0$ can not be accessed by direct measurements or even calculated by computer simulations since in this last case one is always evaluating the dose in the middle of a voxel which has a finite size or thickness. In addition, there is a steep variation of the dose with depth near the surface which shows the importance of assigning the specification of the depth when using the term surface dose. This high gradient of dose with depth also makes the interpretation of the measurements in this region very difficult considering the spacial characteristics of ionization chambers.

Several dosimeters have been reported in the literature for evaluating surface doses such as fixed parallel plate chambers [2, 29–32], extrapolation chambers [1, 2, 29, 31, 32], TLDs [27, 33–35], diodes [36, 37], MOSFET [38] and radiochromic films [27, 39–41]. Parallel plate chambers are often the instrument of choice recommended by international dosimetry protocols [5, 6] for measuring doses at the

surface and in the build-up region of high energy photon beams. However, the general assumption that the measurement position is at the inside face of the chamber entrance window can not be applied for regions where electronic equilibrium does not exist such as in the build-up region and close to interface between two different media. For those places, electronic fluence perturbation mainly due to electrons emitted from the side wall will contribute to the ionization current and as a consequence the chamber will over-respond with the dose appearing to come from a depth greater than that of the front window [1, 30, 42]. As an approach to overcome that difficulty, some authors have used extrapolation chamber in order to assess corrected chamber measurements [1, 2, 29, 30, 43, 44]. Extrapolation chambers represent an alternative approach to the use of a standard calibrated ionization chamber. Its work principle is based on the fact that for sufficiently small cavity air masses m the ratio Q/m as a function of m is constant and can be replaced by the derivative dQ/dm in the cavity relationships. In contrast to Q/m , dQ/dm can be easier measured with good accuracy with extrapolation chambers which are parallel plate chambers especially designed for measuring variations of the air cavity mass through a controlled change in the electrode separation [43, 44]. Taking measurements at smaller and smaller distances between the electrodes one obtains the extrapolated zero volume reading, which is in turn proportional to the ionization very close to the surface of the detector, and thus eliminating the contribution of electrons from the side wall [1, 2, 29, 42, 45–47]. Although several authors [1, 2, 28, 29, 42, 46] have agreed with using extrapolation chambers as the most accurate method for measuring build-up region doses, none of them have used it in its proper sense as did Klevenhagen [43]

and Zankowski and Podgorsak [44]. Furthermore, extrapolation chambers are very time consuming, not widely available and impractical for clinical purposes

Monte Carlo (MC) simulation has been considered a "gold" standard for validating radiation dosimetry quantities as well as providing dosimetry data for the current clinical dosimetry protocols such as the AAPM TG-51 [6] or the IAEA TRS-398 [5], due to its great potential for accurately simulating the transport of radiation in the matter [48–51]. In this sense MC simulations is an useful tool for the study of correction factors used in dosimetry protocols as well as for the evaluation of the response of different ionization chambers at different radiation spectra without the costs of experimental procedures. Recent publications from the literature have shown that MC calculation have had an important role on the investigation of correction factors for ionization chambers in reference dosimetry [52–63]. However, performing simulations to obtain correction factors or comparing calculated and measured quantities requires very long computation time. In this sense, the use of methodologies to save CPU time can improve the efficiency of the simulation of ion chamber responses.

Some authors have also made use of MC techniques for investigating surface and build-up doses as well as correction factors for converting the dose to the air cavity of the chamber to dose to water for specific chambers in mega-voltage photon beams [30, 31, 39, 64]. However, there is still a lack of detailed information on the steep gradient of dose near the surface of water as well as a more complete set of correction factors for a variety of chamber and energy beams in order to determine accurately the dose at those non-reference conditions.

1.4 Purposes

Based on what has been exposed so far, the purpose of this study is to provide beam quality and perturbation correction factors for cylindrical chambers in reference conditions and for evaluating parallel plate chambers response at the surface of water phantom and in the build-up region of photon beams.

On a first step of this research, simulations with the code PENELOPE [65] was used to accomplish a detailed study of the components of the beam quality correction factor for the NE2571 ionization chamber widely used in radiotherapy with photon beams.

Subsequently, simulations with the EGSnrc [51] code system was used to do a detailed study of the response of plane parallel plate and extrapolated chambers at the surface and in the build-up region of high energies photon beams. Once calculated conversion factors are provided more accurate data can be used in treatment planning systems.

CHAPTER 2

Theory

2.1 Dosimetry quantities and equilibrium conditions

2.1.1 Absorbed dose vs KERMA

The concept of radiation equilibrium (RE) and charged particle equilibrium (CPE) have a crucial role for establishing relations between dosimetry quantities, such as absorbed dose (D) and kerma (K) [66]. Kerma stands for **K**inetic **E**nergy **R**elaxed per unit **M**Ass in the medium and is defined as the mean energy ($\bar{\epsilon}_{tr}$) transferred to charged particles by uncharged ionizing radiation (usually photons) per unit mass ($K = d\bar{\epsilon}_{tr}/dm$) [67,68]. Absorbed dose is defined as the mean energy ($\bar{\epsilon}$) imparted to the medium per unit mass within a specified volume of space ($D = d\bar{\epsilon}/dm$). Both quantities have unity of energy per mass (J/kg) in the SI which is also called gray (Gy). The transfer of energy from a photon ($h\nu$) to the medium can be understood as a two stage process. Figure 2–1 shows a schematic representation of this process [67].

In figure 2–1, the kerma can be identified as part of the photon kinetic energy ($h\nu - h\nu'$) that is transferred to an electron of the medium in (a). This electron in turn will give up its energy in two ways: by emitting bremsstrahlung photons ($h\nu''$) when interacting with a atomic nucleus (radiative kerma, K_r) and by collisions with other electrons (collision kerma, K_c). Relatively violent collisions electron-electron can also give rise another electron track called delta-ray. The Coulomb

force interactions with the electrons of the absorbing material will result in local dissipation of the energy as ionization and excitation in or near the electron track. On the other hand, x-ray photons produced due to interactions with the Coulomb force field of atomic nuclei, will carry the energy far away from the charged particle track since photons are relatively penetrating compared to electrons. Absorbed dose is identified in figure 2-1 as part of the kinetic energy (K.E.) lost by the electron in small collisions along its track in (b).

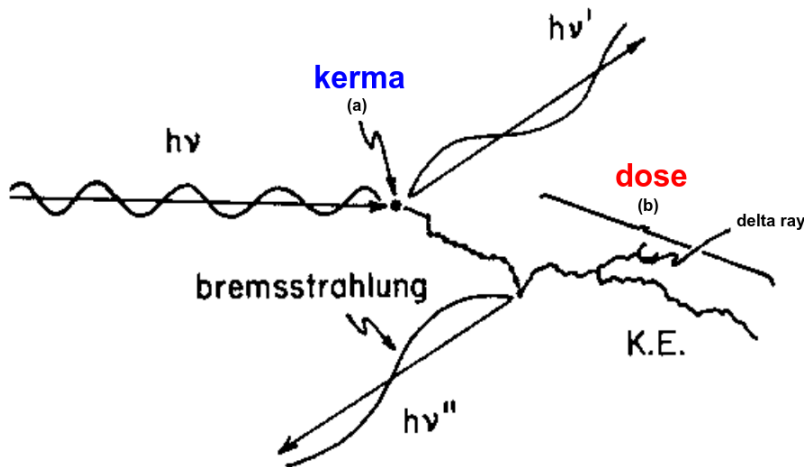


Figure 2-1: Schematic representation of the two stage process of transfer of energy to the medium by photons. In (a) a photon with energy $h\nu$ interacts with an electron of the medium and gives it a kinetic energy $h\nu - h\nu'$. This electron will then spend its kinetic energy by emitting bremsstrahlung photons ($h\nu''$) when interacting with atomic nucleus and by collision with other electrons. Relatively violent collisions electron-electron also gives rise delta-ray which is another electron track. Kerma correspond to the transfer of energy at (a) while absorbed dose corresponds to the imparted energy along (b). Adapted from *The physics of radiology*, Johns and Cunningham, 1983.

We can see from figure 2–1 that kerma and dose do not take place at the same location since electron tracks can have an appreciable length. Kerma takes place at a point (a) while absorbed dose occurs farther downstream within a range equals to the range of the electron (b). This has important consequences for calculating absorbed dose.

For a polyenergetic photon beam, the kerma is related to the energy fluence Ψ and the mass-energy transfer coefficient (μ_{tr}/ρ) by [66,67]

$$K = \frac{d\bar{\epsilon}_{tr}}{dm} = \int_{E=0}^{E_{max}} \Psi_E(E) \left(\frac{\mu_{tr}(E)}{\rho} \right) dE \quad (2.1)$$

where $\Psi_E(E) = d\Psi/dE$ is the differential energy fluence. Similarly, the collisional kerma, K_c can be given by:

$$K_c = \frac{d\bar{\epsilon}_{tr}^{net}}{dm} = \int_{E=0}^{E_{max}} \Psi_E(E) \left(\frac{\mu_{en}(E)}{\rho} \right) dE \quad (2.2)$$

where μ_{en}/ρ is the mass-energy absorption coefficient.

In this sense, the collision kerma (K_c), is related to the net energy transferred, ϵ_{tr}^{net} , defined for a volume V as the energy transferred to charged particles which is lost through collision interactions with other charged particles within the volume. Therefore, ϵ_{tr}^{net} excludes radiant energy emitted as radiative losses (R_u^r) by the charged particles which themselves originated in V , but regardless where the radiative loss events occur. Figure 2–2 [66] illustrates the differences between energy transferred, net energy transferred and energy imparted for a volume V with mass m , when a photon with energy $h\nu_1$ interacts within V via Compton effect followed by bremsstrahlung emissions ($h\nu_3$ and $h\nu_4$). Based on the definitions [66,68], the

energy transferred, net energy transferred and energy imparted will be respectively $\epsilon_{tr} = T = h\nu_1 - h\nu_2$, $\epsilon_{tr}^{net} = T - (h\nu_3 + h\nu_4)$ and $\epsilon = h\nu_1 - (h\nu_2 + h\nu_3 + T')$.

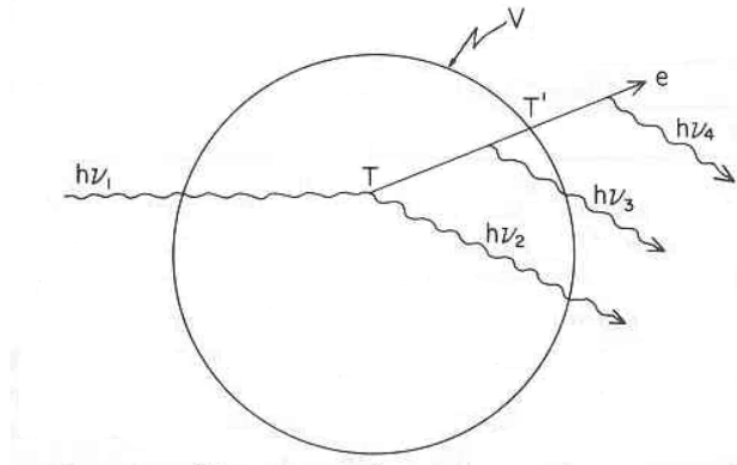


Figure 2-2: Illustration of the definitions of energy transferred, net energy transferred and energy imparted for the case of a photon with energy $h\nu_1$ interacting (via Compton) in a volume V with mass m . The energy transferred, net energy transferred and energy imparted are given respectively by $\epsilon_{tr} = T = h\nu_1 - h\nu_2$, $\epsilon_{tr}^{net} = T - (h\nu_3 + h\nu_4)$ and $\epsilon = h\nu_1 - (h\nu_2 + h\nu_3 + T')$. Reproduced from *Introduction to Radiological Physics and Radiation Dosimetry*, F. H. Attix, 1986.

In opposite to kerma which can be easily related to the fluence of primary particles, as shown in equations 2.1 and 2.2, absorbed dose cannot be calculated in this simple way unless there is a state of equilibrium between these two quantities.

2.1.2 Radiation and charged particle equilibrium

It is said that radiation equilibrium (RE) exists in a volume v if for each particle that leaves the volume v an identical particle enters the volume. The implications of

this can be expressed by the following equalities:

$$(R_{in})_u = (R_{out})_u \quad (2.3)$$

$$(R_{in})_c = (R_{out})_c \quad (2.4)$$

where $(R_{in})_u$ is the radiant energy from uncharged particles entering v , $(R_{out})_u$ is the radiant energy from uncharged particles leaving the volume, $(R_{in})_c$ is the radiant energy from charged particles entering the volume and $(R_{out})_c$ is the radiant energy from charged particles exiting the volume.

Considering a larger volume V where material and density are homogeneous, the radiation source is uniformly distributed in V and the charged particles paths are not perturbed by external electric or magnetic field, one can admit that RE exists in the sub-volume v , if the minimum distance between the surfaces of v and V is greater than the maximum depth of penetration of any ionizing radiation within V [66, 68]. For uncharged particles such as photons which have an undefined depth of penetration, RE is very difficult to be achieved since it is not possible to create a finite distance between the surfaces of v and V . However, it is possible to achieve RE to within some percentage in v by considering a fraction of photons penetrating to a certain distance [66, 68].

Charged particle equilibrium (CPE) in its turn, it is said to exist in a volume v if for each charged particle entering v there is an identical charged particle, i.e., same type and with the same kinetic energy, leaving the volume. Under this condition, it is valid the equality shown in equation 2.4. We can see from the definitions that RE is

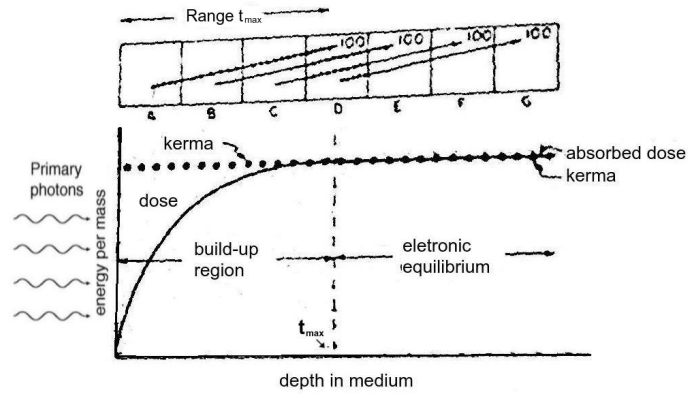
a sufficient condition for having CPE, although the opposite is not true. Therefore, CPE can exist even in the absence of RE, and this has a practical importance in situations where CPE conditions can be adequately approximated.

It is easy to show that under condition of CPE, i.e., $(R_{in})_c = (R_{out})_c$, the energy imparted to the medium ϵ is equal to the net energy transfer, ϵ_{tr}^{net} . Therefore the absorbed dose D equals the collision kerma K_c and is given by:

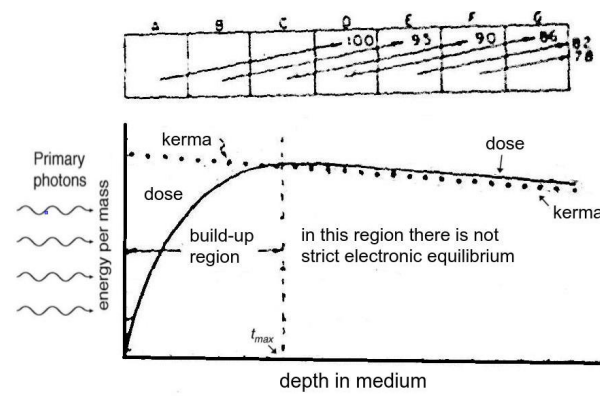
$$D = \frac{d\bar{\epsilon}}{dm} \stackrel{\text{CPE}}{=} \frac{d\bar{\epsilon}_{tr}^{net}}{dm} = K_c \quad (2.5)$$

Due to its importance for radiation dosimetry, the conditions for CPE will be analysed in two different situations where a pure (without contaminant electrons) photon beam reaches an absorbing medium as illustrated in figure 2–3 [67]. For simplicity, the electrons are set in motion at slight angles to the direction of the incident photon beam and all the electron tracks are considered to travel a distance equal to the range t_{max} (maximum range of secondary charged particles produced) in the same direction.

In figure 2–3(a) we consider a non-realistic situation where the photons are not attenuated in the medium and the same number of electron tracks (100) are set in motion in each square from A to G. In this sense we can see that the square D is traversed by 400 tracks, 100 of which started in each of the squares A, B, C and D. Therefore, the total ionization produced in the square D is equal the total ionization produced by the 100 tracks that traversed each of the 4 squares starting in A.



(a)



(b)

Figure 2-3: Schematic illustration of how kerma and absorbed dose vary with depth in charged particle equilibrium (CPE) in (a) and transient charged particle equilibrium (TCPE) in (b). In (a) a non-realistic situation is considered where the photon beam is not attenuated. In (b) a more realistic situation considers an attenuation of the primary particles of 5% at each depth corresponding to a distance between consecutive squares. Adapted from *The physics of radiology*, Johns and Cunningham, 1983.

Since the absorbed dose is proportional to the ionizations produced in each of the squares, its values will increase from zero until its maximum value at depth t_{max} . The kerma and dose in each square would be, in arbitrary units, $K_A = 100$ and $D_A = 25$ ($100/4$), $K_B = 100$ and $D_B = 50$, $K_C = 100$ and $D_C = 75$, $K_D = 100$ and $D_D = 100$ for the squares A, B, C and D respectively. As a result we can say that a CPE exists at any depth beyond t_{max} equals to the maximum range of secondary charged particles produced and where for each electron stopped in any volume, an identical one will be set in motion. The region between the surface and t_{max} is called build-up region, and beyond it is called region of electronic equilibrium. Nonetheless, the production of charged particles by photons is a result of photon interactions in the medium. In this sense, in a more realistic situation the photon beam will be attenuated and as a consequence will produce a non-uniform fluence of secondary particles which also decreases with the attenuation of the primary particles. Therefore CPE never exists within the medium for external sources, but can be approximately achieved in volumes where the attenuation can be negligible.

Figure 2-3(b) shows a more realistic situation where the photon beam is attenuated exponentially reducing of 5% the intensity of the beam in a distance equal to the distance between the squares. In this case the number of electrons set in motion in the successive squares A, B, C, D, E and F will be 100, 95, 90, 86, 82 and 78 respectively, and thus the kerma will also decrease continually. We can see now that the ionization in the square D will be composed by 100 tracks that originated in A, 95 from B, 90 from C and 86 from D. It is easy to verify that in this situation the number of ionizations in D will be less than the full ionization produced by the 100

tracks starting in A. CPE will then never be established, since at no place in the medium are as many electrons set in motion as are brought to rest in it. Absorbed dose (ionizations) will first increase and then decrease after its maximum value at depth t_{max} . Therefore, beyond t_{max} , kerma and dose will both decrease exponentially with absorbed dose curve being always above kerma curve if radiative losses are negligible. The reason for this is that absorbed dose at any point after t_{max} is due to the collision kerma further upstream. This can be expressed as [66,68]:

$$D(x) = K_c(x - \bar{x}) = K_c(x)\beta \quad (2.6)$$

where $\beta \geq 1$ and \bar{x} is the mean distance where secondary charged particles carry their kinetic energy while depositing it as dose. This is also illustrated in figure 2-4 [68] as the distance between the depths where absorbed dose has the same value of collision kerma [66,68].

In this region beyond t_{max} where dose is proportional to the collision kerma ($D = \beta K_c$), an equilibrium condition called transient charged particle equilibrium (TCPE) is said to approximately exist.

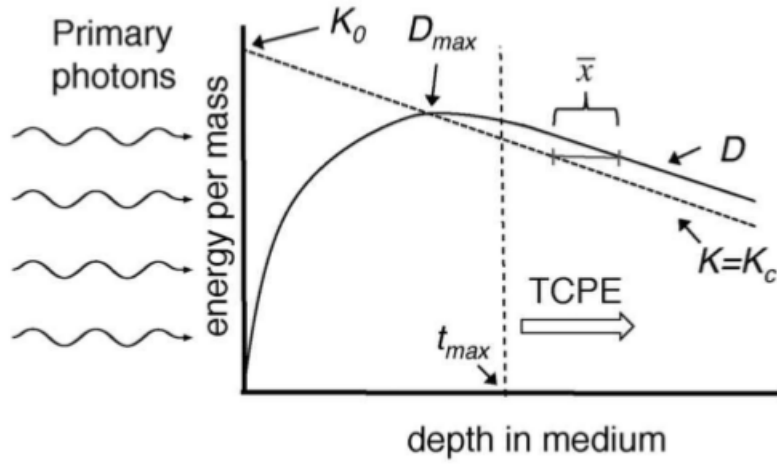


Figure 2-4: Illustration of transient charged particle equilibrium (TCPE) where absorbed dose (D) is proportional to collision kerma (K_c). TCPE occurs beyond the maximum depth of penetration (t_{max}) of secondary charged particles. Radiative losses are assumed to be absent ($K_r = 0$) and then $K = K_c$. Reproduced from Basic Radiation Interactions, Jeffrey V. et al in *Clinical Dosimetry Measurements in Radiotherapy*, Rogers and Cygler, 2009.

As we have seen from equation 2.2, kerma is proportional to the fluence of primary particles and then will also be attenuated according to:

$$K_c(x) = K_c(x - \bar{x})e^{-\mu\bar{x}} \quad (2.7)$$

Combining equations 2.6 and 2.7 we can find:

$$\beta = \frac{K_c(x - \bar{x})}{K_c(x)} = e^{\mu\bar{x}} \quad (2.8)$$

where β and \bar{x} depend upon the incident photon energy.

For photon beams with low energies (up to 3 MeV) and low-Z media such as carbon, water and air, radiative losses are negligible and as a result $K_r \approx 0$ and $\bar{x} \approx 0$, which leads to $\beta \approx 1$ and then $D(x) = K_c(x)$. A true TCPE is also never achieved due to the build-up of the scattered photons with depth which violates the assumptions that those photons do not interact within the distance \bar{x} and that the energy fluence includes a steady state of the scattered photons. This is only true after several mean free paths of the scattered photons and therefore TCPE is only an approximation for external photon beams.

2.2 Cavity Theory

Radiation dosimetry can be understood as the science related to the quantitative determination of the energy imparted to the matter by ionizing radiation [66]. Since only a calorimeter could directly provide an estimation of absorbed dose (energy per unit mass delivered by charged particles) by measuring the rise in temperature of an isolated mass of the medium, any other detector used for that purpose must have its reading corrected for providing the dose to the medium [67]. In this sense, the first challenge to be overcome is related to the fact that the absorbed dose in the sensitive material of the detector (D_{det}) will in general differ from the absorbed dose in the medium in the absence of the detector (D_{med}). On the other hand, for the detector to be considered as a dosimeter, the physical quantity provided M_{det} , which is in general expressed in electric charge or current, must be proportional to (D_{det}) [69]. The step from converting M_{det} in (D_{det}) at a specific radiation beam represents the calibration process and is accomplished by Primary Standard Dosimetry Laboratories (PSDLs).

Cavity theory is the name of the theoretical background which allows us to relate the absorbed dose in an arbitrary medium (D_{med}) for a radiation beam with quality Q (which can be photons or electrons), to the absorbed dose in a detector (D_{det}) placed in that medium. This name comes from the common use of gas-filled ionization chambers, which can be thought of as a cavity introduced in the uniform medium, in order to evaluate the absorbed dose [66, 67, 69]. Therefore, generally speaking, any cavity theory consists in determining a factor $f(Q)$ for converting D_{det} in D_{med} as it is showed schematically in figure 2-5 [69].

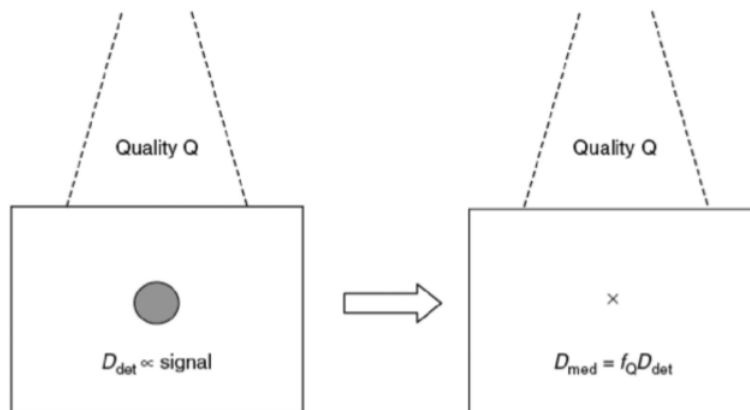


Figure 2-5: Determination of D_{med} from D_{det} . Reproduced from Cavity theory, stopping power ratios, correction factors, A. E. Nahum in *Clinical Dosimetry Measurements in Radiotherapy*, Rogers and Cygler, 2009.

2.2.1 Bragg-Gray cavity theory

W.H.Bragg [70] and L.H. Gray [71, 72] studied the problem of relating the absorbed dose in a gas cavity inserted in a medium to that in the medium itself and

established an important condition with respect the fluence of charged particle crossing the cavity [66]. According to the Bragg-Gray theory, if the cavity is small in comparison with the range of the charged particles striking it, the cavity will not perturb the charged-particle field. Then, for the case where the vast majority of charged particles are electrons, the electron fluence in the cavity $\Phi_{gas}^{e^-}$ at some depth z in the medium will be identical to that existing in the medium in the absence of the cavity $\Phi_{med,z}^{e^-}$. A direct consequence of this condition is that the absorbed dose in the cavity will be deposited entirely by the charged particles crossing it, which means that any contribution to the dose due to photon interactions in the cavity is negligible. Otherwise, if the build-up of dose due to interactions in the cavity is not negligible, then the charged particle fluence will not be the same as that in the undisturbed medium [66,69]. Practically speaking, for the case of photon beams only gas-filled detectors, i.e., ionization chambers will fulfil this condition, since those kind of detectors act as an "electron detector" [69].

If we consider that a mono-energetic photon beam is incident on a uniform medium, med , and gives rise secondary electrons of appreciable ranges, the ratio of dose in the medium at some depth z , $D_{med,z}$, to the dose in a gas cavity, \bar{D}_{gas} , placed at that same position where it is assumed to exist a δ -ray equilibrium, can be written in principle as:

$$\frac{D_{med,z}}{\bar{D}_{gas}} = \frac{\Phi_{med,z}^{e^-}(S_{col}/\rho)_{med,z}}{\Phi_{gas}^{e^-}(S_{col}/\rho)_{gas}} \quad (2.9)$$

where $(S_{col}/\rho)_{med}$ and $(S_{col}/\rho)_{gas}$ are the unrestricted electron mass collision stopping powers of the two media. If the detector can be considered as a *Bragg-Gray* cavity,

then $\Phi_{gas}^{e^-} = \Phi_{med,z}^{e^-}$ and the equation 2.9 can be reduced to:

$$\frac{D_{med,z}}{\overline{D}_{gas}} = \frac{(S_{col}/\rho)_{med,z}}{(S_{col}/\rho)_{gas}} \quad (2.10)$$

Actually the second electrons at depth generated by the photon beams in the medium will have a broad distribution of energies. Therefore a more accurate expression for evaluating the stopping-power ratio as an integral over the electron fluence spectrum should be written as:

$$\frac{D_{med,z}}{\overline{D}_{gas}} = \left(\frac{\overline{S}_{col}}{\rho} \right)_{gas}^{med} = \frac{\int_0^{E_{max}} (\Phi_E^{e^-})_{med,z} (S_{col}(E)/\rho)_{med} dE}{\int_0^{E_{max}} (\Phi_E^{e^-})_{med,z} (S_{col}(E)/\rho)_{gas} dE} \quad (2.11)$$

where $\Phi_E^{e^-}$ is the electron fluence differential in energy and accounts for the fluence of primary electrons only. It is important to point out that equation 2.11 is strictly valid only in the condition of the δ -ray equilibrium mentioned before. If there is charged particle equilibrium (CPE) at a point in the medium, there will also be δ -ray equilibrium at the same point, although this last one is a less demanding condition than the first one [69].

2.2.2 Spencer-Attix cavity theory

The δ -ray equilibrium requirement for the validity of equation 2.11 implies that if we have a small gas-filled cavity traversed by electrons tracks, as illustrated in figure 2-6 [68], the contribution for the dose in the gas cavity by incoming δ -rays generated in the medium must be exactly balanced by that ones generated in the gas

and that will escape from there. Therefore, this requirement will only be fulfilled if the medium and the gas are exactly equivalent or if all δ -ray ranges are negligible.

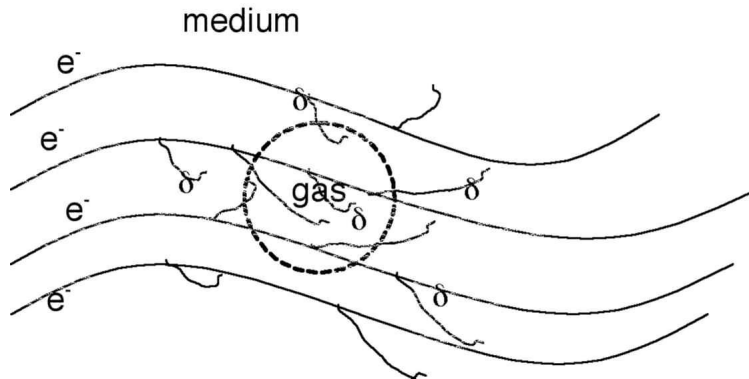


Figure 2-6: A gas filled cavity in a medium traversed by electron tracks. Reproduced from Cavity theory, stopping power ratios, correction factors, A. E. Nahum in *Clinical Dosimetry Measurements in Radiotherapy*, Rogers and Cygler, 2009.

Since in general the materials of the cavity and of the external medium will be different, the main expectation would be the δ -ray ranges being negligible in order to get the desired equilibrium. However this assumption can be hardly achievable since the cavity should also be small enough for not perturbing the electron fluence (Bragg-Gray cavity). A good evaluation of the δ -ray equilibrium condition can be achieved by looking into the fraction of the energy lost in collisions by primary electrons that is deposited within a small gas cavity inserted in a medium [69]. Considering that the vast majority of ion chambers used in radiotherapy has an air volume with diameters between 4 and 6 mm, an electron with continuous slowing down approximation (csda) should have energy of around 15 keV in order to cross a cavity of 5 mm diameter. In this sense, the part of the collision energy loss that is deposited locally (within the

cavity) can be determined by evaluating the collision energy losses below 15 keV for the mega voltage electrons, which can be provided by the ratio of the restricted to the unrestricted stopping-powers (L_{Δ}/S_{col}) with $\Delta = 15$ keV. Therefore, for cavities and energies of interest in radiotherapy (1 MeV to 10 MeV), approximately 80% of the energy lost in collision by primary electrons will remain in the cavity, which implies that the 20% will be carried out of the cavity by δ -rays generated in the cavity and this must be balanced by incoming δ -rays generated in the medium for having an "ideal" δ -ray equilibrium.

Deviations of Bragg-Gray cavity theory from experimental results were attributed to those long-range δ -rays by Attix and co-workers when irradiating parallel-plate air-filled ion chambers with different plate separations [69]. Based on this, Spencer and Attix [12] proposed a modification on Bragg-Gray's stopping-power ratio in order to account for energy deposition by δ -rays of appreciable ranges. For accounting only local energy depositions by all kind (primary or secondary) of electrons, they introduced a parameter Δ that represents a cutoff energy with which an electron can just cross the cavity. In this sense the local energy deposition can be determined evaluating the contribution of all incoming electrons with energies greater than Δ but with energy losses less than Δ as well as the electrons with energy dropping from Δ to zero . This is done through the use of the collision stopping power restricted to losses less than Δ , i.e., the restricted stopping-power (L_{Δ}/ρ) for the electrons with energy between Δ and E_{max} , and the unrestricted stopping-power (S_{col}/ρ) for the electrons with energy past Δ . Therefore, we can rewrite the dose to gas in equation

2.11 as:

$$D_{gas} = \int_{\Delta}^{E_{max}} (\Phi_E^{tot}(E))_{med} [L_{\Delta}(E)/\rho]_{gas} dE + \{\Phi_E^{tot}(\Delta)[S_{col}(\Delta)/\rho]_{gas}\Delta\} \quad (2.12)$$

where $(\Phi_E^{tot}(E))_{med}$ is the total (primary and secondary) electron fluence differential in energy E in the cavity which is assumed to be identical to that in undisturbed medium. The first term in equation 2.12 represents the dose deposited in the cavity due to electrons with energy down to Δ while the second one (also known as "track end" energy) represents the energy deposited by electrons with energy that drops from Δ to zero. By analogy, a similar expression can be written for the dose to the medium, D_{med} , and consequently the ratio between the dose in the undisturbed medium to that in the cavity gas D_{med}/D_{gas} which represents the factor $f(Q)$ will be expressed as:

$$f(Q) = \frac{D_{med}}{D_{gas}} = \left(\frac{\bar{L}_{\Delta}}{\rho} \right)_{gas}^{med} \quad (2.13)$$

where

$$\left(\frac{\bar{L}_{\Delta}}{\rho} \right)_{gas}^{med} = \frac{\int_{\Delta}^{E_{max}} (\Phi_E^{tot}(E))_{med} [L_{\Delta}(E)/\rho]_{med} dE + \{\Phi_E^{tot}(\Delta)[S_{col}(\Delta)/\rho]_{med}\Delta\}}{\int_{\Delta}^{E_{max}} (\Phi_E^{tot}(E))_{med} [L_{\Delta}(E)/\rho]_{gas} dE + \{\Phi_E^{tot}(\Delta)[S_{col}(\Delta)/\rho]_{gas}\Delta\}} \quad (2.14)$$

The restricted stopping power ratio defined by equation 2.14 is also known as the Spencer-Attix stopping-power ratio, and can also be written as $s_{med,gas}$ (IAEA's notation). It is important to point out that on defining Δ as the energy of electrons that have a range in the cavity gas just sufficient to cross the cavity, Spencer and

Attix bring up the size of the cavity into the computation of the stopping-power ratio. Therefore, estimating Δ is an important issue for designing practical ion chambers.

2.2.3 Cavity theory vs. ion chambers: Correction factors

The equation 2.13 allows one to know the dose to the medium at some depth z from the average dose in the gas cavity of the detector if this detector fulfils the conditions required from the Bragg-Gray theory. For an ionization chamber, for example, that behaves as a perfect Bragg-Gray cavity and once the restricted stopping power ratio of the two media is provided, $D_{med,z}$ could be given by [69,73,74]:

$$D_{med,z} = \bar{D}_{air} \left(\frac{\bar{L}_{\Delta}}{\rho} \right)_{gas}^{med} \quad (2.15)$$

However, practical ion chambers in mega-voltage photon and electron beams will in general present departures from perfect Bragg-Gray behaviour, which can be attributed for example to the several materials that compose the different parts of an ionization chamber as illustrated in figure 2-7 [69].

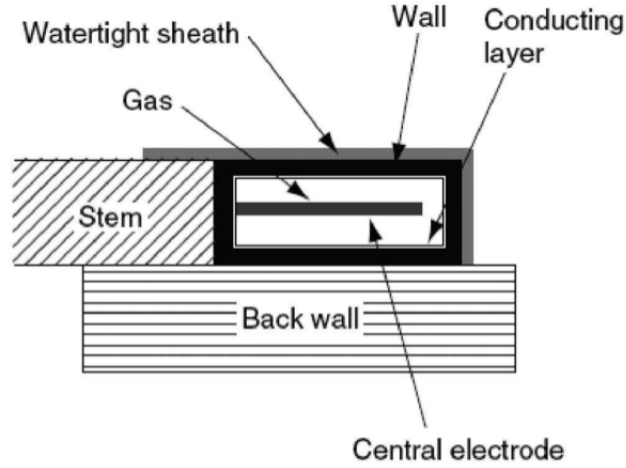


Figure 2–7: Illustration of practical ionization chamber showing its different components that can be a source for Bragg-Gray detector condition deviations. Reproduced from *Cavity theory, stopping power ratios, correction factors*, A. E. Nahum in *Clinical Dosimetry Measurements in Radiotherapy*, Rogers and Cygler, 2009.

In this sense many corrections must be made when using equation 2.15 in order to make it useful for real ionization chambers. Taking into account these corrections, the dose to medium at some depth z , $D_{med,z}$, can be related to the dose in the air cavity of the chamber, \bar{D}_{ch} , by [69, 73–77]:

$$D_{med,z} = \bar{D}_{ch} \left(\frac{\bar{L}_{\Delta}}{\rho} \right)_{gas}^{med} P_{wall} P_{cel} P_{repl} \quad (2.16)$$

where P_{wall} is the correction factor which accounts for non-medium equivalence of the chamber wall and any waterproofing material; P_{cel} is the factor that corrects the response of an ionization chamber for having a central electrode different from the cavity medium and P_{repl} accounts for the medium of interest (phantom) being replaced by the air cavity of the chamber. P_{repl} is usually considered as having two

components, which according to AAPM's TG-21 dosimetry protocol [10] are specified as the gradient correction P_{gr} , and the fluence correction P_{fl} . Its corresponding notation according to IAEA [5] are respectively p_{dis} , the displacement correction, and p_{cav} , the fluence correction. The importance of P_{gr} is related to the fact that in regions of the medium where there is a variation of the dose in a depth interval corresponding to the size of the chamber cavity, the electron fluence in the cavity corresponds to the fluence in the medium at some point above and closer to the surface. This happens because there is less attenuation in the air cavity than in the medium being replaced [69, 73]. This is particularly important for cylindrical chambers in high dose gradient regions, since for these kind of chambers, the dose referred to the position of its center is a weighted average of the doses at depths in the medium corresponding to predominantly the entrance points of its curved front face. An alternative approach from using a factor P_{gr} is to adopt an effective point of measurement (P_{eff}), which is a point shifted from the chamber center towards the source [5, 78], as illustrated in figure 2-8 [5]. In this case, if the reference depth z_{ref} where the dose is required, matches the P_{eff} of the chamber there is no more necessity for correcting the gradient effect and therefore P_{gr} is taken to be unity.

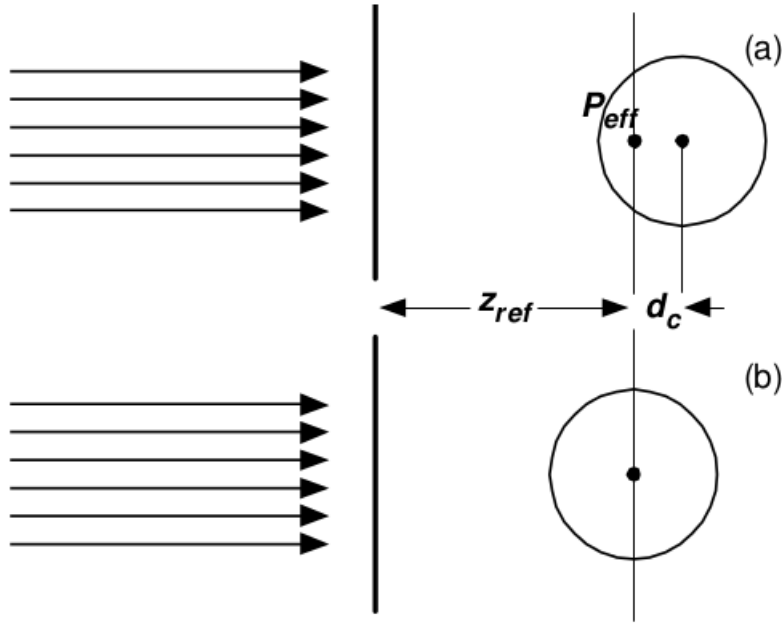


Figure 2-8: Illustration of the adoption of an effective point of measurement P_{eff} for cylindrical chambers. (a) The chamber is positioned with its P_{eff} at the reference depth, z_{ref} , and then $P_{gr} = 1.00$. d_c represents the shift for the P_{eff} related to the center of the chamber. If the chamber is positioned with its center in z_{ref} (b), then P_{gr} is not equal 1.00. Reproduced from TRS-398, IAEA, 2001.

Since the gradient effects is directly proportional to the size (radius) of the cylindrical chamber and to how steep is the gradient dose at the point of measurement, P_{gr} will also depend on those quantities. However, currently dosimeter protocols, such as the TG-51 [78] and TRS-398 [5], adopt a very poor assumption for calculating the shift d_c , which depends only on the radius of the cavity r_{cav} : $0.5r_{cav}$ for electron beams and $0.6r_{cav}$ for photon beams. Kawrakow [79] has shown by Monte Carlo study of the P_{eff} offset in photon beams that the general assumption of $0.6r_{cav}$ is too simplistic, mainly in high dose gradient regions such as in the build-up. For

parallel-plate chambers, where the center of the inside face of its front wall is appropriately chosen to be the point of measurement, there is no gradient effects and then $P_{gr} = 1.00$ for these kind of chambers in photon or electron beams. P_{gr} is also assumed to be unity for both cylindrical and parallel-plate chambers at the depths of maximum dose d_{max} since there is no gradient of dose at those points.

The fluence correction factor P_{fl} , in turn, accounts for other changes in the electron fluence spectrum due to the fact the cavity material is not the same as the medium where it is inserted. According to the Fano's theorem, if a medium is exposed to an uniform radiation field, the secondary particles generated field will also be uniform and will not depend on the density of the medium, as well as on density variations from point to point [66]. It follows from this theorem that if there is CPE at any point in the medium, the charged particle fluence will not depend on the density variations of the medium. In this sense, for measurements made in photon beams at depths $z \geq d_{max}$ where exist transient charged particle equilibrium, the different material of the cavity will not be expected to giving rise any distortion in the secondary electron fluence and then P_{fl} is considered to be unity. However this is not true for the build-up region where the secondary electron fluence has not achieved its equilibrium shape yet [73].

Similarly to build-up regions in photon beams, this will not be the case for measurements made in electron beams where CPE cannot exist at any depth. The non-negligible fluence perturbation in electron beams by a cavity with low-density material compared to the medium can be better understood by analysing the two competing effects which arise in this situation and illustrated in figure 2–9 [66].

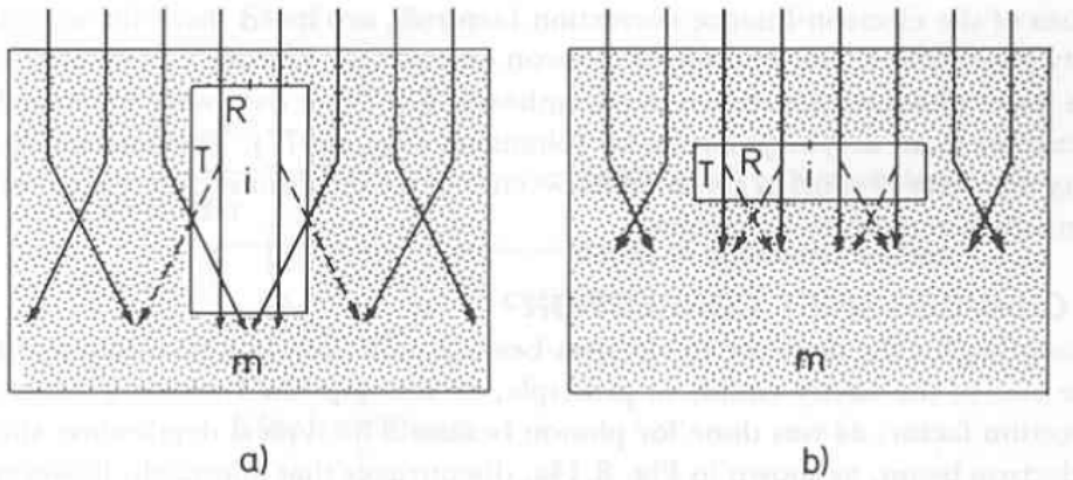


Figure 2-9: Illustration of the electron fluence perturbation effects caused by a low-density material cavity inserted in a phantom with higher density and irradiated by an electron beam. The paths of the electrons are idealized in order to emphasize the effects being shown. The electron tracks that would exist in the absence of the cavity are represented by the dashed lines. (a) The fluence in the cavity is increased compared to the situation without the cavity because the in-scatter effects are dominant over the out-scatter ones. (b) On the other hand, the obliquity effects decreases the fluence in the cavity because the electron paths are shorter (straighter) in a lower-density medium (gas). Reproduced from *Introduction to Radiological Physics and Radiation Dosimetry*, F. H. Attix, 1986.

The electrons are more scattered into the cavity by the surrounding higher-density medium than scattered out by the lower-density cavity gas and this contributes for increasing the fluence (in-scatter effect). This effect is especially predominant for chambers that are elongated in the beam direction. On the other hand, the obliquity or pathlength effect contributes for reducing the fluence since in this case the electrons go straighter in lower-density medium instead of being more scattered by a condensed medium. This effect tends to counter the side in-scattering

one as the cavity length is reduced. However more electrons are scattered in than are scattered out and therefore the presence of the cavity will in general increase the fluence and then we will have P_{fl} less than unity [66, 69, 73].

Despite the significant fluence corrections in electron beams, especially for cylindrical chambers, P_{fl} is usually considered unity for well-guarded parallel plate chambers because for those kind of detectors the dimensions of the guard ring can be large enough for excluding electrons scattered from the side walls and then making negligible its contribution to the dose in the active volume of the chamber. NACP, Attix and Roos are some of the chambers that can be included in this category [69, 73].

2.3 Ionization chambers

Ionization chambers are the most widely used dosimeter for radiotherapy and diagnostic radiology purposes [66]. Like any gas-filled detector it detects radiation by using the ionization produced within its gas cavity and are classified primarily by the voltage applied to the chamber. The voltage applied between the electrodes generates an electric field through the sensitive volume of the chamber in order to collect ionization and avoid recombination between the electrons and gas ions. However, in any practical case the charge Q' collected by the electrode and measured by the electrometer circuit will be less than the charge Q produced by the radiation, because of recombination of some positive and negative ions within the gas. Figure 2–10 shows the response of an ion chamber as a function of the voltage applied between its electrodes [80]. In figure 2–10 we can identify the ion chamber region (the plateau) where the chamber is said to be saturated to the degree that ion recombination is

absent. For voltages values within that region the initial charges released in the chamber are collected with near 100% efficiency ($Q'/Q \approx 1$).

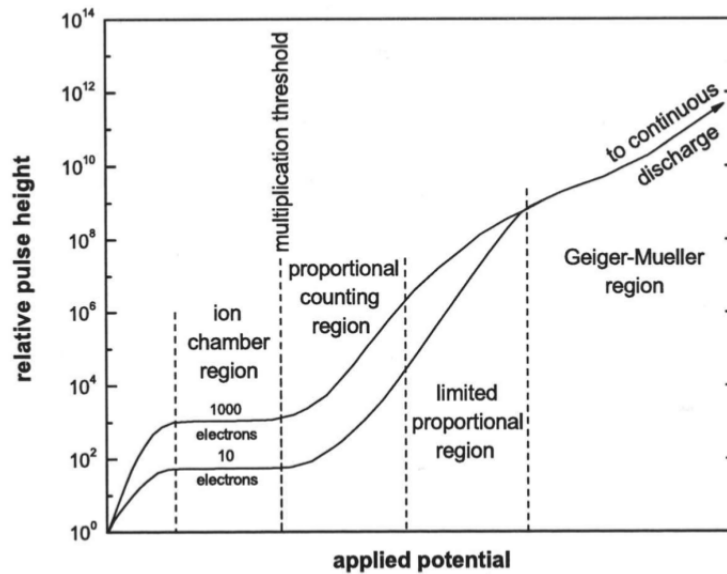


Figure 2-10: Response of an ion chamber as a function of the voltage applied between its electrodes. Reproduced from Ionization Chamber Instrumentation, Larry A. DeWerd et al in *Clinical Dosimetry Measurements in Radiotherapy*, Rogers and Cygler, 2009.

Before the chamber achieving saturation the recombination effect is large since the voltage applied is too low and then Q' is less than Q . Increasing the potential applied to the chamber recombination decreases and saturation is asymptotically approached. However, the voltage can not be increased indefinitely in order to eliminate recombination due to electrical breakdown of insulators or extra ionization produced by the accelerated initial charges (not due to the ionizing radiation field). This last situation where initial charge released has enough kinetic energy to create additional

ionization is desired in proportional and Geiger-Müller counter but not in ionization chambers.

Figure 2–11 shows the basic components of an ionization chamber which include the collecting electrode (collector), the guard and the shell which is also called, wall, thimble or window.

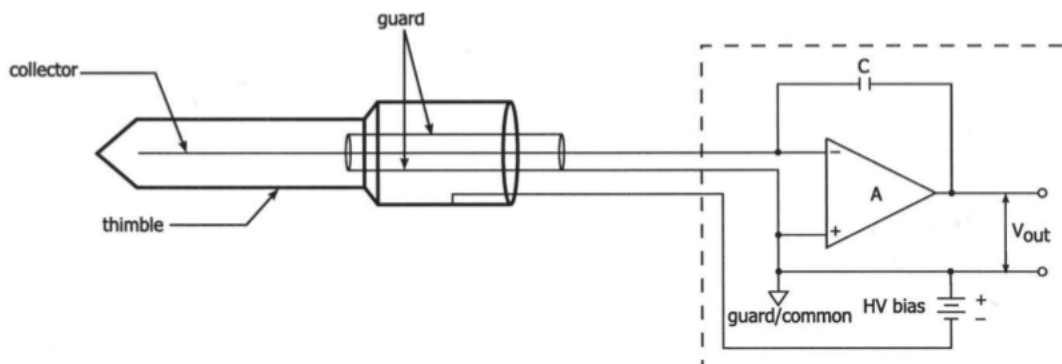


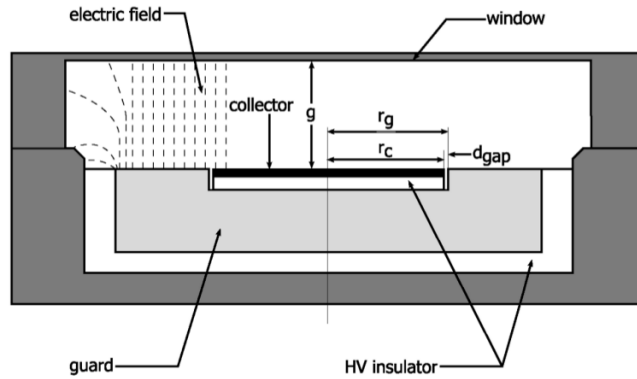
Figure 2–11: Simplified representation of an ionization chamber connected to a charge reading electrometer. Reproduced from Ionization Chamber Instrumentation, Larry A. DeWerd et al in *Clinical Dosimetry Measurements in Radiotherapy*, Rogers and Cygler, 2009

The electric field for collecting and stabilizing the ionization produced in the air of the cavity is generated between the ionization chamber components by a high-voltage power supply or battery within the electrometer (readout device). A triaxial cable transfers the chamber electric charge to the electrometer. Materials such as polyethylene or Teflon provide structural support and electrical insulation between each of the chamber components besides preventing leakage currents. The main purposes of the guard are to provide an electrical shield for the collector current

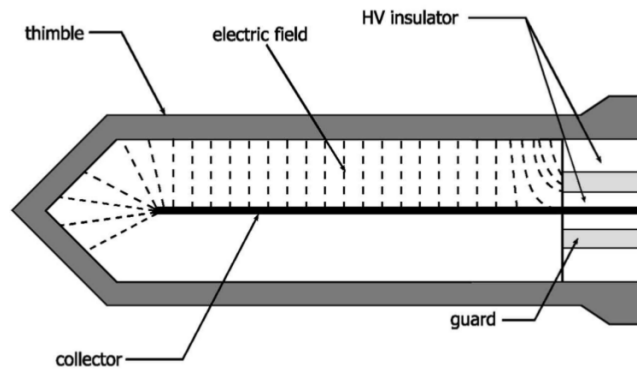
through the triaxial cable to the electrometer and to define the shape of the electric field in the ionization chamber collecting volume.

Despite having the same essential components ionization chambers are defined according to their geometric differences whose the most significant effect is related to differences in the chamber volumes. The volume of the cavity as well as the shape of the electric field are directly related to the size of the chamber signal. Figure 2–12 illustrates a plane parallel plate and a cylindrical (thimble) chambers which are types of chambers commonly used in radiotherapy [80]. The electric field between the collector and the window (or thimble) as well as between the guard and the window are shown in dashed lines. The nominal collecting volume of the parallel plate chamber is defined as the cylinder of air above the collector which also extends up to half width of the gap towards the guard.

Farmer type chambers are the reference dosimetry for measurements in high energy photon beams as well as in electron beam with energies above 10 MeV according to current dosimetry protocols. However the significant departure from unity of P_{fl} for this chamber make it unsuitable in low-energy electron beams [69]. Parallel plate chambers have usually small plate separation (between 1 and 2 mm) which gives better spatial and depth resolution than cylindrical chambers particularly in radiation beams with large gradients. In addition, the small separation between the electrodes results in a negligible change of the beam intensity across the sensitive volume.



(a)



(b)

Figure 2–12: Schematic illustration of a plane parallel plate chamber (a) and a Farmer type (thimble) chamber (b). The electric field is represented by the dashed lines between the electrodes of the chambers. In (a) the nominal volume of the chamber is defined by the separation between the electrode (g), the radius of the collector (r_c) and the radius of the inner edge of the guard (r_g). Reproduced from Ionization Chamber Instrumentation, Larry A. DeWerd et al in *Clinical Dosimetry Measurements in Radiotherapy*, Rogers and Cygler, 2009.

In order to convert their reading, M_{raw} , into absorbed dose to water, D_w , ionization chambers must be corrected for effects such as energy dependence, air pressure/temperature, ion recombination and polarity. Therefore, the fully corrected reading of an ionization chamber can be given by:

$$M = P_{ion}P_{TP}P_{elec}P_{pol}M_{raw} \quad (2.17)$$

where P_{ion} is the ion recombination correction factor, P_{TP} is the temperature and pressure correction factor, P_{elec} is the electrometer scale correction factor and P_{pol} is the polarity correction factor. Explanations on how to calculate each of these correction factors can be found in current dosimetry protocols.

2.4 Clinical dosimetry

The main modifications presented by current dosimeter protocols, such as AAPM TG-51 [78] and TRS-398 [5], when comparing to its previous versions (TG-21 and TRS-277 respectively) are the adoption of a formalism based on absorbed dose to water ($N_{D,w}$) instead of exposure (N_X) or air kerma (N_K) calibration factors, and the requirement for calibrating the detectors at the user energy beam. Due to the similar radiological properties of water to biological tissues, the main quantity of interest in radiation therapy is the absorbed dose to water [5]. In this sense, the determination of this quantity based on an air kerma (or exposure) formalism involves a complex chain of equations and chamber-dependent correction factors which do not account for differences between individual chambers of a particular type. This highlights the advantages of directly using an absorbed dose formalism as it has been pointed out for many authors [7, 8, 81]. Therefore, the expectation for reducing uncertainties in the

dose to water determination process as well as the use of a more simple formalism, opposed to converting from a free-air quantity to an in-phantom quantity, were the rationales for changing the basis of calibrations in modern dosimetry protocols.

Despite improvements obtained with the adoption of $(N_{D,w})$ formalism, the ideal requirement for calibrating ionizations chambers at the same quality as the user beam is not achievable because although most Secondary Standard Dosimetry Laboratories (SSDLs) provides calibration factors in ^{60}Co gamma-ray beams they cannot, in general, supply experimentally determined calibration factors for all high-energy photon and electron beams available [5]. This implies that calibration factors usually obtained in ^{60}Co beam must be corrected when using in the user beam with a different quality. According to the TRS-398 dosimetry protocol [5], the dose to the water in the absence of the chamber at reference depth d_{ref} and for a reference beam of quality Q_0 (usually ^{60}Co γ -rays) is given by:

$$D_{w,Q_0} = M_{Q_0} N_{D,w,Q_0} \quad (2.18)$$

where M_{Q_0} is the reading of the chamber fully corrected for influence quantities of different nature (quantities that are not the subject of the measurement) such as polarity effects, ion recombination, temperature and pressure, and relative humidity of the air cavity of the chamber. N_{D,w,Q_0} is the user ion chamber dose to water calibration coefficient for the quality Q_0 which converts the reading of the chamber in coulombs (C) or other detector unit to absorbed dose to water in gray (Gy). For using the detector in a beam quality Q different from the quality Q_0 in which it was calibrated, a correction factor should be applied to the calibration coefficient.

Therefore, the dose to the water under reference conditions for a beam of quality Q can be given by:

$$D_{w,Q} = M_Q N_{D,w,Q_0} k_{Q,Q_0} = M_Q N_{D,w,Q} \quad (2.19)$$

where k_{Q,Q_0} is the so called beam quality correction factor which account for effects due to differences between the quality Q of the user beam and the calibration quality Q_0 . From equation 2.19 we can see that k_{Q,Q_0} is thus defined as the ratio at the qualities Q and Q_0 of the absorbed dose to water calibration coefficients of the ionization chamber:

$$k_{Q,Q_0} = \frac{N_{D,w,Q}}{N_{D,w,Q_0}} = \frac{D_{w,Q}/M_Q}{D_{w,Q_0}/M_{Q_0}} \quad (2.20)$$

Since the reference quality Q_0 for calibration in standard laboratories is usually ^{60}Co gamma-ray beam, Q_0 is usually omitted and the quality correction factor is written just as k_Q . k_{Q,Q_0} should be ideally measured for each ion chamber and at the same user quality Q beam in clinical dosimetry, which is possible for only few PSDLs around the world that have appropriate beam qualities available [5]. However, k_{Q,Q_0} can also be calculated theoretically when there is no experimental data or its direct measurement is unfeasible. Under Bragg-Gray conditions and from equation 2.19 and the absorbed dose to air formalism ($N_{D,air}$) a theoretical expression for k_{Q,Q_0} can be obtained.

2.4.1 Theoretical determination of k_{Q,Q_0}

The mean absorbed dose to the air cavity of ionization chamber (\overline{D}_{ch}) having a kerma calibration factor N_K at a quality Q_0 can be related to the air kerma (K_{air})

(free in air) by [5, 8]:

$$\overline{D}_{ch,Q_0} = K_{air,Q_0}(1 - g)k_{att}k_mk_{cel} = N_{K,Q_0}M_{Q_0}(1 - g)k_{att}k_mk_{cel} \quad (2.21)$$

where M_{Q_0} is the reading of the chamber in the calibration beam corrected for influence quantities; g is the fraction of energy expended in radiative process (*bremsstrahlung*) by the photon-produced charged particles; and the other factors accounts for: attenuation effects due to absorption and scattering of ^{60}Co γ -rays (Q_0 quality calibration) in the chamber material (k_{att}); lack of equivalence between air and chamber wall and build-up cap material (k_m); and deviations from air equivalence of the central electrode material (k_{cel}). The absorbed dose to air in the cavity can also be written in terms of an absorbed dose to air chamber factor $N_{D,air}$ as:

$$\overline{D}_{ch,Q_0} = N_{D,air,Q_0}M_{Q_0} \quad (2.22)$$

The terminology "chamber factor" is used by Andreo [8] instead of "calibration coefficient" because $N_{D,air}$ is only a user-derived factor and then for distinguishing from a calibration coefficient determined experimentally by SSDLs. Comparison between equations 2.21 and 2.22 allows us to write the absorbed dose to air chamber factor $N_{D,air}$ as a function of the kerma calibration coefficient N_K as:

$$N_{D,air,Q_0} = N_{K,Q_0}(1 - g)k_{att}k_mk_{cel} \quad (2.23)$$

On the other hand, the absorbed dose to the air cavity of an ionization chamber can be given as [5, 8, 10]:

$$\bar{D}_{ch,Q_0} = J_{air,Q_0} \left(\frac{W_{air}}{e} \right) \quad (2.24)$$

where J_{air,Q_0} is the electric charge per unit mass of the air in the cavity (C/kg) and (W_{air}/e) is the mean energy deposited in air per ion pair released (J/C). (W_{air}/e) is usually assumed to be constant (33.97 ± 0.06 J/C) [73, 82] independent of the electron energy for photon and electron beams used in radiotherapy. From equations 2.22 and 2.24 the absorbed dose to air chamber factor $N_{D,air}$ can be written as:

$$N_{D,air,Q_0} = \frac{D_{ch,Q_0}}{M_{Q_0}} = \frac{J_{air,Q_0} \left(\frac{W_{air}}{e} \right)}{M_{Q_0}} \quad (2.25)$$

Since J_{air,Q_0} is proportional to the chamber response M_{Q_0} the ratio in equation 2.25 is a constant which depends only on the type of ionization chamber being used (dimensions and compositions) [10]. Therefore, under the assumption that $(W_{air}/e)_{Q_0} = (W_{air}/e)_Q$ the evaluation of $N_{D,air}$ at two qualities according to equation 2.25 provides:

$$\frac{N_{D,air,Q}}{N_{D,air,Q_0}} = \frac{J_{air,Q}(W_{air}/e)_Q}{M_Q} \frac{M_{Q_0}}{J_{air,Q_0}(W_{air}/e)_{Q_0}} = \frac{(W_{air}/e)_Q}{(W_{air}/e)_{Q_0}} = 1 \quad (2.26)$$

which shows that the absorbed dose to air chamber factor in the calibration quality Q_0 will also be valid at the user's beam quality Q ($N_{D,air,Q_0} = N_{D,air,Q}$).

From the Spencer-Attix cavity theory, the dose to the water at a reference depth z where the effective point of measurement of the chamber is positioned can be related to the dose in the air cavity according to equation 2.16, which in IAEA's [5] notation

and for a quality beam Q_0 is given by:

$$D_{w,Q_0}(z) = \overline{D}_{ch,Q_0}(s_{w,air})_{Q_0} [p_{wall} p_{cel} p_{cav} p_{dis}]_{Q_0} \quad (2.27)$$

Combining equation 2.27 with the formalism based on absorbed dose to air (equation 2.22) and absorbed dose to water (equation 2.18) we can finally write a relationship between both calibration coefficients as:

$$N_{D,w,Q_0} = N_{D,air,Q_0}(s_{w,air})_{Q_0} [p_{wall} p_{cel} p_{cav} p_{dis}]_{Q_0} \quad (2.28)$$

Since the beam quality correction factor k_{Q,Q_0} is defined as the ratio at the qualities Q and Q_0 of the absorbed dose to water calibration coefficients of the ionization chamber, it follows from equations 2.28, 2.26 and 2.20 that:

$$k_{Q,Q_0} = \frac{N_{D,w,Q}}{N_{D,w,Q_0}} = \frac{(s_{w,air})_Q [p_{wall} p_{cel} p_{cav} p_{dis}]_Q}{(s_{w,air})_{Q_0} [p_{wall} p_{cel} p_{cav} p_{dis}]_{Q_0}} = \frac{(s_{w,air})_Q p_Q}{(s_{w,air})_{Q_0} p_{Q_0}} \quad (2.29)$$

and its equivalent in the AAPM's notation [78] is given by:

$$k_{Q,Q_0} = \frac{\left[\left(\frac{\overline{L}_\Delta}{\rho} \right)_{air}^w P_{wall} P_{cel} P_{fl} P_{gr} \right]_Q}{\left[\left(\frac{\overline{L}_\Delta}{\rho} \right)_{air}^w P_{wall} P_{cel} P_{fl} P_{gr} \right]_{Q_0}} \quad (2.30)$$

which provides a theoretical expression for calculating k_{Q,Q_0} depending only on quotients of the water to air Spence-Attix stopping-power ratios and chamber perturbation factors evaluated at the energies Q and Q_0 . In equation 2.29, p_Q can be understood as an overall perturbation factor which gives rise to deviation in the Bragg-Gray assumption that the electron fluence (down to energy Δ) in the gas

cavity of the detector is identical to that in undisturbed medium at the point of interest [69, 83]. In this sense p_Q can be written as the product of the various perturbation factors, each one accounting for different effects related to the constructive details of the chamber and assumed to be independent of the others.

2.5 Absorbed dose determination with extrapolation chambers

As we have already discussed previously, Spencer-Attix cavity theory provides simple linear relationships between the dose to a point in the medium, D_{med} , and the dose to air, \bar{D}_{air} , inside a cavity positioned in that point. For a perfect Bragg-Gray cavity, this relationship is given by equation 2.15 which express D_{med} as the product of \bar{D}_{air} and $(\bar{L}_\Delta/\rho)_{air}^{water}$. On the other hand the dose to the air cavity can be given by equation 2.24, as a function of the charge per unit mass, J_{air} and the mean energy to produce an ion pair in air, \bar{W}_{air}/e . Combining those equations and writing J_{air} as the ratio Q/m , where Q is the charge collected in the sensitive air mass, m of the cavity, the dose to medium for a perfect Bragg-Gray cavity can be given by:

$$D_{med} = \frac{Q}{m} \left(\frac{W_{air}}{e} \right) \left(\frac{\bar{L}_\Delta}{\rho} \right)_{air}^{med} \quad (2.31)$$

However, although the charge Q can be measured to a high degree of accuracy with a calibrated electrometer, the effective mass m of the cavity is usually very difficult to measure. The standard method used to solve this problem is to calibrate the cavity chamber at, or trace its calibration to, a national standards laboratory. Therefore, absorbed doses to water are usually determined in radiotherapy clinics by making use of a calibrated cylindrical or plane parallel plate ionization chamber

and following the procedures of national or international dosimetry protocols, e.g., TRS-398 [5] and TG-51 [6]. The calibration coefficients allow the conversion of the ionization in the sensitive air volume of the chamber in dose to water and also incorporates various correction factors which accounts for chamber dimensions, wall composition, ion collection efficiency and perturbation in the fluence of photons and electrons due to the presence of the cavity.

An alternative for the use of calibrated ion chambers is to use uncalibrated variable air volume extrapolation chambers [43, 44] which has the advantage of not requiring the evaluation of chamber perturbation factors. These chambers are specially designed parallel plate ionization chambers which allows the variation of the cavity air mass through a controlled change in electrode (or plate) separation. Its work principle is based on the idea that for sufficiently small cavities with masses m , the ratio Q/m is constant as a function of m , and can be replaced by the derivative dQ/dm in cavity relationships. The derivative dQ/dm is then much easier-to-measure with extrapolation chambers than the ratio Q/m . Replacing this derivative in equation 2.31, the modified Spencer-Attix relationship can be written as [43, 44]

$$D_{med} = \frac{dQ}{dm} \left(\frac{W_{air}}{e} \right) \left(\frac{\bar{L}_{\Delta}}{\rho} \right)_{air}^{med} \quad (2.32)$$

or for parallel plate ionization chambers one can finally write:

$$D_{med} = \left(\frac{1}{\rho A} \right) \frac{dQ}{ds} \left(\frac{W_{air}}{e} \right) \left(\frac{\bar{L}_{\Delta}}{\rho} \right)_{air}^{med} = K \frac{dQ}{ds} \quad (2.33)$$

where ρ is the air density inside the chamber, A is the effective area of the measuring electrode and s is the separation between the polarizing and measuring electrodes.

The proportionality constant $K = (1/\rho A)(\overline{W}_{air}/e)\overline{L}_{air}^{med}$ is given for a specific chamber at a specific photon or electron beam. The effective area, A , of the chamber collecting electrode can be determined by measuring the capacitance C of the extrapolation chamber as a function of the electrode separation s . The derivative dQ/ds corresponds to the slope of the curve Q vs s and can be determined through a measurement of $\Delta Q/\Delta s$ which in turn can also be measured with a high degree of accuracy (within $\pm 0.2\%$) [44]. Since the air density, ρ , the mean energy \overline{W}_{air}/e and the medium to air restricted stopping-power ratio can also be known accurately, properly designed extrapolation chambers can be used for radiation dosimetry with similar accuracy to that obtained with calibrated ionization chambers.

2.6 Monte Carlo simulations

Generally speaking, a Monte Carlo (MC) method could be defined as one that deliberately makes use of random numbers for numerically solving problems. The method is particularly interesting when it is applied for making calculations in processes whose evolution is determined by random events (stochastic), e.g., the emission of radiation from atoms and its interaction with matter, since in these cases the events are to some degree unpredictable [84]. However the method is not restricted for applying in stochastic processes and indeed some definitions describe MC as the technique for solving non-probabilistic problems, e.g., for calculating an area under a curve, by using probabilistic methods [84]. The name was first used in the 1940s to designate a class of numerical methods based on the use of random numbers by scientists working on the nuclear-weapon project in Los Alamos [65, 84].

The simulation of random events can be done in a computer by means of a deterministic algorithm which generates a sequence of pseudo-random numbers that mimics the properties of what would be a truly random number. Although the use of MC method is not necessarily restricted to computers, the availability of modern digital computers can enormously enhance its effectiveness [84].

In the field of radiation transport, Monte Carlo technique can be understood as the simulation of random trajectories of individual particles by making use of knowledge of the probability distributions controlling the individual interactions of electrons and photons with matter [85]. In this sense, a given experimental arrangement, such as an electron beam coming out of an accelerator and impinging a water slab, is virtually simulated by considering the tracks (histories) of the particles as a random sequence of free flights which end with an interaction event and then the particle can change its direction, lose energy and produce secondary particles [65]. The process is repeated until the particle is absorbed or leaves the geometry of interest [65,86]. For simulating these histories is essentially to know the differential cross sections (DCS) for the relevant mechanisms of interaction, which will in turn determine the probability distribution functions (PDFs) that govern the physical processes involved [85]. The DCS will then provide the PDFs of the random variables that characterize a track, such as the free path between successive interaction events, the type of interaction taking place and the energy loss and angular distribution in a particular event [65]. Therefore both trajectories and interactions, are "determined" by using machine-generated (pseudo-) random numbers to sample from the PDFs.

In this way, quantitative informations on the transport process can be obtained by averaging over the simulated histories since its number is sufficiently large.

The random nature of Monte Carlo method implies that all results are strongly affected by statistical uncertainties which usually decrease as $N^{-1/2}$, where N is the number of histories simulated. The attempt to reduce uncertainty by only increasing N will also increase the computation time and then reducing simulation efficiency (ϵ), usually defined as [54, 87]:

$$\epsilon = \frac{1}{T \cdot \sigma^2} \quad (2.34)$$

where T is the CPU time needed for calculating a quantity of interest and σ is the corresponding estimated statistic uncertainty. However it is also possible to reduce uncertainty in Monte Carlo algorithms without increasing the computer simulation time and without introducing a systematic error in the calculation by using variance reduction techniques (VRTs) [54, 65, 87–90]. Some of these VRTs which are commonly used in many Monte Carlo codes are the *Splitting* technique, *Range Rejection* and the *Russian Roulette* game.

The ***Splitting*** technique [65, 89, 91–95] consists of favouring the flux of radiation towards the region of interest. This is accomplished by splitting particles with an initial weight w_0 and in a certain state into a number $N_s > 1$ of identical particles with weights w_0/N_s in the same state. In order to leave the simulation unbiased the weight of the splitted particles are taken into account when calculating mean and standard deviations of the quantities of interest [65]. The choice of an ideal number N_s strongly depends on the user experience and it is advisable running short simulations for obtaining significant efficiency gains.

The *Splitting* technique usually works better when combined with ***Russian Roulette*** game, which in turn is the reverse process, in the sense that it "kills" the particle when it tends to move away from the region of interest [65]. In the *Russian Roulette* technique a survival probability threshold equal to $1/N_r$ for the particles is defined and compared with a random number. If the random number is higher than the threshold then the particle is discarded, otherwise, if the random number is less than or equal the survival probability then the particle is kept and has its weight increased by N_r . The choice of N_r is likewise N_s a task that depends on the user ability.

Several MC codes are also provided with ***Range Rejection*** variance reduction technique, which can save significant quantities of computing time for electron transport calculations and it is very useful when calculating total energy deposition of charged particles in a given spatial region [65, 96]. The basic idea of this VRT is to absorb a charged particle if its residual energy is such that the particle cannot reach (or leave) regions of interest (e.g., cavity of an ion chamber). However *Range Rejection* is not considered a true variance reduction technique since it ignores the possibility of bremsstrahlung photons produced by the slowing down electron that might contribute to the dose in the region of interest or escape the local region [65, 96–98]. In this sense, a more accurate use of this technique is made by defining an energy threshold (called ESAVE in BEAMnrc) below which events such radiative photon emissions can be ignored and the technique is then applied [96–98]. It is important to point out that the choice of an appropriate threshold is situation

dependent and therefore one must use a sufficiently low value in order to guarantee the accuracy of the simulation [96,97]. Another approach that can make *Range Rejection* a true VRT, consists of using a *Russian Roulette* game with survival probability $1/n_r$, where $n_r > 1$ is a user-defined integer, for the electrons whose residual range is shorter than the distance to the region of interest [98].

2.6.1 Condensed vs Detailed simulations

Simulating the transport of electrons through the matter is a very time-consuming task due to the huge number of elastic scatterings undergone by an electron when interacting with nuclei during its history . In addition an electron also sets in motion a large number of low-energy "knock-on" electrons besides leaving many atoms in excited states. To overcome these problems, MC algorithms usually make use of a condensed-history technique [99] where the electrons path is broken into a series of steps for which the effects of the huge number of individual interactions that occur in the step are grouped together [85,100]. Since this step is much larger than the mean free path between real collisions, there is a large number of collisions that takes place along each step, whose length is chosen by the user or internally determined by the code. Based on this, the earliest simulation algorithms used to be classified into two different kinds [100]: "detailed" simulations, where all the collisions undergone by an electron are simulated in chronological succession, and "condensed" simulations where the simulation of the global effect of the collisions that occur in a track segment of a given length are accounted for by using approximate multiple scattering theories. The approximations used in those theories are the main limitations for the accuracy of condensed simulation methods. Although detailed simulation is exact

(apart from the inherent statistical uncertainties), in the sense that it provides the same results as those obtained by solving transport equation, it is only feasible when the average number of collisions per track is not too large. Examples of these situations are those involving either electrons with low initial kinetic energies (up to about 100 keV) or special geometries such as an electron beam impinging on thin foils [100].

A third class of simulation algorithms are called "mixed" [48,100] which combine detailed simulations for "hard" events, i.e., those with polar scattering angle or energy loss larger than previously selected threshold, with condensed simulations for "soft" interactions which in turn present scattering angle and energy loss smaller than the cutoff values. It is important to note, as Rogers and Bielajew [85] has pointed out, that the choice of these thresholds for considering the creation of secondary electrons or photons as discrete events is arbitrary and as so it is a component of the algorithm rather than a component of the physical processes involved. These threshold values can be properly selected in order to make the mean number of hard events per track sufficiently small for allowing their detailed simulation . This is the case for example, for high-energy electrons whose DCS for the various interaction processes decrease rapidly when scattering angles and energy losses increase. Hard events can only be well reproduced in a detailed way due to the large angular deflections and energy losses. On the other hand, since soft events has only a mild effect on the evolution of the track, they can be accurately reproduced by making use of multiple scattering approach [48]. In this sense, mixed simulation is usually preferable than condensed simulations due to its advantages such as: a more correctly simulation of

the spatial distributions; more appropriate handling of tracks in the vicinities of interfaces; and large reduction of possible dependencies of the results on user defined parameters [48].

2.6.2 Class-I and class-II algorithms

Currently MC codes are usually divided into two broad categories according to the energy of the primary electron is related to the energy lost in individual interactions [85]: the class-I models which groups together the effects on the primary electron of *all* interactions of a certain type for each step of the condensed history; and the class-II or mixed algorithms, where the effects of only a *subset* of the interactions of each type are grouped together, whereas the effects of the remaining interactions are treated on an individual basis. Therefore in a class-II algorithm, all interactions that produce "knock-on" electrons (or bremsstrahlung photons) with energy below some arbitrary threshold energy will be handled with a continuous energy-loss model (condensed-simulation) for grouping together all those kind of interactions. In contrast, all those relatively rare hard ("catastrophic") interactions that create secondary particles (knock-on electrons or bremsstrahlung photons) above the same arbitrary energy will be treated individually (detailed simulation).

Since class-II algorithms, where correlations between primary and secondary particles are included, are in principle more accurate than class-I, most currently available MC codes, such as PENELOPE [65] and EGSnrc [51] are based on this mixed kind of algorithm.

2.6.3 Monte Carlo codes

It is a consolidated idea that MC simulations is an accurate method for simulating the transport of ionizing radiation (especially photons and electrons) through the matter as well as the complex source configurations and geometries involved in radiotherapy [101]. The massive increases in computing power per unit cost in the last decades and the increasing availability of many powerful software tools are the main reason for the increased use of Monte Carlo techniques in the broad range of applications in Medical Physics [50]. Therefore, MC techniques represent an essential tool for radiation dosimetry and radiotherapy where accurate information on high energy problems involving coupled electron-photon transport is needed.

PENELOPE

The MC code PENELOPE whose name stands for *PEN*etration and *E*nergy *LO*ss of *P*ositrons and *E*lectrons is a mixed (class-II) simulation algorithm for simulating coupled transport of electrons, positrons and photons in the energy range from 50 eV to 1 GeV in arbitrary material systems consisting of a number of homogeneous regions (bodies) limited by interfaces [48, 49, 65, 100, 102]. The package was initially devised to simulate the penetration and energy loss of only positrons and electrons, but later it was modified to incorporate photons transport [102], combining mixed positron and electron simulation method with detailed simulations of photons.

PENELOPE is composed by a set of subroutine packages written in FORTRAN besides applications and a database for several materials of interest in radiological physics. The basic subroutine packages are distributed in 4 FORTRAN source files: PENELOPE.f which contains the subroutines for simulating the transport of the

particles; PENGINEOM.f which has the subroutines for controlling the geometry of the simulation by tracking particles through modular quadric geometries (systems with up to 10,000 surfaces and 5,000 bodies); PENVARED.f which are the variance-reduction subroutines; TIMER.f which contains the timing subroutines for managing the time of the simulation; and MATERIAL.f which is the program to generate material data files [65]. For being a subroutine package, PENELOPE cannot operate by itself and then it needs a steering main program for controlling the geometry and the evolution of tracks, as well as, for keeping score of the relevant quantities and performing the required averages at the end of the simulation [65]. This main program must be provided by the user and can be edited for his particular problem from the PENMAIN.f file which is also provided by the code, and contains the call for the four subroutine packages mentioned above. In this way, for developing a simulation the user should compile and link the files PENMAIN.f, PENELOPE.f, PENGINEOM.f, PENVARED.f and TIMER.f in order to create the executable file of PENMAIN.f (*penmain.exe*) as illustrated in figure 2–13. The input file *user.in* has the main informations related to the user’s simulation (number of histories, source definition, field size, simulation parameters, etc) and can be edited from the example *penmain.in*. This input file will also point to the files *user.geo* and *user.mat* which contain the informations about the geometry and materials of the simulation respectively.

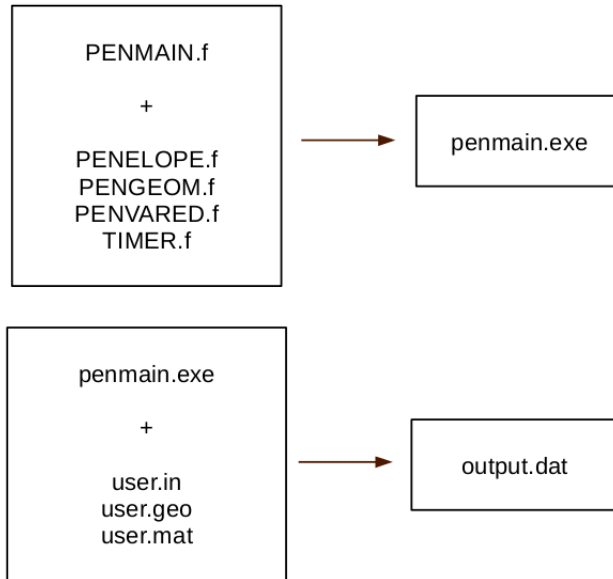


Figure 2–13: Compiling and running PENELOPE code.

The file *user.geo* can also be edited from the example *sample.geo*, where one can define the regions of interest by using quadric surfaces [65]. The material data files *user.mat* (e.g., *water.mat*, *air.mat*, etc.) are generated by the user from the executable binary file *material.exe*, which in turn is created by compiling and linking the source files *MATERIAL.f* and *PENELOPE.f*. The output file (*output.dat*) generated by the execution of the program *penmain* contains in its default mode general information about the simulation such as average deposited energies, average number of generated secondary particles, doses distributions, simulation speed, etc., which are given with its respective statistical uncertainty (3σ). The user should modify the source file *PENMAIN.f* in order to get his specific results in the *output.dat* files.

Important simulation parameters that account for the speed and accuracy of photons, positrons and electrons transport in PENELOPE must be set in the input-file *penmain.in* for each material in the simulated structure. Some of these parameters are the absorption energies E_{abs} at which the transport of the particles are terminated and the remaining kinetic energy assumed to be deposited locally; the cutoff energies (thresholds) for the production of delta rays, W_{CC} , and bremsstrahlung radiation, W_{CR} ; and the elastic scattering parameters, $C_1 \simeq 1 - \langle \cos \theta \rangle$, related to the average angular deflection produced along a step length and which determines the mean free path between hard elastic events, and C_2 which is the maximum average fractional energy loss along that step [65].

In order to ensure reliable simulation results one should sets small values for the parameter C_1 which admits values from 0 (detailed simulation) up to 0.2 (mean angular deflection $\theta \sim 37$ deg). The authors [65] consider that using $C_1 = C_2 = 0.05$ is a fairly conservative assumption for obtaining adequate results and should be kept if there is no gain in speed when using larger values. C_2 is effective only at high energies and also admits values in the range $0 \leq C_2 \leq 0.2$.

The simulation can also be speeded up by using large values for the cutoff energies W_{CC} and W_{CR} since they have a very week influence on the accuracy of the results. However, since these parameters mainly influence the simulated energy distributions, their maximum allowed values are determined by the desired energy resolution. For values of W_{CC} and W_{CR} smaller than the bin width used to tally the energy distributions, these quantities will be practically insensitive to the adopted values of these parameters. On the other hand if energy distributions are of no

interest, the recommendation is to set these cutoff energies to one hundredth of the typical energy of primary particles. It is important to note that for the sake of consistency W_{CC} and W_{CR} should not be larger than E_{abs} , the absorption energies of electrons and photons in the material, or otherwise one would lose electrons and photons with energies larger than its respective absorption energies (E_{abs}).

The absorption energies, on its turn, should have their values determined either by the experiment or by the required space resolution. An appropriate assumption is to choose E_{abs} values in order to guarantee that the residual range $R(E_{abs})$ of electrons and positrons is smaller than the typical dimensions of the volume bins used to tally dose or deposited charge distributions, if this is interesting for the user [65]. However, it is worth mentioning that the effect of these parameters can be better evaluated by running short simulations with increasing values of E_{abs} starting from 50 eV.

EGSnrc

The *Electron Gamma Shower* (EGS) system of computer codes is freely available (<http://irs.inms.nrc.ca/software/egsnrc/>) from the National Research Council of Canada (NRCC or NRC). Its last version is the EGSnrc [51], and also uses a class-II condensed history technique for simulating charged particle transport. The system is a general purpose package for Monte Carlo simulations of the coupled transport of electrons and photons in an arbitrary geometry and with energies above a few keV up to several GeV [51]. The transport of secondary electrons and bremsstrahlung photons is followed and explicitly simulated if the production energy is greater than the thresholds AE and AP respectively. The particle's histories

are terminated when their energies falls bellow the cutoff's *ECUT* (electrons) and *PCUT* (photons).

The EGSnrc system provides a set of user codes written in MORTRAN3 (an extended version of FORTRAN language) for a variety of tasks besides new user codes which use the EGSnrc C++ class library also known as *egspp* [97]. Some of these most widely used EGSnrc user-codes are [51]: **DOSRZnrc** which scores dose in a generalised cylindrical geometry; **CAVRZnrc** which is similar to DOSRZnrc but also scores a variety of quantities which are of specific interest to dosimetry calculation with ion chambers such as the correction factors A_{att} , A_{scat} and A_{wall} ; **CAVSPHnrc** which is identical to CAVRZnrc but for spherical geometries; **FLURZnrc** which scores particle fluence in cylindrical geometries; and **SPRZnrc** which calculates Spencer-Attix spectrum averaged stopping-power ratios for arbitrary media in cylindrical geometries [103].

The four EGSnrc C++ user codes also provided with the EGSnrc system are [97]: **cavity** that calculates the dose to the cavity of an ionization chamber and/or the A_{wall} correction factor and it implements most of the functionality of the original CAVRZnrc MORTRAN user code; **egs_chamber** which is an advanced EGSnrc application derived from the cavity user code for efficient chamber simulations [54]; **egs_fac** that is also an advanced EGSnrc application for directly calculating free air chamber (FAC) correction factors (cleaner and more efficient when compared with the complexity logic in cavity) [104]; and the **egs_cbct** user code for simulating cone beam CT scans, and that quickly estimates scatter contribution to an ideal detector

by means of sophisticated Variance Reduction Techniques (VRTs) and a smoothing algorithm [105].

In addition, the EGSnrc Monte Carlo code system of radiation transport is also composed by **BEAMnrc**, a general purpose code to simulate radiotherapy beams such as accelerators (with electrons and photon beams), ^{60}Co units, and x-ray units [96, 106]. BEAMnrc is an improved and EGSnrc-compatible version of the original BEAM package developed by NRC and the University of Wisconsin-Madison in the 1990s as part of the OMEGA (*Ottawa Madison Electron Gamma Algorithm*) project to develop 3-D treatment planning for radiotherapy. The package also includes the dose scoring utility **DOSXYZnrc**, a general-purpose Monte-Carlo EGSnrc user code for 3-dimensional absorbed dose calculations in cartesian volumes [103, 107].

All EGSnrc user codes described above allow the user to use a full BEAM simulation as a particle source (instead of using a stored phase space file or energy spectrum) in order to simulate realistic radiotherapy beams. Radiation sources can be defined as particles sampled from a BEAM treatment head simulation running concurrently with a particular simulation of the other codes. In this sense, source particles for EGSnrc codes are sampled from what would be the scoring plane during a normal run of the BEAM accelerator.

The *egs_chamber* user code

The egspc user code *egs_chamber* was designed by Wulff *et al* [54] for efficiently calculating dose to the cavity of an ionization chamber as well as the dose ratios of two correlated geometries that can be used for computing perturbation factors [97]. The code is derived from the *cavity* user code by implementing several variance

reduction techniques (VRTs) that dramatically improve the simulation efficiency for calculating ion chamber response and perturbation factors.

The main motivation for developing this kind of code was the prohibitively long time of the previous available tools, such as the *cavity* code, for MC calculations of ion chamber profiles inside a phantom irradiated by a large field [54, 97]. In this sense VRTs, such as, photon cross section enhancement (XCSE), intermediate phase-space storage (IPSS) of the properties of particles entering user defined regions, and correlated sampling (CS) are combined with the *cavity* code for generating the new code *egs_chamber*.

Although the *cavity* code already has two powerful VRTs (Photon splitting and Russian Roulette) that increase its efficiency for calculating cavity doses for any geometry describing an ion chamber, the calculation of perturbation factors and ion chamber doses at more than one position inside a phantom is extremely time consuming [54]. Therefore, the extension for implementing three new VRT's (XCSE, IPSS and CS) makes *egs_chamber* much more efficient for those kind of calculations.

Photon cross-section enhancement (XCSE)

For understanding XCSE variance reduction technique it is important to have in mind that typical phantom dimensions (e.g., 30 x 30 x 30 cm^3 for absolute dosimeter purposes) can be smaller than the mean free path length (*mfp*) of MeV photons in water (e.g., 45 cm for a 10 MeV photon) [54]. Based on this, the essential idea of XCSE, is to artificially increase the number of photon interactions by increasing the photon cross section Σ of a material in an arbitrary region and thus decreasing the

mfp. However, this requires the weight of the particles being decreased by the same factor in order to keep the results unbiased.

In *egs_chamber* this done in the following way [54, 98]: when a photon comes into a region whose cross section is enhanced by a factor b , the photon is split into an interaction portion (with fraction $1/b$) and a non-interacting portion (with fraction $1 - 1/b$). In this way, particles set in motion (electrons and/or scattered photons) by the interacting photon will carry a weight w_0/b where w_0 is the weight of the original photon. Then *Russian Roulette* game is played with survival probability $1/b$ for the scattered photons, and if they survive their weight is increased to w_0 . The electrons set in motion by the interacting photons and which also have weight w_0/b will be transported further and there are b times more such electrons than there would be in a simulation without XCSE. *Russian Roulette* is also played with the non-interacting (unscattered) portion of the incident photon with survival probability $1 - 1/b$ and the surviving photons will also carry again the initial weight w_0 .

Although this technique is similar to the *splitting technique*, which is also available in *egs_chamber*, the main advantage of XCSE technique as implemented in this code is the definition of a position dependent enhancement factor set by the user on a region-by-region basis [54, 97]. Figure 2–14 illustrates the use of this technique in *egs_chamber* [54].

On the other hand, the different cross section enhancement factors (b_i) set to individual regions of the geometry will set in motion electrons with different statistical weights. Electrons, e.g., generated outside of the CSE scoring region enters that region with a weight w_0 and these fluctuations can compromise the statistics of the

cavity dose. Because of this, the electrons generated by the interacting photons are handled in a different way. In order to equalize the weights of the electrons entering the region of interest, when an electron leaves one region with XCSE factor b_1 and moves into a region with XCSE factor b_2 , with $b_2 > b_1$, then the electron is split into b_2/b_1 copies with weight $w_0 b_1/b_2$. For the case where $b_2 < b_1$ *Russian Roulette* is played with survival probability b_2/b_1 and the surviving electrons have their weight increased to $w_0 b_1/b_2$.

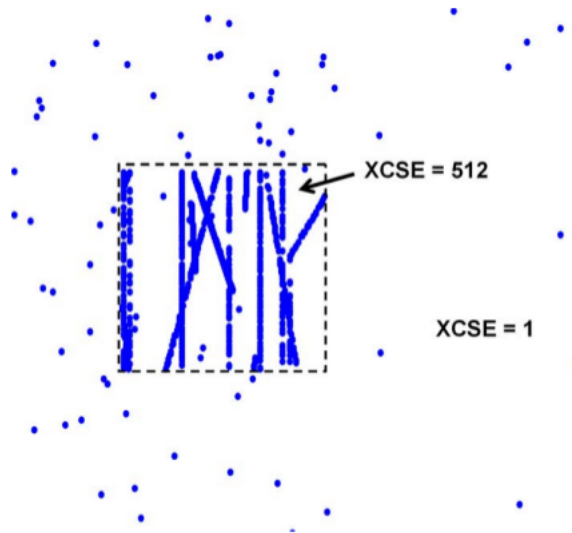


Figure 2–14: 2-D representation of the XCSE technique in *egs_chamber* by showing interaction sites (blue dots) of approximately 500 hundred 6 MeV photons. The box (dashed line) represents a small region inside the water phantom where the cross section is increased by 512. Reproduced from *Medical Physics*, "Efficiency improvements for ion chamber calculations in high energy photon beams", Wulff *et al*, vol 35, pp. 1328 - 1336, 2008.

As we can see from the example in figure 2–14, the technique is applied by using large XCSE factors and surrounding the chamber geometry with one or more extra

regions (shells). The optimum efficiency for a specific simulation should be however investigated by adjusting these two parameters (XCSE factors and size and shape of the shells).

Intermediate phase-space storage (IPSS)

The IPSS variance reduction technique allows one to store the particle properties (energy, position, direction, etc.) at a defined boundary and after using it for an arbitrary number of subsequent geometries [97]. The reason for using IPSS can be understood considering the calculation of a depth dose curve or profile inside a water phantom using a real ion chamber model, where each position of the chamber must be simulated separately [54]. Since only a small fraction of the overall geometry changes, the basic idea of IPSS consists of introducing an artificial volume, which surrounds all possible positions of the chamber needed for the dose calculations as tightly as possible. This artificial volume is used for scoring the phase space (particle type, energy, position, direction, statistical weight, etc.) of all particles entering it. In this way the history of the particles are immediately terminated as they enter the volume and the stored phase space will then be used as a source for all single chamber calculations at the different positions inside the phantom and thus avoiding unnecessary recalculations in all parts of the medium. In this sense, the user should define a "base geometry" composed by the phantom and the artificial volume for IPSS where the transport from the common simulation source starts and stops at the artificial IPSS boundary. Separate simulation geometries for describing the different chamber positions and which includes the phantom but not the IPSS volume are also defined. In these last geometries the transport of the particles will

be then subsequently performed and the dose to the cavity calculated. An important advantage of the implementation of this technique in *egs_chamber* is the use of the "on-the-fly" method, where the phase-space information is stored in memory instead of using phase space files and thus avoiding relatively slow speed of hard disk access besides other disadvantages related to the use of those files [54, 91]. Figure 2–15 illustrates the combined use of IPSS and XCSE techniques [54]. In order to efficiently combine the two techniques, a special handling of the electrons is necessary, as also can be seen in figure 2–15.

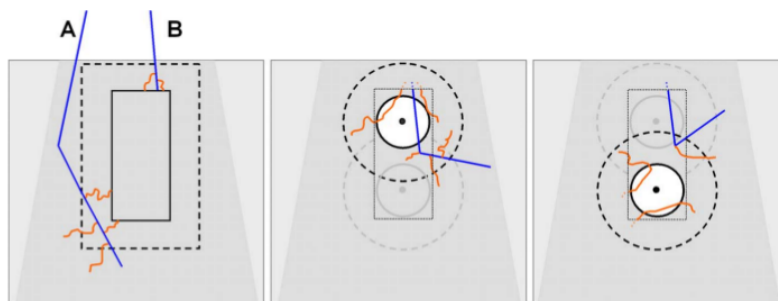


Figure 2–15: Representation of the combined application of IPSS and XCSE techniques in two positions of an ion chamber inside a phantom. The dashed line box and dashed circles represent the shells of phantom material with enhanced cross sections involving the IPSS volume (solid line box) and chamber (solid line circle) respectively. As soon as the particles get into the IPSS volume their transport is terminated and the phase space of photons and electrons is stored (left). This phase space is then used as a source at the two different positions of the ion chamber (middle and right). However, electrons that do not start inside the XCSE region of the respective ion chamber geometry (dashed circles) must survive a *Russian Roulette* game. We can see from the illustration that IPSS electrons originating from photon A will not survive the game for the first chamber position (middle) and neither electrons from photon B will survive for the second position (right). Reproduced from *Medical Physics*, "Efficiency improvements for ion chamber calculations in high energy photon beams", Wulff *et al*, vol 35, pp. 1328 - 1336, 2008.

Both chamber and IPSS volume are surrounded by shells of phantom material where the photon cross sections are enhanced and that overlaps each other. A *Russian Roulette* game is played with survival probability equals to the inverse of the XCSE factor with all electrons that do not start inside the XCSE region of the ion chamber geometry. Therefore, a large number of electrons will be only transported around the cavity for each position of the chamber [54].

Correlated sampling (CS)

This true VRT is similar to IPSS, but the phase space is scored in a set of user defined regions corresponding to parts of the chamber that differ (in composition details) from one geometry to another (correlated sampling regions). This is the case, for example, for the central electrode correction factor (P_{cel}) calculation where two "slightly" different geometries (with and without the electrode) are needed. Another difference in CS is that besides storing all those particle's properties mentioned in IPSS technique, it also stores the random number sequence and state. This allows one to maximize correlation besides decreasing the statistical uncertainties in dose ratios which are very useful for computing perturbation factors with large efficiency [54, 97, 98, 108, 109].

Figure 2–16 illustrates the use of CS technique [108], where the problem of interest is a comparison of the dose to the small region (cavity) into a phantom when this region is filled with different materials (e.g., water and air). The CS implementation allows one to calculate the dose to the CS region for both options (with water and air) in a single execution of the code, instead of performing the entire calculation twice.

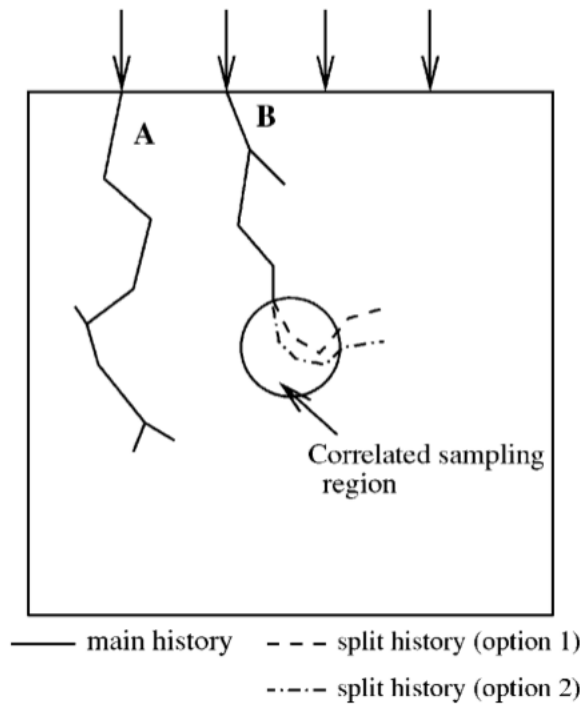


Figure 2–16: Representation of the correlated sampling method. Particle *A* represents a main history that is transported only once since it never enter the correlated sampling region (solid line circle). For particle *B* its main history (solid line) is transported only once, and thus only the split history (dashed lines) is repeated for each geometry option. Since the particle enters the CS region with the same parameters in both geometry options, it will follow similar trajectories and quantities (energy deposition) will be highly correlated. Reproduced from *Medical Physics*, "Efficiency improvements for ion chamber calculations in high energy photon beams", Wulff *et al*, vol 35, pp. 1328 - 1336, 2008.

For particles that travels through the phantom without entering the CS region, the simulation is performed only once which results in significant time savings. This is the case of the particle's track *A* shown in the figure. For tracks like *B*, the particle is transported as a main history only until it reaches the boundary of the CS region,

where the particle data and state of the random number generator are then stored. From this point, the transport of the particle and any secondary particles continues as before, and the quantities of interest, like absorbed dose, are then scored for the first geometry option (e.g., water). After finishing the transport of the particle and all its descendants, the particle data are restored to the point in the main history where the split began and the particle transport initiates again but now with the material in the region corresponding to the second geometry option. This process can be repeated many times for many different geometries available, and a new main history initiates only when all transport of the first history is completed [108].

As it has already been pointed out, since particles that never get into the CS region will be transported only once, there will be large savings in execution time for codes that implement this technique. In addition, even if the precision in absolute terms on the quantity is no better than one single simulation, the reduction in the uncertainty on the ratio of scored quantities in the different geometries will provide the greatest gain in computing efficiency [98, 108].

CHAPTER 3 Methodology

3.1 Calculations of k_Q for reference dosimetry using PENELOPE

In this section, the methodology of use of the code PENELOPE to calculate stopping power ratios, the perturbation and beam quality correction factors for the NE2571 ionization chamber will be described.

3.1.1 Parameters and features of PENELOPE code

In this part of the work simulations were performed using the MC code PENELOPE 2008 version [65] described in section 2.6.3. In particular, for calculating chamber correction factors, simulations were also performed by using the package *clonEasy* [110] which allows the use of parallel simulations in different computers.

ClonEasy consists of a set of Linux scripts and auxiliary FORTRAN programs that implement Secure Shell-based communication between a "master" computer and a set of "clones" [110]. In this research *clonEasy* was used together with PENELOPE for performing parallel simulations on a LINUX cluster in which up to 20 CPU's could be used simultaneously. Simulation parameters in PENELOPE were set in order to guarantee a reasonable compromise between speed and accuracy for all calculations.

The average angular deflection parameter, C_1 , and maximum average fractional energy loss parameter, C_2 , between two consecutive hard elastic events were set to $C_1 = C_2 = 0.02$ in all regions of interest, i.e., dose scoring voxels regions and ion chamber geometries. For the other regions of the water phantom these parameters

were fixed to $C_1 = C_2 = 0.1$. The threshold energies for hard inelastic interactions, W_{CC} , and hard bremsstrahlung emission, W_{CR} , were set to $W_{CC} = W_{CR} = 10$ keV for all regions except the water phantom where $W_{CC} = W_{CR} = 100$ keV were used. The absorption energies were also set to $E_{abs}(e^-, e^+) = E_{abs}(\gamma) = 10$ keV for the regions of interest and 100 keV for the rest of the water phantom.

3.1.2 Radiation sources and the TPR_{10}^{20} beam quality specifier

Radiation sources were defined in the input-file *user.in* of PENELOPE by using published photon spectra found in the literature for ^{60}Co [111] and 4, 6, 10 and 25 MV nominal energies linear accelerators [112]. In this sense, radiation sources were assumed to be point sources emitting photons with those corresponding published spectra.

In this study the TPR_{10}^{20} was used as a beam quality specifier. Since the radiation sources used do not correspond to full beam Monte Carlo models of accelerators, where contaminant electrons can be take into account, values of $\%dd(10)_x$ were calculated according to the geometrical set-up described in TG-51. The TPR_{10}^{20} was then calculated from the $\%dd(10)_x$ by using the equation provided by Kalach and Rogers [113]:

$$TPR_{10}^{20} = -0.8228 + 0.0342(\%dd(10)_x) - 0.0001776(\%dd(10)_x)^2 \quad (3.1)$$

For the determination of $\%dd(10)_x$ values, absorbed doses in a $30 \times 30 \times 30 \text{ cm}^3$ water phantom were calculated using square scoring voxels of 0.2 cm thickness and 0.5 cm width and $N = 5 \times 10^9$ primary histories.

3.1.3 Phase space file methodology for reducing time simulations

In this subsection a methodology is presented for saving CPU time when calculating absorbed doses at reference depths in a water phantom irradiated by photon beams. On a first step simulation, the radiation particles that reach the geometric region of a 5 cm diameter and 1.6 cm high cylinder are stored in a phase-space file (psf) for each of the five energy spectrum used in this study. This is accomplished in PENELOPE by setting the simulation parameters $IPSF = 1$ and $IDCUT = 0$ in the input-file *user.in* for the corresponding body where the psf should be stored. Setting those values for the parameters means that a phase space file is created ($IPSF = 1$) storing information of the particles, such as, type, energy, position, direction and statistical weight, as soon as they enter the artificial volume defined by the cylinder described above, and where their transport is immediately terminated ($IDCUT = 0$). In this sense the time needed for tracking the particles in regions of the phantom different from those ones of interest (ionization chamber or scoring dose voxels) is spent only once for each energy desired.

In a second step, the stored psf can be used as a source for all single chamber and dose to water calculations which geometry is involved by the artificial volume used to store the psf. Absorbed energies to water in a disc with 1 cm radius and 0.025 cm thickness using the beam (full spectrum) and the psf were compared in order to test the methodology. Calculations were done at 5 cm depth for ^{60}Co and at 10 cm depth for mega-voltage photon beams and using $N = 3 \times 10^9$ histories in both situations. The dose scoring voxel as well as the region around it, defined by the artificial volume used to store the psf, were considered as the region of interest

and then simulation parameters were assigned in order to allow a detailed simulation ($C_1 = C_2 = 0.02$ and $W_{CC} = W_{CR} = E_{abs}(e^-, e^+) = E_{abs}(\gamma) = 10$ keV). For the rest of the phantom larger values of those parameters were assigned for condensed simulation ($C_1 = C_2 = 0.1$ and $W_{CC} = W_{CR} = E_{abs}(e^-, e^+) = E_{abs}(\gamma) = 100$ keV).

3.1.4 Restricted stopping-power calculations

In order to calculate perturbation factors by means of equation 2.16, ratios water-to-air of average mass restricted stopping-powers were also calculated using PENELOPE code. PENELOPE package provides a FORTRAN program called TABLES.f which gives interpolated values of total cross sections, mean free paths, ranges of particles and also detailed tables of fundamental quantities such as stopping powers that are written in a number of separate files with the extension '.tab'. The material-data file (e.g., water.mat, air.mat) must be built previously by running the code *material* (see section 2–13). Arrays of unrestricted and restricted stopping powers vs. energy for each medium (water and air) were then built by running the executable file *tables.exe*.

For calculating average values of restricted stopping powers for each medium and obtaining the ratio between them, a program was written using MATLAB and is shown in Appendix A. The program reads the arrays *Energy vs. Stopping Power* and *Energy vs. Fluence*, and then calculates the water to air ratio of average restricted stopping powers according to equation 2.14. The array *Energy vs. Fluence* was built by sampling the electron fluence in a water disc with 1.0 cm radius and 0.025 cm thickness at reference depths in the central axis of the beam with an SSD = 100 cm at the surface of a 30 cm x 30 cm x 30 cm water phantom.

3.1.5 Absorbed doses and correction factors calculations

Equations 2.16 and 2.30 can be combined to provide a relation which allows one to calculate the beam quality conversion factor, k_Q , directly using Monte Carlo simulations as a dose ratio at two beam qualities and given by [52, 55]:

$$k_Q = \left(\frac{D_w}{D_{ch}} \right)_{60Co}^Q \quad (3.2)$$

In this way, k_Q can be determined by calculating the absorbed doses for each of the four terms in equation 3.2, which relates the absorbed dose to water in the absence of the chamber, D_w at the depth corresponding to the point of measurement, to the absorbed dose to air averaged over the cavity volume of the ion chamber, D_{ch} , as illustrated in figure 3–1(a). The perturbation factors, as defined in equation 2.16 were independently evaluated by calculating ratios of the NE2571 ionization chamber's cavity doses with different constructive details as illustrated in figure 3–1, as well as, ratios between doses to those chamber cavities and doses to water [52, 53, 76].

Absorbed doses to water, D_w , were calculated using a reference volume modelled as a disk of water with 0.025 cm thickness and 1 cm radius, centered on the point of measurement in the phantom. Studies in the literature have shown that no difference is observed within a statistical uncertainty $\leq 0.05\%$ in the calculated dose using voxels with thickness below 0.05 cm [52, 79].

Based on the geometry definitions described above, perturbation factors for the NE2571 farmer chamber were calculated as follow:

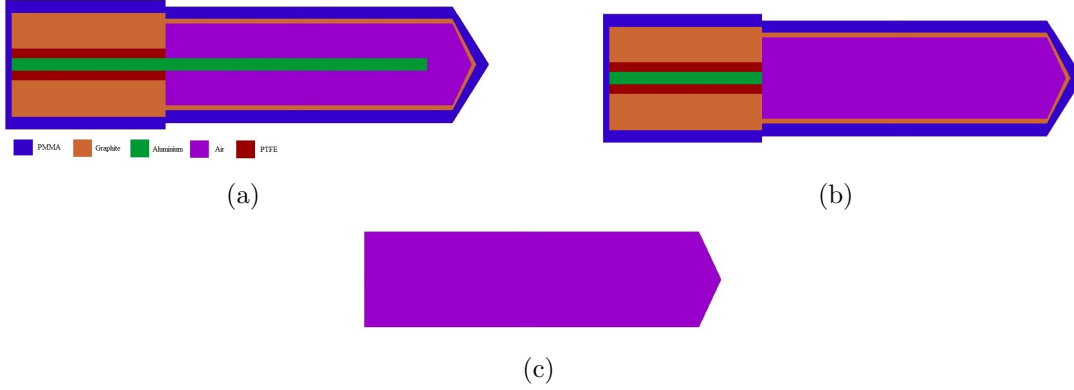


Figure 3–1: Simulation geometries of the NE2571 farmer chamber built with the PENGEOM package of PENELOPE for calculating correction factors. In (a) a complete geometry of the chamber (for calculating D_{ch}) is shown in comparison with the geometry without electrode (b) (for calculating D_{noel}) and also with the geometry corresponding only to the bare air cavity of the chamber in (c) (for calculating D_{air}).

$$P_Q = \left(\frac{D_w}{D_{ch}} \right) / \left(\frac{\bar{L}_\Delta}{\rho} \right)_{air}^{water} \quad (3.3)$$

$$P_{repl} = \left(\frac{D_w}{D_{air}} \right) / \left(\frac{\bar{L}_\Delta}{\rho} \right)_{air}^{water} \quad (3.4)$$

$$P_{cel} = \left(\frac{D_{noel}}{D_{ch}} \right) \quad (3.5)$$

$$P_{wall} = \left(\frac{D_{air}}{D_{noel}} \right) \quad (3.6)$$

where D_{noel} is the dose averaged over the air cavity of the chamber without electrode (made of air) as illustrated in figures 3-1(b); and D_{air} is the dose averaged over the bare air cavity of the chamber as illustrated in figure 3-1(c) with electrode made of air and with all the other parts of the chamber made of water (without wall, sleeve and stem).

The NE2571 Farmer-type cylindrical chamber with a volume of 0.6 cm^3 was modelled by means of quadric surfaces through the package PENGEO. Dimensions of this chamber were taken from data available in the literature [5,52,114]. Its cavity has a diameter of 0.64 cm and 2.4 cm length. The chamber has also a 2.06 cm aluminium central electrode with diameter of 1 mm. Its graphite wall has a thickness of 0.061 g/cm^2 . Since the NE2571 itself is not waterproof, the model also includes a 1 mm PMMA waterproofing sleeve. The chamber stem modelled here also includes portions of aluminium, graphite, and polytetrafluorethyl (PTFE)(TEFLON) [52].

All absorbed energy quantities (for chamber geometries and water disc) were calculated in a $30 \times 30 \times 30 \text{ cm}^3$ water phantom at the point of measurement on the central axis of the beam and at depths of 5 cm for ^{60}Co and 10 cm for mega-voltage beams. In a first step, the phase space file for all the five energy beams used in this study was stored according to the methodology presented in subsection 3.1.3 for $N = 5 \times 10^8$ primary histories. Besides looking for good statistics on dose calculations, this number of primary histories for storing the psf's was chosen in order to guarantee the accuracy of the sampled spectrum and at the same time to save memory space in computer hard disk. This optimization was accomplished by comparing particle fluences sampled in the artificial volume used to store the psf with 5×10^7 , 5×10^8 and

1×10^9 primary histories. The spectrum with $N = 5 \times 10^8$ primary particles showed uncertainty on energy fluence distribution closer to those obtained by $N = 1 \times 10^9$ and phase space files considerably smaller. Although all the spectra have presented the same distribution within uncertainties, electron energy fluence distributions obtained with $N = 5 \times 10^7$ primary histories presented the largest uncertainties when compared with $N = 5 \times 10^8$ and $N = 1 \times 10^9$, as can be seen from figure 3–2 for the four photon beams investigated. Figure 3–3 also shows the photon fluences of those stored psf’s.

In a second step simulation, the phase space files were used as radiation sources in PENELOPE for calculating the absorbed dose quantities. In order to improve statistics, the *Splitting* variance reduction technique was used with $N_{split} = 100$. In addition, parallel simulations in 10 different computers were also used with the package *ClonEasy* according to the methodology described by Badal and Sempau [110].

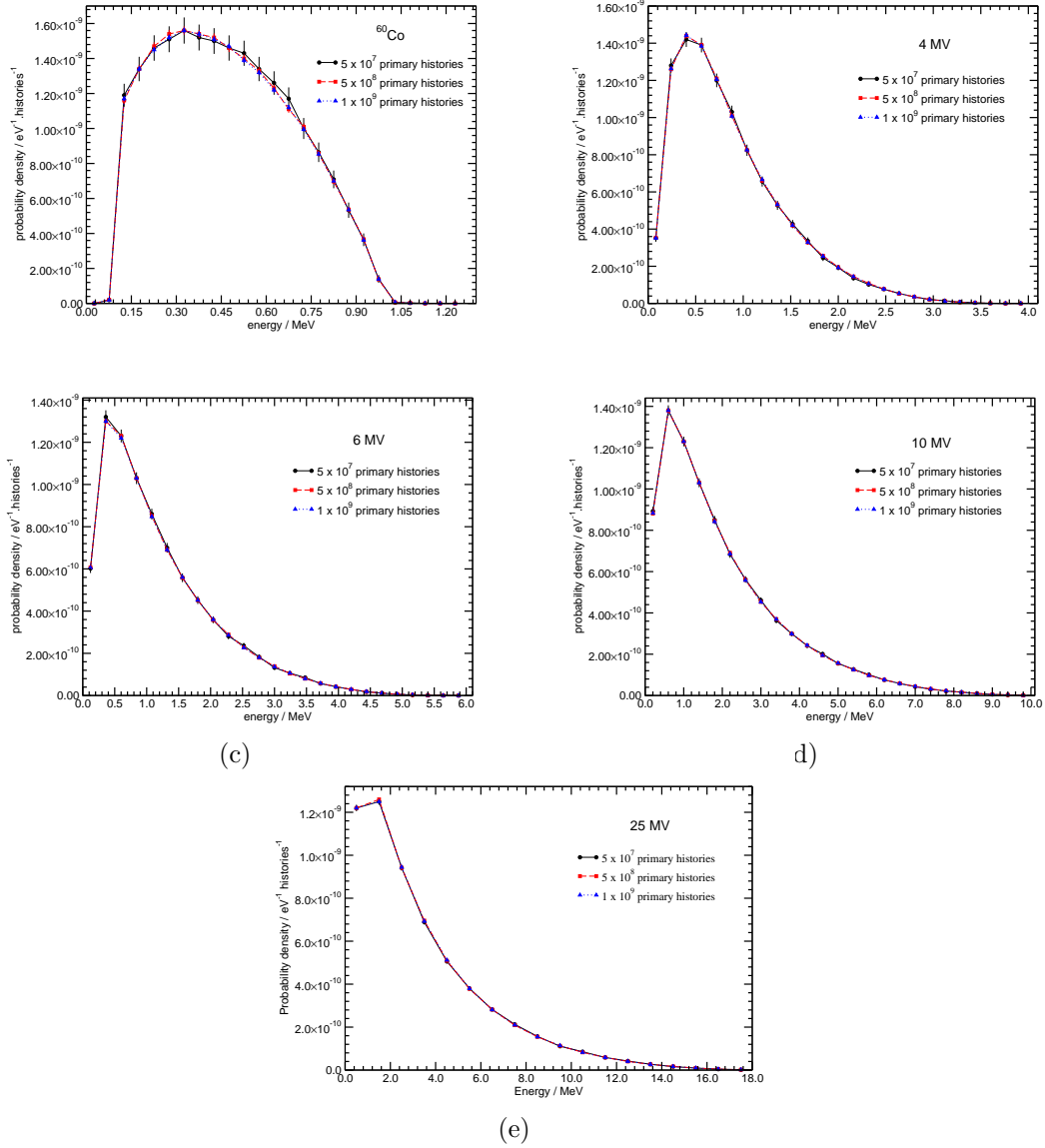


Figure 3-2: Comparison of electron energy fluence distributions of the phase space file stored with different numbers of primary histories for ^{60}Co (a), 4 MV (b), 6 MV (c), 10 MV (d) and 25 MV (e) photon beams.

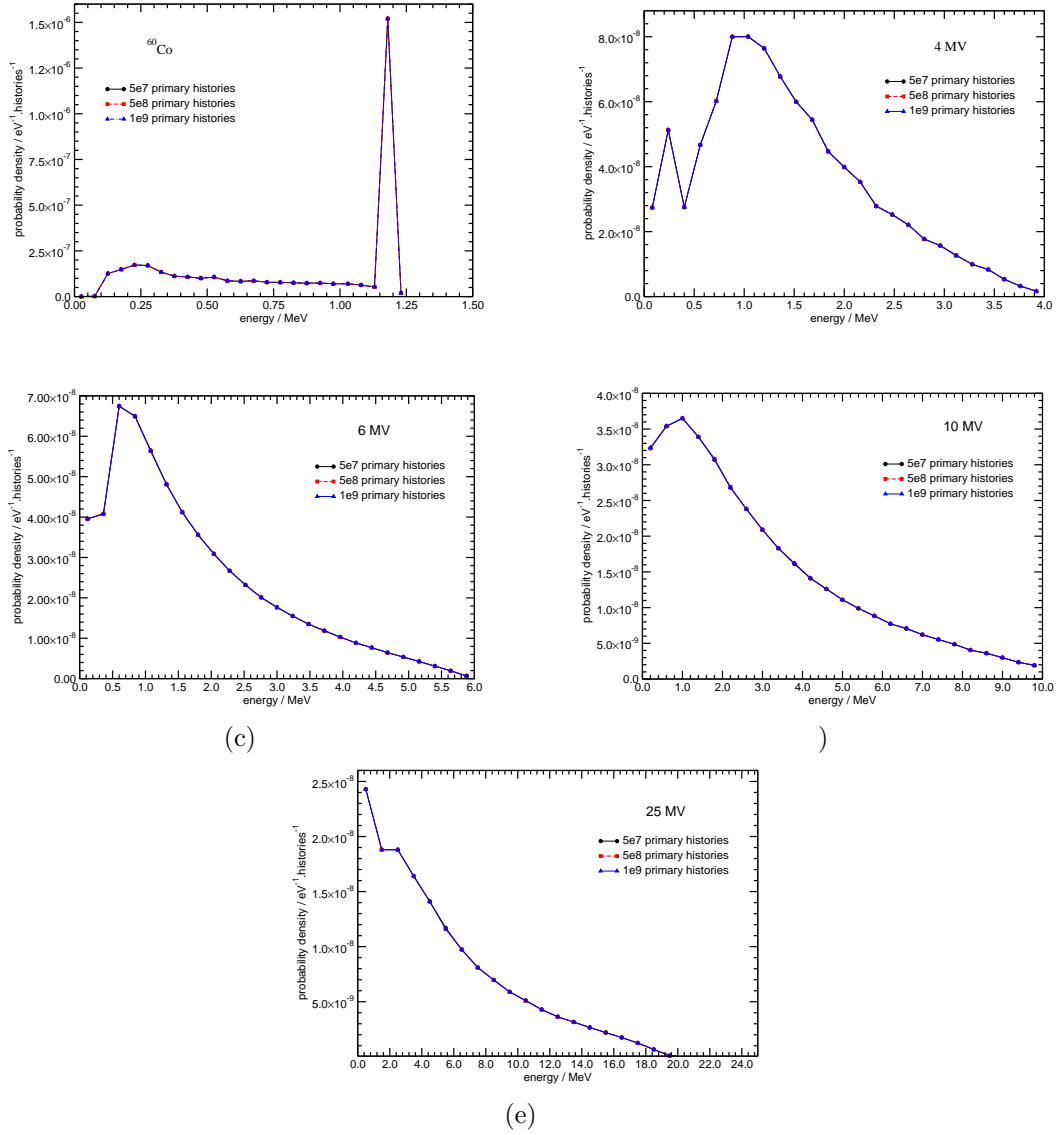


Figure 3-3: Comparison of photon energy fluence distributions of the phase space file stored with different numbers of primary histories for ⁶⁰Co (a), 4 MV (b), 6 MV (c), 10 MV (d) and 25 MV (e) photon beams.

In *ClonEasy* each computer clone provides a quantity q_k (with $k = 0, 1, \dots, K - 1$) with variance $\sigma^2(q_k)$ after simulating N_k histories. The outcome results are then combined in order to provide the global average value (\bar{q}) and its standard deviation ($\bar{\sigma}$) given by [110]:

$$\bar{q} = \frac{1}{N} \sum_{k=1}^{K-1} N_k q_k \quad (3.7)$$

and

$$\sigma(\bar{q}) = \frac{1}{N} \sqrt{\sum_{k=1}^{K-1} N_k^2 \sigma^2(q_k)} \quad (3.8)$$

with

$$N = \sum_{k=1}^{K-1} N_k \quad (3.9)$$

where N is the total number of simulated histories. In order to guarantee the statistical independence of the output from the different executions, each computer clone must use an independent sequence of pseudo-random numbers. Our calculations were done using equations 3.7, 3.8 and 3.9 with $K = 10$ and $N_k = 5 \times 10^8$.

3.2 Buildup and surface calculations using the EGSnrc system

In this section the methodology used to evaluate parallel plate chambers response at the surface of water phantoms and in the build-up region of photon beams will be described. Parallel simulations with the EGSnrc code system were performed on a LINUX cluster in which up to 600 CPU's could be used simultaneously.

3.2.1 Radiation sources

In this part of the work, a realistic model of the Elekta SL25 linear accelerator was simulated using the BEAMnrc package [96, 106] for producing high energy

photon beams with nominal energies of 6, 10 and 25 MV. A BEAMnrc model of the Eldorado 6 ^{60}Co treatment unit [111] was also employed. The realistic photon beams were produced in order to have a 10 x 10 cm² field at the surface of the water phantom with an SSD of 100 cm. The beams then produced are collected and used as an input for the other EGSnrc user codes. Table 3–1 shows the radiation sources used in this study along with our calculated beam quality specifiers.

Table 3–1: Beam quality specifiers for the Elekta SL25 and ^{60}Co Eldorado 6 full BEAMnrc models. Values of $\%dd(10)_x$ are calculated using DOSRZnrc code, and TPR_{10}^{20} are calculated with Kalach and Rogers formula.

Beam	Nominal energy (MV)	Beam quality specifier	
		$\%dd(10)_x$	TPR_{10}^{20}
^{60}Co Eldorado 6	-	58.59 ± 0.04	0.571
Elekta SL25	6	68.02 ± 0.06	0.682
	10	73.90 ± 0.05	0.735
	25	84.30 ± 0.05	0.798

The photon component of the percent depth-dose at 10 cm depth, $\%dd(10)_x$, was calculated using DOSRZnrc code [103] for obtaining a depth dose curve along the central axis of a cylindrical water phantom with a radius of 15 cm radius and 30 cm height. The absorbed doses to water are calculated in individuals disks with 0.5 cm

thickness and 2 cm radius. Full BEAMnrc models are used as input source in DOSRZnrc where only photons particles are selected to irradiate the phantom. In addition, the ECUT value for the air between the phantom and the accelerator head is set to 30 MeV in order to get rid of contaminant electrons. Tissue-phantom ratios at 20 and 10 cm for a 10 x 10 cm² field at the depth of measurement, TPR_{10}^{20} , were calculated from Kalach and Rogers formula [113] and given by equation 3.1.

3.2.2 Calculation of surface water depth doses

Percentage depth dose curves were calculated at the surface of a water phantom for depths $0.5 \mu\text{m} \leq z \leq 0.1 \text{ mm}$ in order to evaluate the dose gradient at those superficial depths in high energy photon beams. Absorbed doses to water were calculated with the DOSRZnrc code using cylindrical dose-scoring voxels with 2 cm radius and thickness of 0.001 mm, 0.002 mm, 0.2 mm and 5 mm. The voxels were then distributed along the central axis of a cylindrical water phantom with 15 cm radius and 30 cm height. The simulation geometry was set to have a 10 x 10 cm² field at the surface of the phantom with an SSD = 100 cm for all the four beams produced with full BEAMnrc models of the accelerators mentioned previously. The cutoff energies (ECUT, PCUT) and production thresholds (AE, AP) were set to 521 keV for electrons and 10 keV for photons. A total of 2×10^9 histories were used in order to get uncertainties lower than 0.5% at all depths. In addition, cross-section enhancement factors of 256, 128, 64 and 16 for ⁶⁰Co, 4 MV, 10 MV and 25 MV beams respectively were set to central region of the phantom within a radius of 2.5 cm.

3.2.3 Evaluation of extrapolation chambers response

In this part of the work, extrapolation chambers were modelled in order to evaluate the response of this kind of ionization chamber for assessing surface and buildup doses and compare with experimental results from the literature [1, 2, 29–31, 64, 115]. The C++ class library egsp for the EGSnrc code system was used to model the geometry of two extrapolation chambers used by Nilson and Montelius [1] and Gerbi and Khan [2] (PTW 30-360) for measuring surface doses in polystyrene phantom in high energy photon beams. Those two chambers will be referred here as ExCh 1 and ExCh 2, respectively, and some details of its geometries are given on table 3–2. Further information can also be found elsewhere [1, 2, 44, 47].

Table 3–2: Physical characteristics of the extrapolation chambers modelled in this study according to data from the literature. The chambers are designated here as ExCh 1 (Nilson and Montelius) and ExCh 2 (Gerbi and Khan PTW 30-360). Active radius of the cavity in mm are given together with the total (active and guard region) radius in parentheses. The range of electrode separations (s) shown on third column corresponds to the minimum and maximum values used experimentally.

Extrapolation chamber	Cavity		Window	
	Radius (mm)	Plate separation range (mm)	Material	Thickness (mg/cm ²)
Nilson and Montelius (ExCh 1)	14 (25)	0.5 - 10	Graphited-coated on Mylar	0.976
Gerbi and Khan (PTW 30-360) (ExCh 2)	15 (30)	0.5 - 5.0	Graphited-coated on Mylar	2.61

The geometry of a PTW Markus chamber [57] was also modelled for comparing the results with those obtained with the extrapolation chambers following the experimental methodology of the authors [2]. Figure 3–4 shows the image of the modelled extrapolation chambers made with the geometry viewer provided with the geometry package of egs++. Dashed line in the air cavity illustrates the active air region. Several similar models were used for representing the chambers with different electrode separations.

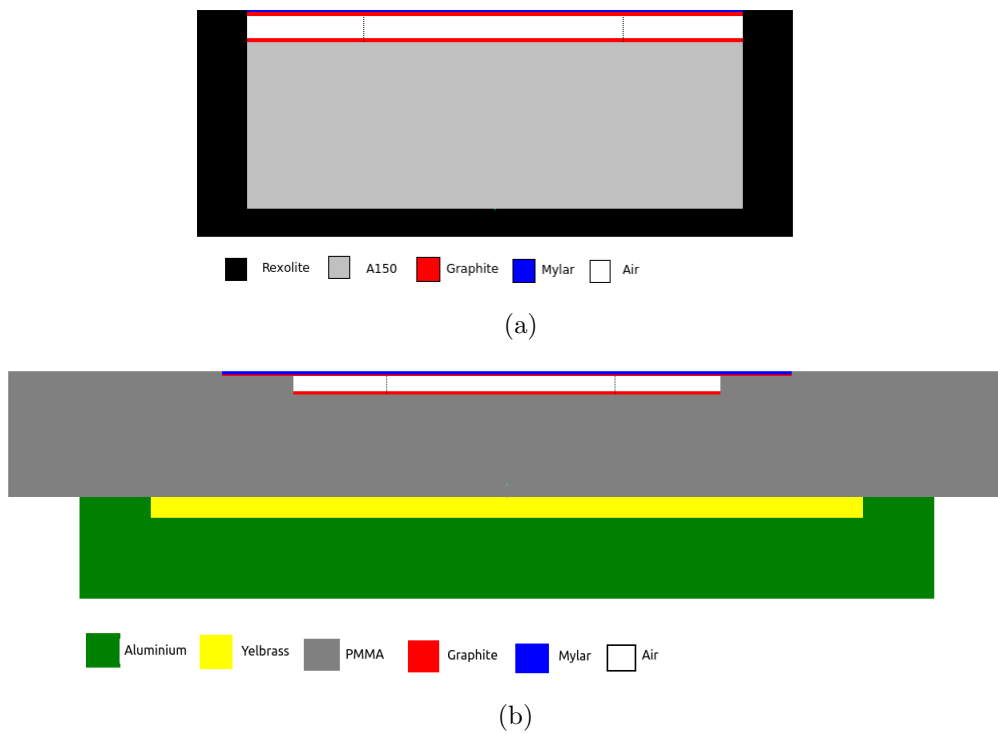


Figure 3–4: Monte Carlo models of the extrapolation chambers used by Nilson and Montelius (a) which will be referred here as ExCh 1, and the PTW 30-360 used by Gerbi and Khan (b) referred as ExCh 2. Some of its characteristics are given on table 3–2.

The effective point of measurements are taken at the inside front face of the chamber window, which allows one measuring surface doses at approximately $z = 0.01$ mm (ExCh 1) and $z = 0.03$ mm (ExCh 2).

The `egs_chamber` user code was used for running independent simulations for each one of the different plate separations (s) of the chambers in a $30 \times 30 \times 30$ cm³ polystyrene phantom. In our Monte Carlo model of the extrapolation chambers the overall thickness of the chamber were kept constant and equals to 4 cm for the ExCh 1 and 5.6 cm for the ExCh 2 for the different plate separations used. For the ExCh 1 chamber 5 different plate separations between 0.1 and 0.9 mm and 10 plate separations between 1.0 and 10.0 mm were used. For the ExCh 2 chamber evaluation of the response were made for 5 different electrode separations between 0.1 and 0.5 mm and 6 plate separation between 1 and 5 mm. Full beam simulations for ⁶⁰Co, 6 MV, 10 MV and 25 MV were simulated with BEAMnrc and used as a source in the `egs_chamber` input files. Calculations were performed with the chambers at the surface of the phantom and at different depths of the buildup region in order to evaluate the influence of the electrode separations.

Perturbation factors were also calculated as a function of depth z in the build-up region in order to understand their contribution in chamber response for the different plate separations. By making use of correlated sampling technique, `egs_chamber` allows one to calculate the wall perturbation factor P_{wall} , in the same single run used to calculate the chamber response. This is accomplished by defining a second chamber geometry, in the same input file, where each material of the chamber, except the air cavity, is replaced by the phantom material (polystyrene in this case). The

fluence perturbation factor, P_{fl} , was calculated according to equation 3.4. The water to air restricted stopping-power ratios needed to calculate P_{fl} were calculated in this study using the SPRZnrc user code.

Transport cutoff energies in the chambers response simulations were set to $AE = ECUT = 521$ keV (10 keV kinetic energy) and $AP = PCUT = 10$ keV. Variance reduction techniques available in `egs_chamber`, as described in subsection 2.6.3, were set on in order to increase simulation efficiency. Cross-section enhancement factors of 256, 128, 64 and 32 were used on a region by region basis for ^{60}Co , 6 MV, 10 MV and 25 MV beams respectively. In this sense, the entire chamber as well as the air above the phantom and a region involving the chamber with thickness of 0.5 cm (for ^{60}Co) and 1.0 cm (for x-rays beams) were considered as enhanced regions. Survival probability of 1/512 was set for applying Russian Roulette to electrons that could not reach the cavity or that could not leave its current region. Other transport parameters were set to their default values in the current version of `egspp/EGSnrc`.

3.2.4 Monte Carlo dose conversion factors for parallel plate chambers

In this part of the study, the response of parallel plate ionization chambers was investigated in the build-up region and at the surface of water and solid water (RMI-457) [5] phantoms in photon beams. Simulations were performed using the `EGSnrc` [51,86] Monte Carlo code system with the `egs_chamber` user code from Wulff et al [54]. All geometries were modelled using the `egs++` geometry package [116]. Four parallel plate ionization chambers commonly used in clinics, PTW Roos, IBA NACP-02, Exradin A10 and P11TW were modelled according to data from manufacturer [57].

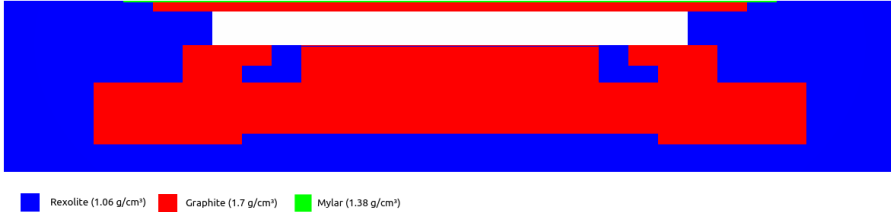
The main specifications of those chambers are given in table 3–3 and their Monte Carlo schemes are shown in figure 3–5.

Table 3–3: Major dimensions and materials for the four plane-parallel plate ion chambers investigated in this study. The radius of the active region of the chambers are given in the fourth column with the total radius (active and guard region) in parenthesis. Chamber materials are MYLAR, graphite (Gr, 1.7 g/cm³ density), rexolite (cross-linked polystyrene, Rex), air-equivalent plastic (C552), polyoxymethylene (POM, trade name Delrin), polystyrene-equivalent plastic (D400), Kapton and polymethylmethacrylate (PMMA). The abbreviation Gr’d refers to a graphited material, i.e., a thin layer of graphite applied to the material in question.

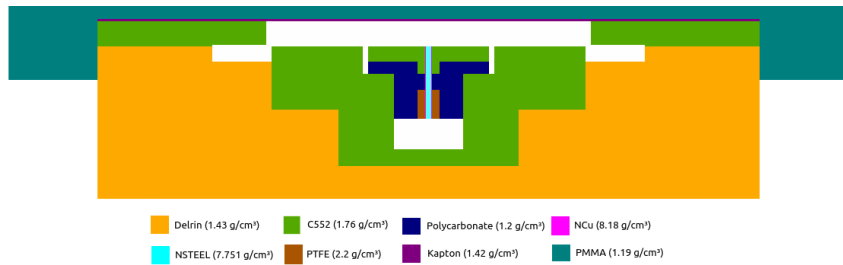
Chamber	Volume (cm ³)	Cavity		Window		Wall materials	Collector
		Depth (mm)	Radius (mm)	Material	Thickness (mm)		
Roos	0.384	2	7.8(12)	Gr’d/PMMA	1.1	PMMA	Gr’d/PMMA
NACP-02	0.157	2	5(8)	MYLAR Gr (2.25 g/cm ³)	0.1 0.5	Gr/Rex	Gr’d/Rex
A10	0.050	2	2.8 (7.3)	Kapton	0.03	C552/POM	C552
P11TW	0.920	3	9.9 (14.3)	Kapton	0.03	D400/POM	D400



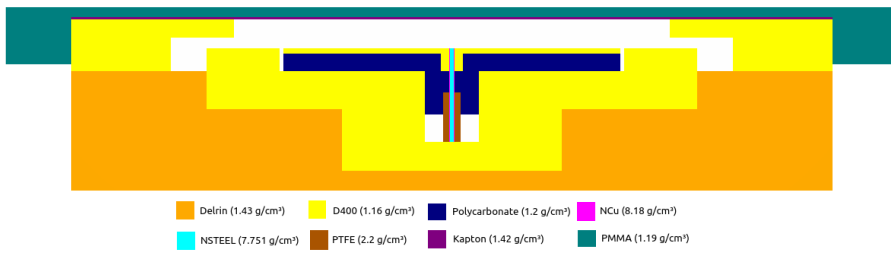
(a)



(b)



(c)



(d)

Figure 3–5: Monte Carlo models of the Roos (a), NACP02 (b), A10 (c) and P11TW (d) plane parallel plate chambers created with the geometry viewer package of EGSnrc C++ class library. Main materials that compose the chambers are indicated in the legend with their corresponding density.

Variance reduction techniques such as photon cross-section enhancement and correlated sampling were employed following the methodology of Wulff *et al* [54] to increase efficiency of simulations. The cutoff energies and production thresholds were set to 521 keV for electrons and 10 keV for photons. All the other Monte Carlo transport parameters were set to their default values.

Calculations were accomplished in two distinct depth regions of the phantom, named in this study, as surface region, which goes from 0.03 mm depth until 1.03 mm, and build-up region corresponding to depths between 1 mm and the depth of maximum dose in each photon beam.

Absorbed dose-to-air in the ion chamber averaged over the cavity volume, D_{ch} , was calculated with `egs_chamber` at several depths in only one run using the *input-loop* feature of `egs++` library. Russian Roulette option of `egs_chamber` for electrons that cannot reach the cavity was used with a survival probability of 1/512. Absorbed dose-to-water (D_w) values were calculated for a disk of water centered at depths corresponding to the effective point of measurement of the chambers in a 30 x 30 x 30 cm³ water phantom. Water disks had a thickness of 0.025 cm and radius equals to the active radius of each chamber. Following the methodology of Sempau *et al* [83], a unique chamber- and quality-dependent factor $f_{c,Q}$ was calculated as a function of depth for each chamber at the surface and in the build-up region of water phantom according to:

$$f_{c,Q} = \frac{D_w}{D_{ch}} \tag{3.10}$$

Therefore, the beam quality correction factor, k_Q , can also be determined as a function of depth, by making the ratio of dose-to-water conversion factors in two beam qualities and given by:

$$k_Q = \frac{f_{c,Q}}{f_{c,60Co}} \quad (3.11)$$

We can see from table 3-3 that the Exradin A10 and P11TW ion chambers have the thinnest window thickness between the chambers investigated. However, both of them need a water-proofing cap when used in water phantoms, which in turn increases their window up to 1 mm water equivalent thickness. In this sense, in order to investigate the response of those chambers at depths less than equal 1.0 mm, a 30 x 30 x 30 cm³ solid water phantom was used. Surface ($0.03 \text{ mm} \leq z \leq 1.03 \text{ mm}$) dose to water conversion factors were then calculated for those chambers by making the ratio between the absorbed dose to water (D_w) at the corresponding EPOM of the chamber and the dose to its air cavity (D_{ch-SW}) in solid water. For depths $z \geq 1 \text{ mm}$, all chambers responses were simulated in a 30 x 30 x 30 cm³ water phantom.

CHAPTER 4 Results and Discussions

4.1 k_Q and correction factors calculations with PENELOPE

In this section we are going to present and to discuss the results related to the calculations of perturbation and beam quality correction factors in reference conditions with the Monte Carlo code PENELOPE.

4.1.1 The TPR_{10}^{20} beam quality specifier

Table 4–1 shows our MC calculated values for the $\%dd(10)_x$ beam quality specifier with its relative statistical uncertainty. For comparison, the table also shows the values calculated by Muir and Rogers [55] and Wulff *et al.* [52] for the same beams.

The largest differences were found for the 4 MV beam of the Varian Clinac accelerator which were 2.3% and 1.9% compared to the values calculated by Muir and Rogers and Wull *et al.* respectively. For the other energy beams deviations were less than 2% when compared with both references. Differences in values set for the simulation parameters as well as the geometry and methodology used for absorbed dose calculation using the two codes can possibly account for the deviations between our values and those reported by the referred authors. The use by the authors of a scoring voxel with radius twice wider than that one used in this study can also explain the better statistics on their results. On the other hand, the discrepancies contrast with the agreement found when comparing our calculated beam quality correction

factors with those obtained by the same authors and using the same sources as will be shown further in this section.

Table 4–1: The photon component of the percentage depth-dose at 10 cm depth ($\%dd(10)_x$) for a 10 x 10 cm² field on the surface of the water phantom as a beam quality specifier for the radiation sources used in this study. Our calculated values (third column) are compared with those obtained by Muir and Rogers (fourth column) and Wulff *et al.* (last column). The relative difference with our values are shown between parentheses. Maximum relative statistical uncertainties on Muir and Rogers and Wulff *et al.* values are 0.1% and 0.3% respectively.

Beam	Nominal energy (MV)	$\%dd(10)_x$		
		This work	Muir and Rogers [55]	Wulff <i>et al.</i> [52]
⁶⁰ Co	-	57.4 ± 1.2%	58.4 (1.7%)	58.4 (1.7%)
Varian Clinac	4	64.1 ± 0.9%	62.7 (2.3%)	62.9 (1.9%)
	6	66.7 ± 1.1%	66.5 (0.3%)	66.2 (0.8%)
	10	74.9 ± 0.8%	73.8 (1.5%)	74.2 (1.0%)
Elekta SL25	25	83.5 ± 0.7%	82.8 (0.9%)	83.7 (0.2%)

Table 4–2 shows the TPR_{10}^{20} beam quality specifier calculated in this study from the $\%dd(10)_x$ values shown in table 4–1 and by using equation 3.1. That equation was also used by Muir and Rogers for calculating TPR_{10}^{20} from $\%dd(10)_x$ values which are shown in the fourth column of table 4–2. Wulff *et al.* made direct calculations of the TPR quality index defined according to IAEA dosimetry protocol, and their values are shown in the fifth column of table 4–2. The last column shows the values

from Erazo and Lallena [58] who made calculations of the ratio of percentage depth doses at 20 cm and 10 cm depth (PDD_{10}^{20}) for a field size of 10 x 10 cm² defined at the phantom surface and with SSD = 100 cm using PENELOPE code. The authors then calculated the TPR_{10}^{20} using a relation between these two quantities defined in the TRS-398 protocol [5].

Table 4-2: Radiation sources and Monte Carlo calculated TPR_{10}^{20} quality specifier for the 5 energy beams used in this study. Comparisons are made between our results (third column) and those obtained by other authors that used the same energy spectra. The values between parentheses represent the relative percentage difference with our values. Our results were obtained from the calculated $\%dd(10)_x$ presented in table 4-1 and using equation 3.1.

Beam	Nominal energy (MV)	TPR_{10}^{20}			
		This work	Muir and Rogers [55]	Wulff <i>et al.</i> [52]	Erazo and Lallena [58]
^{60}Co	-	$0.555 \pm 1.6\%$	0.569 (2.5%)	0.572 (3%)	0.571 (2.8%)
Varian Clinac	4	$0.640 \pm 1.2\%$	0.623 (2.7%)	0.621 (3%)	0.644 (0.6%)
	6	$0.668 \pm 1.0\%$	0.666 (0.4%)	0.662 (1%)	0.670 (0.2%)
	10	$0.743 \pm 0.7\%$	0.734 (1.2%)	0.736 (0.9%)	0.739 (0.5%)
Elekta SL25	25	$0.795 \pm 0.3\%$	0.791 (0.5%)	0.797 (0.3%)	0.791 (0.5%)

The comparison of the MC calculated values from Wulff *et al.* with our values shows maximum deviations of 3% for ^{60}Co and 4 MV beams. For the other energy beams deviations were less than equal 1%. We found a maximum deviation of 2.7% for the 4 MV beam when comparing with results from Muir and Rogers. A maximum

deviation of 2.8% is found for the ^{60}Co beam and less than 1% for the other energies when comparing our results to Erazo and Lallena ones.

It is worth to point out that equation 3.1 introduces maximum deviations of 0.007 in calculations of the TPR_{10}^{20} [113]. Differences to the values obtained by Wulff *et al* and Erazo and Lallena are also expected since those authors have used a different methodology than that one used here for calculating TPR_{10}^{20} values.

Despite differences presented for some photon beams, both quality specifiers, $\%dd(10)_x$ and TPR_{10}^{20} calculated in this study are in fair agreement with the values referred in the literature by authors who used the same spectrum to simulate a collimated point source.

4.1.2 Phase space file vs Beam simulations

Table 4-3 compares the absorbed energy values calculated at reference depths in water using the full spectrum beam and the phase-space file as radiation sources in PENELOPE. The absorbed energies calculated using the psf's show agreement with those ones calculated using the full spectrum beam within maximum statistical uncertainties of 0.5%. The maximum percentage relative difference was 0.3% for the 25 MV beam which is still less than the combined uncertainties of 0.4% for the absorbed energy values calculated using the two methodologies. For all energy beams investigated, the differences between the values obtained by the two methods were smaller than their respective total uncertainties.

Table 4-3 also shows a significant difference between the simulation time using the two methods. Simulation time for calculating absorbed dose to water using a

Table 4–3: Absorbed energies to water calculated in a disc with 1.0 cm radius and 0.025 cm thickness at and SSD = 100 using a full spectrum beam and a phase space file (psf) in PENELOPE input-files.

Beam	Absorbed energy (eV / histories)				
	Simulations with beam	Time (days)	Simulations with psf	Time (days)	Relative difference
^{60}Co	$17.976 \pm 0.5\%$	12.9	$17.997 \pm 0.5\%$	1.7	0.1%
4 MV	$21.783 \pm 0.5\%$	17	$21.822 \pm 0.5\%$	1.6	0.2%
6 MV	$24.269 \pm 0.5\%$	17	$24.218 \pm 0.5\%$	1.7	0.2%
10 MV	$37.265 \pm 0.4\%$	20.1	$37.175 \pm 0.4\%$	2.2	0.2%
25 MV	$59.184 \pm 0.3\%$	4.2	$59.371 \pm 0.3\%$	1.0	0.3%

psf as a source in PENELOPE is approximately 10 times shorter than using a full spectrum beam, except for the 25 MV beam where the time is only 4.2 times shorter.

Therefore the proposed methodology of using phase-space files instead of a full spectrum in the input-file of PENELOPE shows a significant efficiency. Based on this, the use of variance reduction techniques which in turn can increase time in simulations becomes more feasible when using a psf as a source instead of a full spectrum beam.

4.1.3 Restricted stopping power ratio

Figure 4–1 shows our calculated values for the Spencer-Attix water to air restricted stopping power ratio, $(\bar{L}_\Delta/\rho)_{air}^{water}$, with $\Delta = 10$ keV, as a function of the

TPR_{10}^{20} . For comparison, data from the TRS-398 dosimetry protocol [5] were also plotted using the cubic fit provided in that report. The fit data from Kalach and Rogers [113] for $TPR_{20,10} \geq 0.62$ is also shown in addition with a stopping-power value calculated for a ^{60}Co beam from Rogers and Yang [117].

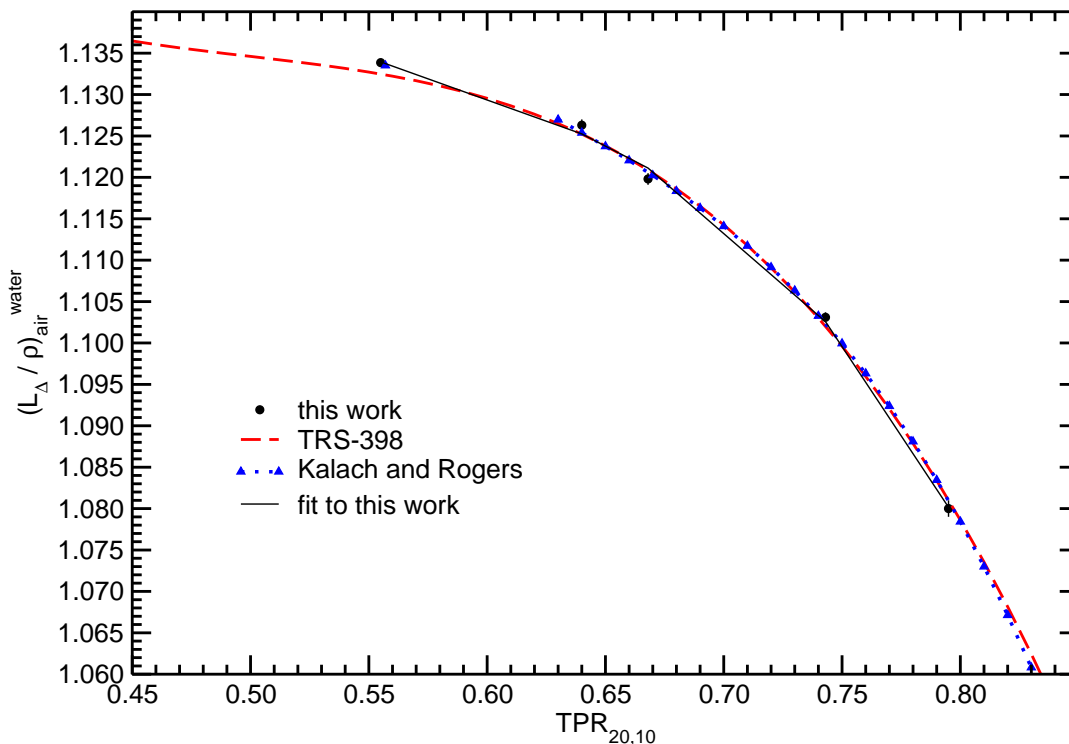


Figure 4-1: Spencer-Attix water to air stopping-power ratios calculated by Monte Carlo simulation. Our values calculated with PENELOPE (black circles) are shown together with a cubic fit (straight line) given by $(\bar{L}/\rho)_{air}^{water} = 1.7736 - 3.1476(TPR_{10}^{20}) + 5.2889(TPR_{10}^{20})^2 - 3.0527(TPR_{10}^{20})^3$ with rms deviation of 0.07%. Data from the fit provided in TRS-398 are shown in red dashed line. A fit from Rogers and Kalach for $TPR_{10}^{20} \geq 0.63$ plus the stopping power ratio for a ^{60}Co beam from Rogers and Yang is also shown (dotted line with blue triangles).

A cubic fit to our calculated data for providing $(\bar{L}_\Delta/\rho)_{air}^{water}$ values for $0.555 \leq \text{TPR}_{10}^{20} \leq 0.795$ is given by:

$$\left(\frac{\bar{L}_\Delta}{\rho}\right)_{air}^{water} = 1.7736 - 3.1476(\text{TPR}_{10}^{20}) + 5.2889(\text{TPR}_{10}^{20})^2 - 3.0527(\text{TPR}_{10}^{20})^3 \quad (4.1)$$

For values of TPR_{10}^{20} near to 0.557 this fit presents differences of 0.1% and 0.03% with the values of the TRS-398 and Rogers and Yang respectively. For a TPR_{10}^{20} of 0.8 these differences are both approximately 0.1%. The root mean square deviation of the data from the fit is around 0.07%.

Therefore, our calculated values for the water-to-air restricted stopping-power ratios are in excellent agreement with the values provided by the TRS-398 dosimetry protocol and also with the data published by Kalach and Rogers [113] with differences less than 0.1%. Equation 4.1 can then be used to calculate $(\bar{L}_\Delta/\rho)_{air}^{water}$ values for photon beams with $0.555 \leq \text{TPR}_{10}^{20} \leq 0.795$.

4.1.4 Perturbation and beam quality correction factors

The overall perturbation factor

Figure 4–2 shows the overall perturbation factor for the NE2571 ionization chamber calculated according to equation 3.3 and with the use of the calculated stopping power ratios presented in subsection 4.1.3. As defined in subsection 2.4.1, this factor brings together all the effects related to the constitutive elements of an ionization chamber. For comparison our results are plotted with those obtained by Wulff *et al* [52] and Erazo and Lallena [58] which did calculations for this factor using EGSnrc and PENELOPE codes respectively.

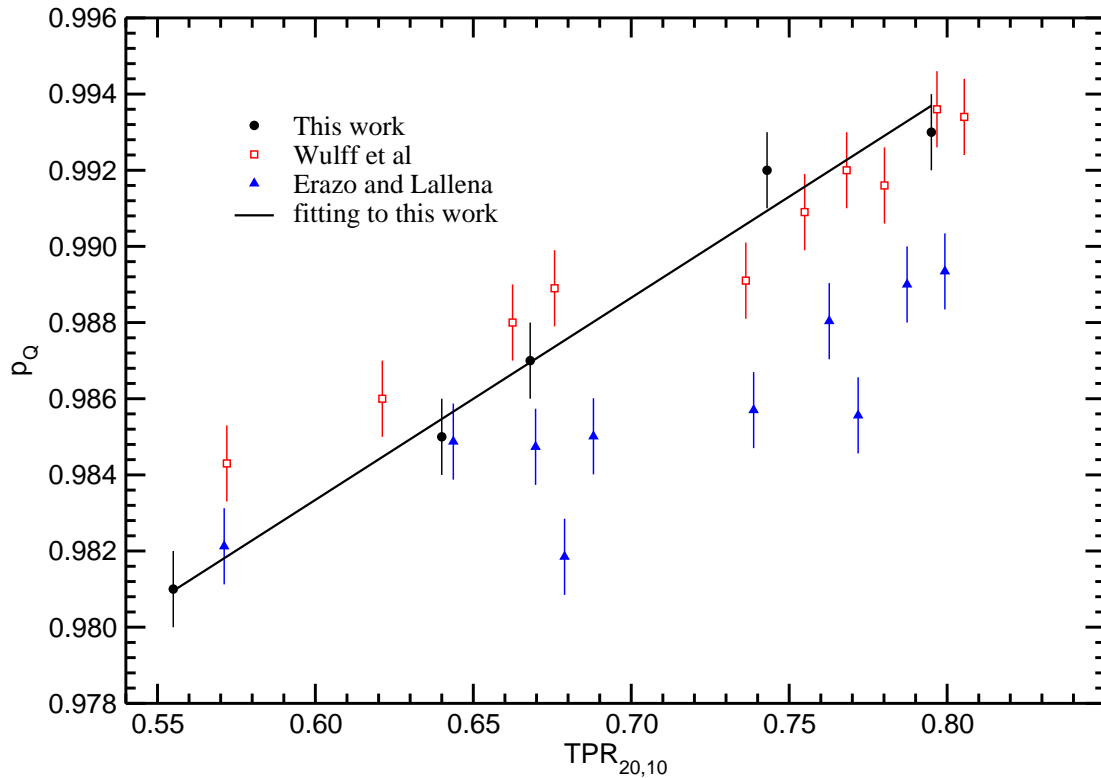


Figure 4–2: Monte Carlo calculated overall perturbation factor for the NE2571 ionization chamber as a function of the beam quality TPR_{10}^{20} . Our data (solid black circles) are shown in comparison with the results from Wulff *et al* (open red squares) and Erazo and Lallena (solid blue triangles). A fit of type $p_Q = a + b * TPR_{10}^{20}$ with $a = 0.952 \pm 0.003$, $b = 0.053 \pm 0.004$ and $r^2 = 0.98$ is given (black straight line) .

We can see from the plot that p_Q increases linearly with increasing the energy of the photon beam and it becomes closer to unity for higher energies. This means that the total perturbation effect of the chamber decreases with increasing energy. This proximity to unity for p_Q with increasing energy was expected considering that at higher energies the chamber approaches to the Bragg-Gray conditions of not disturbing the electron fluence, since in that case the range of the secondary particles

(electrons) can be larger than the cavity size of the chamber. Therefore the ratio D_w / D_{ch} approaches to the value of the water to air restricted stopping power ratio $(\bar{L}/\rho)_{air}^{water}$, and then p_Q approaches to one. The linearity of p_Q with TPR_{10}^{20} can also be understood considering that D_w and D_{ch} are both linear with the electron energy fluence. The same linear behaviour was also observed by Wulff *et al* and approximately by Erazo and Lallena. A linear fit to our data with $r^2 = 0.98$ was proposed and given by:

$$p_Q = 0.952 + 0.053 * TPR_{10}^{20} \quad (4.2)$$

Therefore, equation 4.2 can be used to easily determine p_Q for the NE2571 ionization chamber in photon beams with TPR_{10}^{20} in the range $0.555 \leq TPR_{10}^{20} \leq 0.795$. The root mean square deviation (rms) of the data from the fit is of 0.06%.

The replacement correction factor

Figure 4-3 shows the P_{repl} correction factor also calculated for the NE2571 ion chamber as a function of the TPR_{10}^{20} . The plot presents our data calculated by using equation 3.4 in comparison with results obtained by Wulff *et al*. Despite the uncertainties (0.2% in the worst case) the values of P_{repl} calculated in this study are in fair agreement with those obtained by Wulff *et al* considering the total combined uncertainties. For ^{60}Co beam our calculated value of 0.996 ± 0.001 for this factor was also much closer to that one obtained by Wulff *et al* of 0.995 ± 0.001 than the value provided by the TRS-398 of 0.987 ± 0.003 . Our result is also in fair agreement with the value of $0.9964 \pm 0.08\%$ obtained by Wang and Rogers [76].

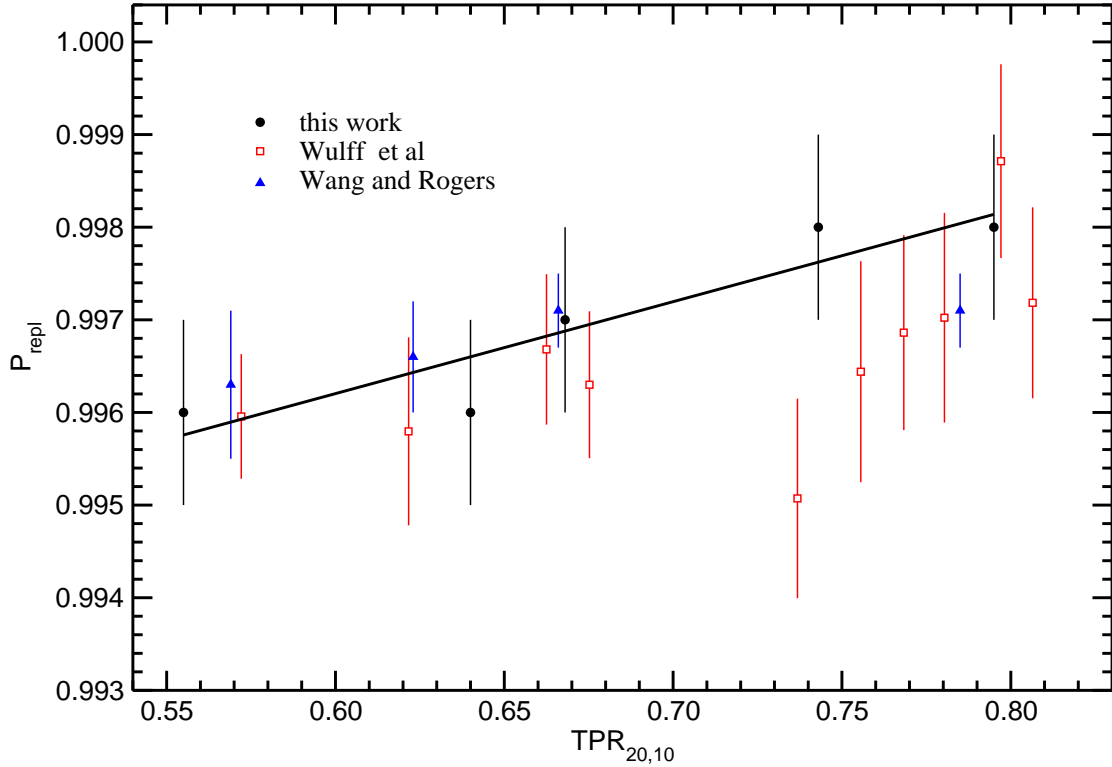


Figure 4–3: The P_{repl} correction factor which accounts for the combined effect of the dose gradient in the absence of the chamber (P_{grad}) and secondary electron fluence perturbation (P_{fl}). Our results (black solid circles) for the NE2571 ion chamber are shown in comparison with those ones obtained by Wulff *et al* (open red squares) and Wang and Rogers (blue triangles). A linear fit of type $P_{repl} = a + b * TPR_{10}^{20}$ with $a = 0.990 \pm 0.002$, $b = 0.010 \pm 0.002$ and $r^2 = 0.85$ is proposed to our data.

It is worth point out that P_{repl} values calculated in this study follow a theoretical definition proposed by Wulff *et al* [52] and also by Wang and Rogers [76] and illustrated in figure 3–1 and equations 3.3 to 3.6. Values of P_{repl} available in current dosimetry protocols are based on experimental results from Cunningham and Sontag [118] (TG-51) and Johansson *et al* [119] (TRS-398). According to Huq *et al* [120]

differences of up to 0.5% can be found for the replacement correction factors when different approaches are used. Wulff *et al* also points out that taking into account uncertainties on those experimental data, deviations from Monte Carlo calculations are not surprising although still deserve further investigations. In addition, Wang and Rogers [76] also investigated differences between Monte Carlo calculations for the P_{repl} correction factor and experimental data available in dosimetry protocols. According to these authors, the interpretation of the measured data as the replacement correction in dosimetry protocols is not correct.

A linear fit with $r^2 = 0.85$ to our data is presented and given by:

$$p_{repl} = 0.990 + 0.010 * TPR_{10}^{20} \quad (4.3)$$

Equation 4.3 can then be used for determining P_{repl} for the NE2571 ion chamber in the range of TPR_{10}^{20} presented in this study. The root mean square deviation of the data from the fit is of 0.03%.

The wall perturbation factor

Figure 4–4 presents our calculated values of P_{wall} for the NE2571 farmer chamber as a function of the beam quality. It is important to mention that although our results have been compared with those ones obtained by Wull *et al*, those authors calculated the perturbation of the graphite wall of the chamber plus the waterproofing sleeve ($P_{wall+sleeve}$) and the effect of the chamber stem P_{stem} in a separately way. On the other hand, what we call P_{wall} in this study is the combined effect of the perturbation caused by the graphite wall, the stem and the sleeve of the chamber ($P_{wall+sleeve+stem}$). In this sense, in order to make a comparison we took the product of $P_{wall+sleeve}$ and

P_{stem} calculated by the authors. The results for $P_{wall+sleeve}$ calculated by Buckley and Rogers [121] and Wulff *et al*, using the EGSnrc user codes CSnrc and egs_chamber respectively, are also shown in figure 4–4 for comparison.

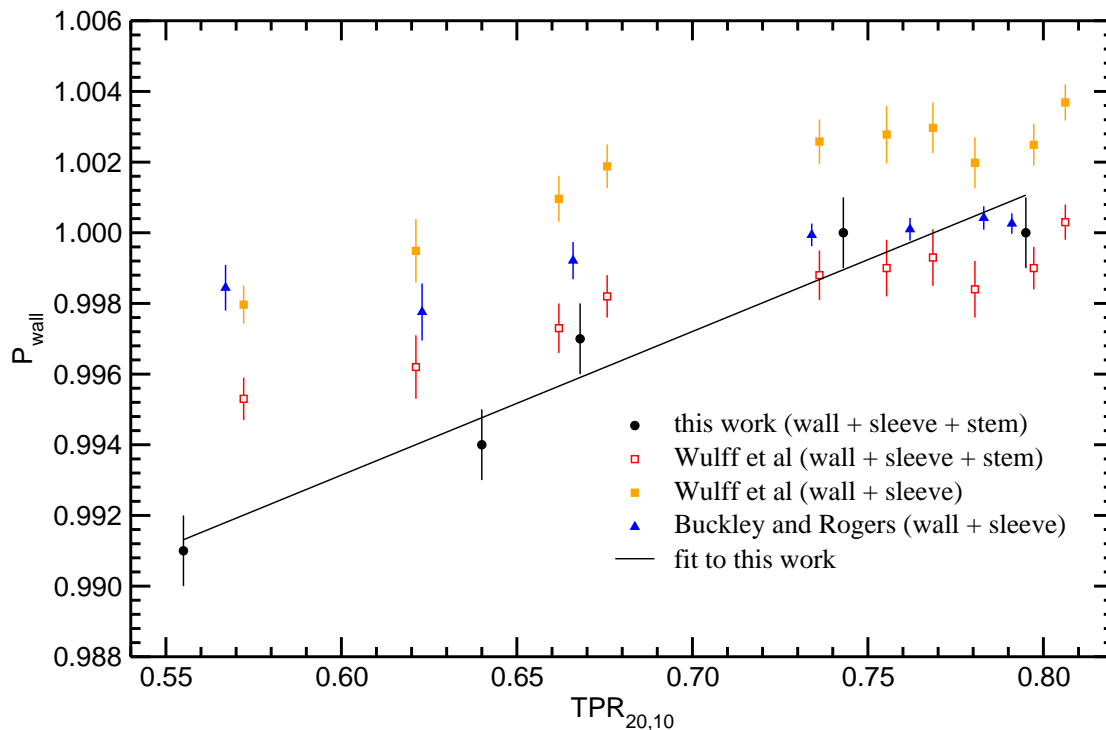


Figure 4–4: The wall perturbation factor for the NE2571 chamber. Our calculated values (solid black circles) for $P_{(wall+sleeve+stem)}$ are shown in comparison with the values for this same factor from Wulff *et al* (open red squares). The figure also shows the values of $P_{(wall+sleeve)}$ calculated by Wulff *et al* (solid orange squares) and Buckley and Rogers (solid blue triangles). A linear fit $P_{wall} = a + b(TPR_{10}^{20})$ with $a = 0.969 \pm 0.004$, $b = 0.041 \pm 0.006$ and $r^2 = 0.93$ is shown (black straight line) to our data.

As expected all curves predicts a decrease of the wall perturbation effect with increasing energy which results in increasing values of P_{wall} and closer to unity for higher energy beams. Despite the uncertainties (maximum of 0.2%) obtained for this correction factor, the values calculated for energy beams greater or equal to 6 MV ($TPR_{10}^{20} = 0.668$) are in fair agreement with those obtained by Wulff *et al* and Buckley and Rogers with maximum relative difference of 0.2%. On the other hand, the values calculated for ^{60}Co and 4 MV beams were slightly divergent to those obtained by the referred authors even if we take into account the effect of the chamber steam. For ^{60}Co ($TPR_{10}^{20} = 0.555$) differences were 0.68% and 0.74% compared to the values from Buckley and Rogers and Wulff *et al* respectively. This last one falls to 0.43% if we take into account the steam effect calculated separately by Wulff *et al*. For the 6 MV beam, our calculated value for $P_{(wall+sleeve+steam)}$ differs in 0.48% and 0.61% to the $P_{(wall+sleeve)}$ values calculated by Buckley and Rogers and Wulff *et al* respectively. In comparison to the $P_{(wall+sleeve+steam)} = P_{(wall+sleeve)} \times P_{(stem)}$ from Wulff *et al* the difference is around 0.28%.

Although our calculated value for P_{wall} in ^{60}Co beam ($0.991 \pm 0.2\%$) is close to those reported in current dosimetry protocols such as the TRS-398 ($0.992 \pm 0.5\%$) and TG-51, the Almond-Svensson formalism [5] used for calculating P_{wall} in those protocols are known to overestimate the wall perturbation factor [69, 75]. In this sense, a better investigation of these differences for lower energy beams is necessary.

The present results shows a variation in $P_{(wall+sleeve+steam)}$ of 0.9% for TPR_{10}^{20} values between 0.555 and 0.8. A linear fit to our data with $r^2 = 0.93$ is given by:

$$p_{wall} = 0.969 + 0.041(TPR_{10}^{20}) \quad (4.4)$$

Therefore equation 4.4 allows one to calculate P_{wall} value for the NE2571 ionization chamber in photon beams with $0.555 \leq TPR_{10}^{20} \leq 0.8$.

The central electrode perturbation factor, P_{cel}

Figure 4–5 shows our central electrode perturbation factor values in comparison with those obtained by Wulff *et al* and Buckley *et al* [108] for the NE2571 ion chamber. As we have already discussed, this factor accounts for the central electrode material (aluminium) being different from the cavity one (air). Our results suggest that P_{cel} varies from 0.993 to 0.995 when TPR_{10}^{20} goes from 0.555 to 0.80. The data are in good agreement, within uncertainties (maximum of 0.2%), with those calculated by Wulff *et al* with maximum difference of 0.14% for a TPR_{10}^{20} of 0.555 (^{60}Co beam). This is also in good agreement with the value of $0.993 \pm 0.2\%$ provided in the TRS-398 dosimetry protocol for this chamber in ^{60}Co beam. The maximum difference to Buckley *et al* values is of 0.08% for a TPR_{10}^{20} of 0.640 (4 MV beam). A linear fit with $r^2 = 0.83$ and given by:

$$p_{cel} = 0.989 + 0.007(TPR_{10}^{20}) \quad (4.5)$$

is proposed for calculating P_{cel} in the range of TPR_{10}^{20} investigated.

Figure 4–5 also shows that our uncertainties are too large when compared to those ones obtained by the referred authors. This can be understood since the methodology used to calculate P_{cel} according to equation 3.5 involves a ratio of

doses to the air cavity (few interactions) of the chamber and to a reduced air volume cavity due to the presence of the electrode (much less interactions). This means that more efficient variance reduction techniques must be used in order to get more precise values for this correction factor.

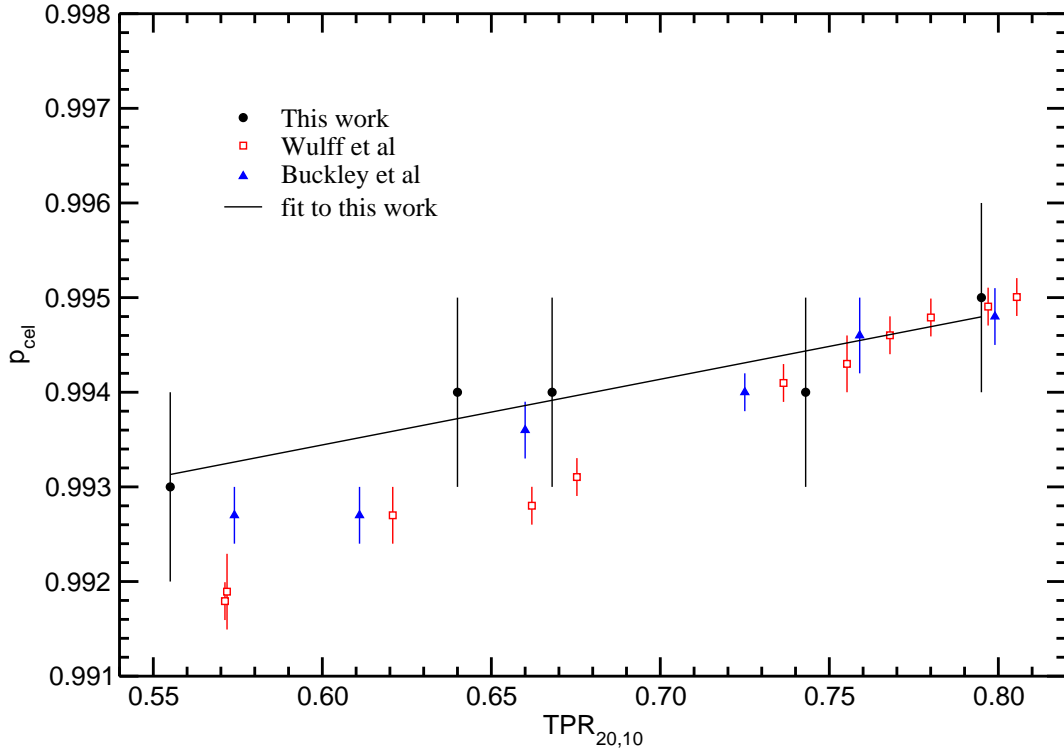


Figure 4-5: The central electrode correction factor, P_{cel} , for the NE2571 ionization chamber. Values calculated in this study (solid black circles) are shown in comparison with those ones obtained by Wulff *et al* (open red squares) for the same chamber. A liner fit $P_{cel} = a + b(TPR_{10}^{20})$ with $a = 0.989 \pm 0.01$, $b = 0.007 \pm 0.002$ and $r^2 = 0.83$ is proposed to our data.

The beam quality correction factor, k_Q

Figure 4-6 shows the beam quality correction factor, k_Q , for the NE2571 ionization chamber as a function of the TPR_{10}^{20} and calculated in this study by using equation 3.2.

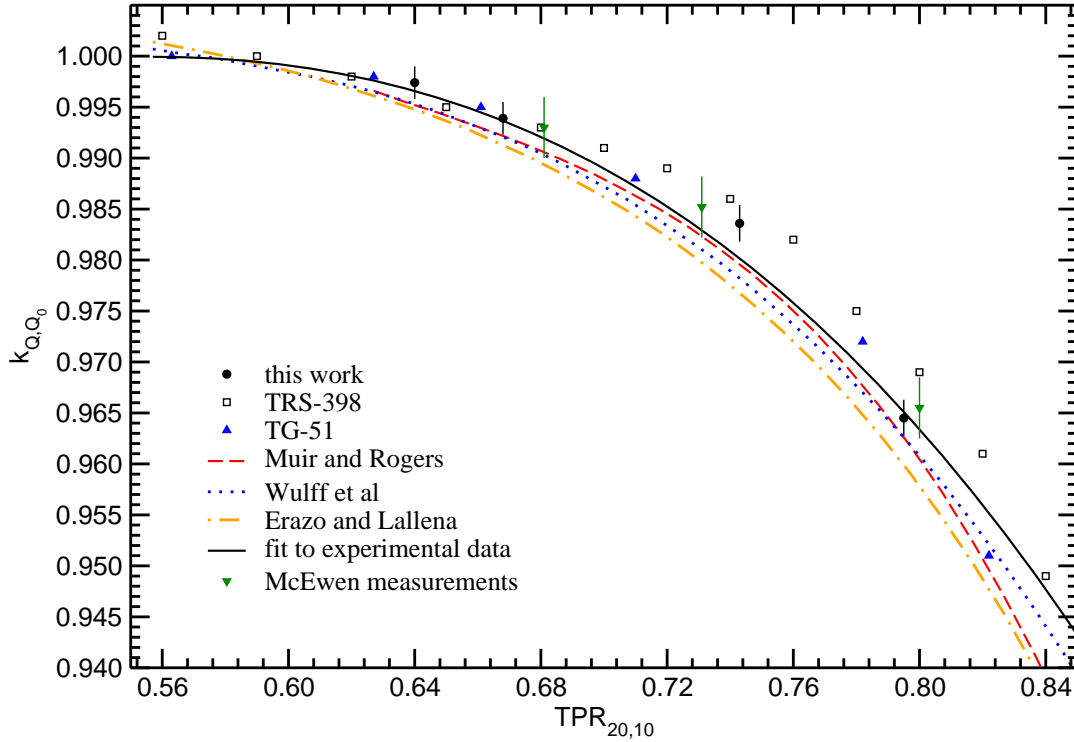


Figure 4-6: The beam quality correction factor for the NE2571 ionization chamber. Data points are from our results (solid black circles), TRS-398 (open squares) and TG-51 (blue triangle up). Fit to Monte Carlo calculated data are from Muir and Rogers (dashed red line), Wulff *et al* (dotted blue line) and Erazo and Lallena (point dashed orange line). A fit to experimental data compiled by Andreo and given by Wulff *et al* is also plotted (solid black line) for comparison with Monte Carlo results. Values measured by McEwen are also shown (green triangles down).

Data provided in current dosimetry protocols [5, 78] as well as results from the literature [52, 55, 58] are also plotted together for comparison. The first three sets of data points correspond to our results (solid black circles) and data from the dosimetry protocols TRS-398 [5] (open squares) and TG-51 [78] (blue triangle-up). Fitting curves provided by Muir and Rogers [55] (dashed red line), Wulff et al [52] (dotted blue line) and Erazzo and Lallena [58] (point-dashed orange line) are also plotted for the same TPR_{10}^{20} range. In addition, a cubic polynomial fit to experimental data compiled by Andreo [81] and provided by Wulff *et al* [52] is also plotted (solid black line) for comparison with our Monte Carlo calculated data. Comparison is also made to values measured by McEwen [122] (green triangles down) for this correction factor.

Our calculated values are in good agreement (within uncertainty of 0.2%) with those obtained by the referred authors, except for the k_Q value corresponding to a TPR_{10}^{20} of 0.743 (10 MV) where differences were up to 0.4% (Muir and Rogers), 0.5% (Wulff *et al*), 0.7% (Erazo and Lallena) and 0.3% (Experimental data). This result points out the necessity of calculating k_Q for a larger number of TPR_{10}^{20} values, especially in the range of 10 MV beams. Agreement was also satisfactory when comparing to data provided in dosimetry protocols with maximum percentage difference of 0.6% to the TRS-398 value for a TPR_{10}^{20} of 0.795 (25 MV). Differences to the values provided in TG-51 were 0.1% on average. Table 4–4 shows the differences between our Monte Carlo calculated results and those obtained with the fitting curves provided by the referred authors.

Table 4–4: Monte Carlo calculated k_Q factors for the NE2571 ion chamber and differences to results found in the literature. Fitting curves provides the values of k_Q for the same TPR_{10}^{20} used in this study. The uncertainties to our calculated values are shown in parentheses besides each value.

% Differences to k_Q values calculated in this study							
TPR_{10}^{20}	k_Q , this work	TRS-398	TG-51	Muir and Rogers	Wulff <i>et al</i>	Erazo and Lallena	Experimental data
0.640	0.9974(0.2%)	0.04%	0.1%	0.2%	0.2%	0.3%	0.1%
0.668	0.9939(0.2%)	0.1%	0.1%	0.2%	0.2%	0.3%	0.02%
0.743	0.9836(0.2%)	0.1%	0.1%	0.4%	0.5%	0.7%	0.3%
0.795	0.9645(0.2%)	0.6%	0.1%	0.2%	0.2%	0.5%	0.1%

Cubic polynomial fits to data from TRS-398 and TG-51 were calculated in order to compare to our results for the same TPR_{10}^{20} values used in this study. A cubic polynomial of type:

$$k_Q = a + b(TPR_{10}^{20}) + c(TPR_{10}^{20})^2 + d(TPR_{10}^{20})^3 \quad (4.6)$$

was also fitted to our data with a $\chi^2/df = 1.3$ for $0.637 \leq TPR_{10}^{20} \leq 0.797$. The fit parameters are shown on table 4–5.

Figure 4–7 provides a very enlightening plot, as suggested by Rogers [123], for understanding the dependence of the beam quality correction factor, k_Q with its respective components, such as the water to air restricted stopping power ratio and

Table 4–5: Fit parameters to a cubic polynomial of type $k_Q = a + b (TPR_{10}^{20}) + c (TPR_{10}^{20})^2 + d (TPR_{10}^{20})^3$ for calculating k_Q values as a function of the TPR_{10}^{20} .

	Parameters			
	a	b	c	d
Fit to this work	4.4918	-15.236	22.257	-10.91
Fit to TRS-398 data	1.6424	-3.1183	5.1047	-2.8251
Fit to TG-51 data	1.8835	-4.2748	6.9468	-3.8034

the chamber perturbation factors, as defined in equation 2.20. All those components are taken as the ratio between their values in the quality beam, Q , and the reference quality, Q_0 (^{60}Co).

We can see from this plot that the main component in k_{Q,Q_0} is the the water to air restricted stopping power ratio $(\bar{L}_\Delta/\rho)_{air}^{water}$, responding for a variation of approximately 4.8% in the beam quality correction factor for TPR_{10}^{20} between 0.555 (^{60}Co) and 0.795 (25 MV). For the same energy range the combined effect of all chamber perturbation factors (P_Q) responds for a variation of 1.2% in k_{Q,Q_0} . Furthermore, figure 4–7 also shows that P_{wall} , with a variation of 0.9% in the TPR_{10}^{20} range investigated, is the most important chamber perturbation factor and it is responsible for 75% of the 1.2% variation in P_Q mentioned above. The replacement (P_{repl}) and central electrode (P_{cel}) perturbation factors are almost equal to unity for the energy beam range investigated, both showing a variation of around 0.2%.

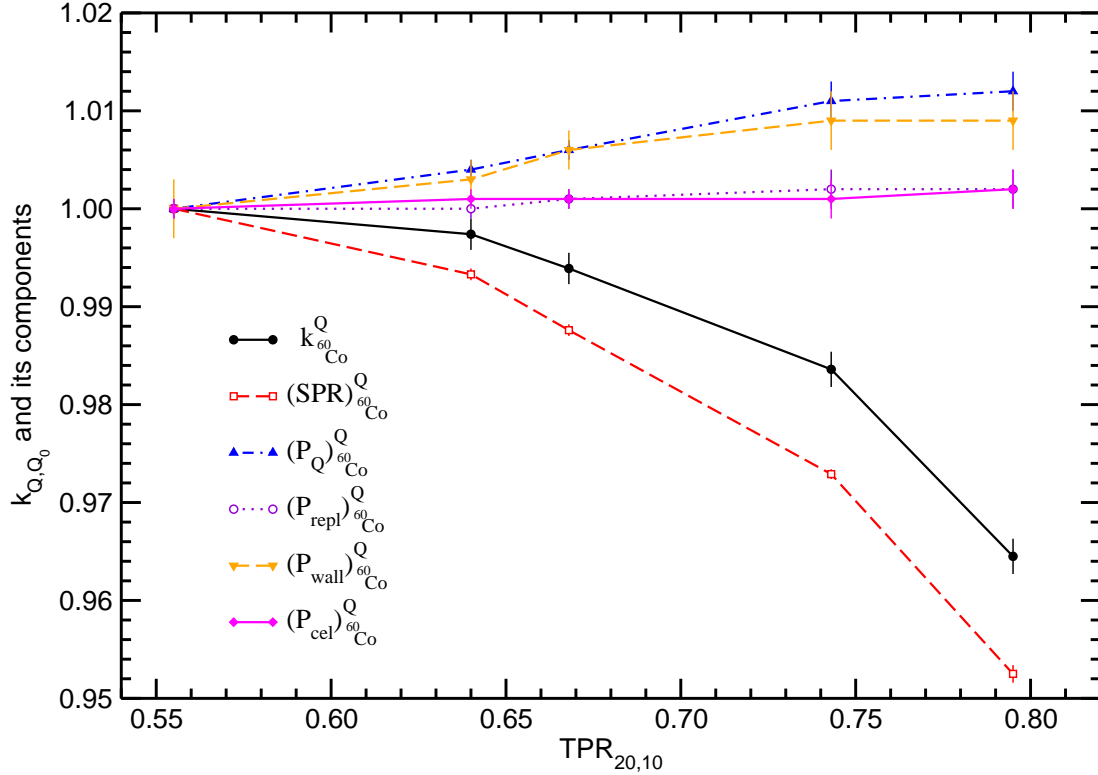


Figure 4-7: Beam quality correction factor, k_Q , and its components for the NE2571 ionization chamber as a function of the TPR_{10}^{20} . The components are given by the ratio in two beam qualities of the water to air restricted stopping power ratio $(SPR)_{60Co}^Q$ and the overall perturbation factor $(P_Q)_{60Co}^Q$, as well as the factors, $(P_{wall})_{60Co}^Q$, $(P_{repl})_{60Co}^Q$, and $(P_{cel})_{60Co}^Q$ assumed to be independent of each other.

The beam quality correction factor, defined as the ratio, in two beam qualities, of the products of all its components, is then responsible for a variation of approximately 3.6% on the NE2571 ion chamber response with the TPR_{10}^{20} .

Therefore, the results presented so far shows that our calculations for the beam quality and perturbation correction factors for the NE2571 ionization chamber are in fair agreement with several data from the literature. Discrepancies found for the wall

perturbation factor in low energies highlight for a better investigation on calculating this factor. In addition, deviations in single perturbation factors also support the directly calculation of the beam quality correction factor or a unique chamber- and quality-dependent factor as proposed by Sempau *et al* [83].

4.2 Buildup and surface dose calculations with EGSnrc system

In this section results obtained with the Monte Carlo code system EGSnrc for parallel plate chambers at the surface and in the build-up region of photon beams will be presented and discussed.

4.2.1 Surface depth dose curves

Figure 4–8 shows percentage depth dose curves at superficial layers ($0.5 \mu\text{m} \leq z \leq 0.1 \text{ mm}$) of a water phantom as a function of depth for the four energy beams investigated with a $10 \times 10 \text{ cm}^2$ field. Depth doses are normalized to dose maximum in the absence of electron contamination.

We can see from this plot that there is a significant dose gradient for the of range of depths investigated which supports the previous discussion about what surface dose means. For ^{60}Co beam, the total percentage depth dose varies by approximately 9% from $z = 0.5 \mu\text{m}$ to 0.1 mm. In this same depth range, the variations obtained for 6, 10 and 25 x-ray beams are around 6%, 3.4% and 2% respectively. We can also see that surface doses (and also the gradient) decrease with increasing the energy of the beam. This can be understood taking into account the generation of high-energy electrons that will deposit their energies at larger depths [31].

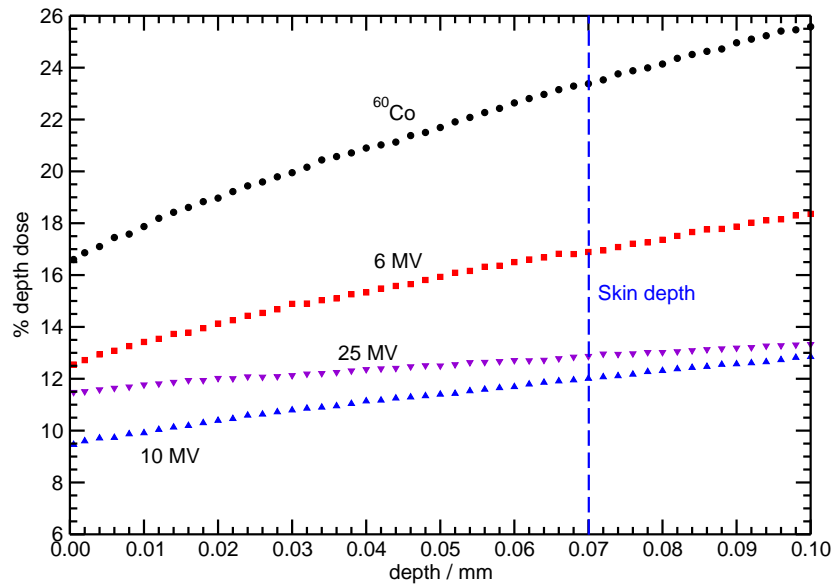


Figure 4–8: Surface percentage depth dose curves for high energy photon beams as a function of depths between $0.5 \mu\text{m}$ and 0.1 mm in a cylindrical water phantom with 15 cm radius and about 30 cm height. For all energy beams a field of $10 \times 10 \text{ cm}^2$ is defined at an $\text{SSD} = 100 \text{ cm}$. Surface and skin depths are considered to be at $z = 0.5 \mu\text{m}$ and $z = 0.07 \text{ mm}$ respectively. Values are normalized by the maximum dose without electron contamination.

However, figure 4–8 shows that surface dose values for the 25 MV curve are larger than the 10 MV ones in the depth range of $0.5 \mu\text{m} \leq z \leq 0.1 \text{ mm}$. A reasonable explanation for this behaviour can be a larger contribution of contaminant electrons and low energy photons produced in the head of the accelerator as well as in the air below it. In this sense 25 MV beams produce a larger amount of contaminant electrons and lower energy photons than beams with lower nominal energy, which in turn contributes to increase the surface dose.

This explanation is also supported by the results shown in figure 4–9 for the photon component of the same surface depth dose curves.

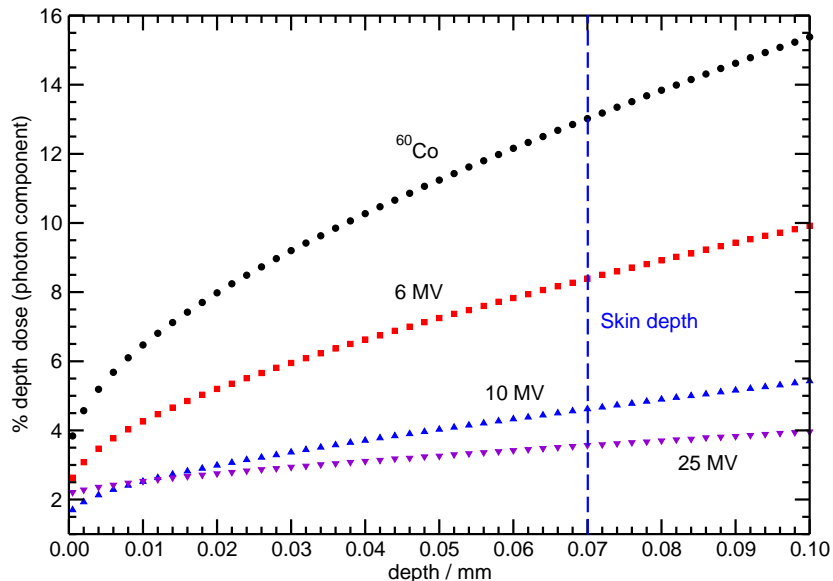


Figure 4–9: Photon component of the surface percentage depth dose curves shown in figure 4–8. Electron contamination is removed by choosing only photon particles from the beams produced in BEAMnrc simulations and also making ECUT = 30 MeV for the air between the head accelerator and the water phantom in DOSRZnrc. Values are normalized by the maximum photon component dose (without electron contamination).

When electron contamination is removed, the depth range in which the surface doses for the 25 MV beam are larger than the 10 MV ones is significantly reduced to $0.5 \mu\text{m} \leq z \leq 0.01 \text{ mm}$.

Table 4–6 shows the contribution to the total dose from photons and contaminant electrons at the shallowest depth $z = 0.5 \mu\text{m}$ and the skin depth $z = 0.07 \text{ mm}$.

Table 4–6: Surface ($z = 0.5 \mu\text{m}$) and skin depth ($z = 0.07 \text{ mm}$) percentage depth doses for high energy photon beams with and without contaminant electrons. Values are normalized by the maximum dose without contaminant electrons. Statistical uncertainties in brackets are in the last digits.

Photon beams	% depth doses					
	$z = 0.5 \mu\text{m}$			$z = 0.07 \text{ mm}$		
	Total	photons	contaminant electrons	Total	photons	contaminant electrons
^{60}Co	16.60 (9)	3.838 (2)	12.76 (9)	23.38 (7)	13.017 (4)	10.36 (7)
6MV	12.55 (6)	2.627 (5)	9.92 (6)	16.89 (5)	8.389 (1)	8.50 (5)
10 MV	9.46 (5)	1.699(2)	7.76 (5)	12.01 (5)	4.618 (5)	7.39 (5)
25 MV	11.48 (3)	2.210 (2)	9.27 (3)	12.87 (3)	3.568 (5)	9.30 (3)

For both depths we can see that the contaminant electron components for 25 MV beam are larger than the 10 MV ones. However, although at $z = 0.07$ mm the photon component for 25 MV is smaller than the 10 MV one, at $z = 0.5$ μm the photon component for 25 MV is still larger than the 10 MV one. This also supports the fact that more low energy photons are produced by the 25 MV beam and contribute for the surface doses being larger when compared to 10 MV ones for depths $z \leq 0.01$ mm.

The comparison between the total and photon component of the surface percentage depth dose curves also points out that contaminant electrons have a non negligible contribution to surface doses for high energy photon beams with a 10×10 cm^2 field at an SSD = 100 cm. In ^{60}Co beam, contaminants electrons are responsible for around 77% of the total surface dose calculated at $z = 0.5$ μm and around 44% at skin depth ($z = 0.07$ mm).

The results presented in this subsection shows that the term surface dose must be accurately addressed to a specific depth due to the high gradient of absorbed dose within the first millimetres at the surface of a water phantom.

4.2.2 Extrapolation chamber responses

The response of the ExCh 1 extrapolation chamber in ^{60}Co and 6 MV x-rays beams as a function of the electrodes separation (s) are shown in figure 4–10 with the point of measurement of the chamber at depth $z = 0.01$ mm in a polystyrene phantom. Experimental results [1] correspond to the mean ionization per unit mass (C kg^{-1}) normalized to the value at the depth of dose maximum for $s = 1$ mm. Our calculated results represent the dose to air cavity of the chamber also normalized by the dose at the depth of maximum dose for the same plate separation ($\%D_{gas}$).

Our Monte Carlo calculated values for the normalized chamber response are compared to experimental data obtained by Nilson and Montelius for the referred chamber, as well as to our calculated values for the dose to polystyrene phantom for the two energy beams and also normalized for D_{max} ($\%D_{med}$).

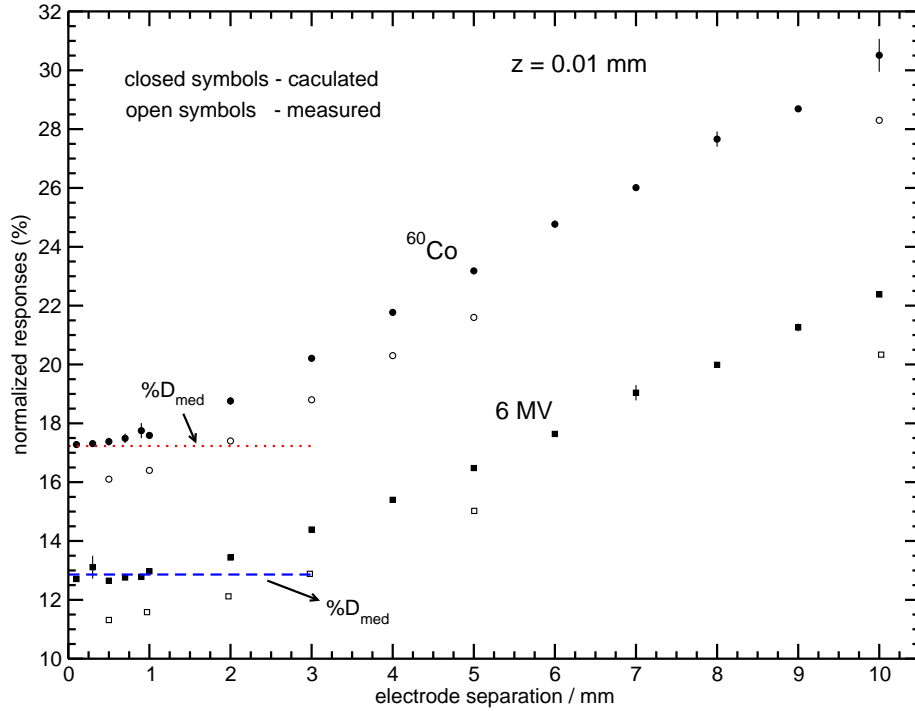


Figure 4-10: Simulated (closed symbols) and measured (open symbols) response for the ExCh 1 extrapolation chamber at $z = 0.01$ mm in polystyrene phantom for ^{60}Co (circles) and 6 MV (squares) beam as a function of the electrode separations. Results are normalized to D_{max} obtained with $s = 1$ mm. Values of calculated $\%D_{med}$ at $z = 0.01$ mm are also shown (dotted and dashed lines) for comparison.

The plots show that the normalized doses increase linearly with increasing plate separations. This can be understood by considering the electronic fluence perturbation caused by electrons from the side walls of the chamber. The most part of those electrons does not reach the collecting volume at small plate separations as they are primarily forward directed. However, when the distance between the electrodes increases, they will give a successively larger contribution to the response of the chamber. The non-linearity of the curve at small plate separations, where the slope decreases with decreasing the electrode distance can also be understood by considering the influence of the side wall electrons.

We can see from figure 4–10 that the calculated extrapolation curves become linear for plate separations larger than 2 mm for both ^{60}Co and 6 MV beams which is in agreement with the experimental results. The maximum difference between the experimental and calculated chamber response are around 2% at 10 mm plate separation for both energy beams investigated.

Nilson and Montelius obtained an extrapolated value for the normalized mean ionization at the surface ($z = 0.01$ mm) of the phantom of 16%, which they considered in fair agreement with the value of 18% obtained with a fixed parallel plate chamber in ^{60}Co beam. Our calculated values of $17.3\% \pm 0.1\%$ and $12.7\% \pm 0.1\%$ for $\%D_{gas}$ with $s = 0.1$ mm (considered to be our extrapolated readings) in ^{60}Co and 6 MV beams respectively, are also in good agreement with the calculated $\%D_{med}$ values of $17.2\% \pm 0.2\%$ and $12.9\% \pm 0.2\%$ at the corresponding depth ($z = 0.01$ mm) in the polystyrene phantom. Our results also have shown that a maximum plate separation of 1 mm is enough for obtaining an accurate $\%D_{gas}$ at the surface of the phantom.

Analysis of the perturbation factor, P_{repl} , can also help to understand the linear increasing of the $\%D_{gas}$ with increasing electrode separation. Figure 4–11 shows how P_{repl} varies with depth in polystyrene phantom in the buildup region of ^{60}Co and 6 MV beams for the smallest ($s = 0.1$ mm) and largest ($s = 10$ mm) plate separations used in the simulation of the ExCh 1 chamber response.

Figure 4–11 shows that the larger correction on chamber response due to fluence perturbation are obtained for the largest distance between the electrodes and closer to the surface due the contribution of contaminant electrons.

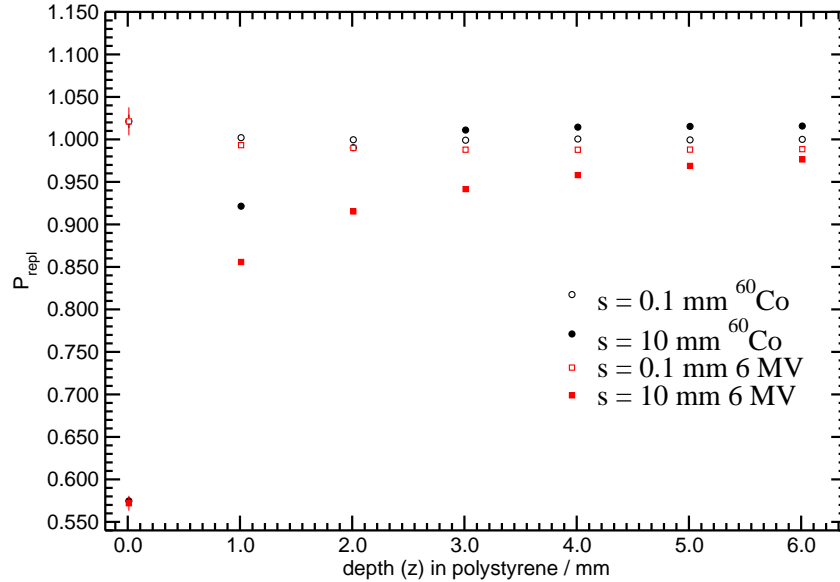


Figure 4–11: Monte Carlo calculated values of the replacement perturbation factors, P_{repl} , for the ExCh 1 extrapolation chamber in ^{60}Co (circles) and 6 MV (squares) beams as a function of depth z in the buildup region of a polystyrene phantom. Calculations were done for 2 different electrode separations, $s = 0.1$ mm (open symbols) and $s = 10$ mm (closed symbols).

This also supports the increase of $\%D_{gas}$ at $z = 0.01$ mm as shown in figure 4–10. We can also see from figure 4–11 that the replacement perturbation factor is approximately depth independent and close to unity for very small (0.1 mm) plate separations in both energy beams.

Figure 4–12 shows the difference between the percentage depth ionizations (PDI's) of a fixed parallel plate Markus chamber and the ExCh 2 extrapolation chamber as a function of depth normalized to depth of maximum dose (z/z_{max}) in polystyrene phantom for ^{60}Co and 25 MV beams with a $10 \times 10 \text{ cm}^2$ field at an SSD = 100 cm. The ExCh 2 extrapolation chamber was used by Gerbi and Khan for assessing accurate measurements of doses at the surface and in the build-up region of high energy photon beams. In this sense the plots shown in figure 4–12 represent the over-response of the Markus chamber when compared to the extrapolated values measured with the ExCh 2 chamber. In our Monte Carlo calculated data, the responses of the ExCh 2 chamber with $s = 0.1$ mm were considered to be the extrapolated ones (PDI for zero volume). Figure 4–12 shows that our calculated values agree within uncertainties with the experimental ones obtained by Gerbi and Khan. A root mean square deviation of about 1% is reported by the authors for the experimental results. Our calculated values presented a statistical uncertainty of 0.4% on average.

We can also see from both calculated and experimental results that the over-response of fixed parallel plate chambers decrease with increasing the energy of photon beams as it could be expected since the electrons are more forward directed for higher nominal energies. Calculated results show an over-response for the Markus

chamber at $z/z_{max} = 0.01$ of around $16.2\% \pm 0.4\%$ for the ^{60}Co beam which decreases to approximately $2\% \pm 0.2\%$ for 25 MV beam at the same depth.

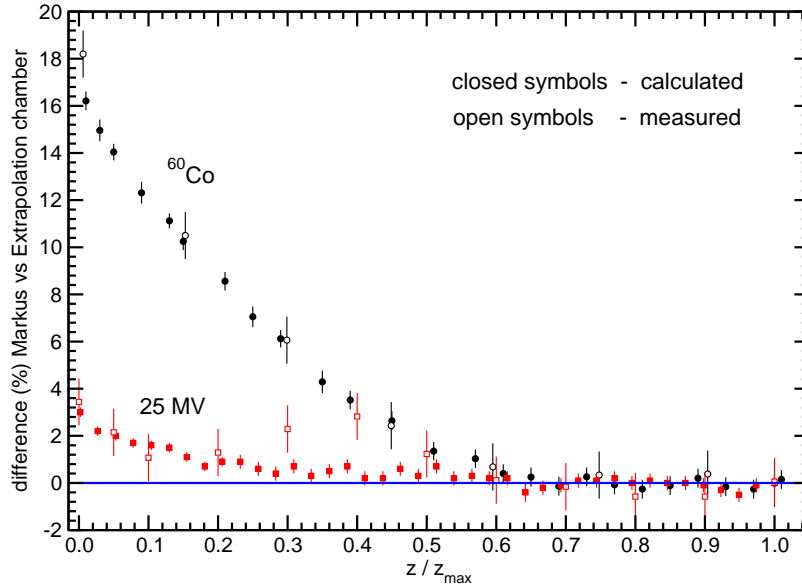


Figure 4-12: Difference between the percentage depth ionizations (PDI's) obtained with extrapolation chamber ExCh 2 and a fixed parallel plate Markus chamber in the buildup region in solid water for ^{60}Co (circles) and 25 MV (squares) beams. The over-responses of the Markus chamber are shown as a function of depth z normalized to the depth of maximum dose (z_{max}) for a $10 \times 10 \text{ cm}^2$ field at an $\text{SSD} = 100 \text{ cm}$. Experimental data (open symbols) are from Gerbi and Khan with root-mean-square deviation of about 1%. Monte Carlo calculated data (solid symbol) with egs_chamber were simulated by considering responses of the ExCh 2 chamber with $s = 0.1 \text{ mm}$ as the extrapolated values against the response of the Markus chamber. The blue base line represents null difference (no over-response).

It can also be seen from our calculated results that the greatest over response of the Markus chamber are within the first 50% of z_{max} . This is also in good agreement with the experimental results when comparing extrapolation chamber response against fixed parallel plate chambers in the build-up region of photon beams.

The maximum difference between calculated and experimental values was 0.75% for the ^{60}Co beam. For the 25 MV beam differences were also within uncertainties except for $z/z_{max} = 0.3$ and 0.4 where differences were 1.52% and 2.39% respectively. However those two experimental values are also far from the expected behaviour of the curve.

Figure 4–13 shows calculated and experimental results for the over-response of the Markus chamber as shown in figure 4–12 but for 6 MV (4–13(a)) and 10 MV (4–13(b)) beams. For these energy beams we have made a comparison with the experimental results obtained by Mellenberg [29], which also evaluated the over-response of a Markus chamber using an extrapolation chamber identical to the ExCh 2.

For the 6 MV beam our calculated data presented maximum differences of 2.3% when compared to experimental data from Gerbi and Khan at $z/z_{max} = 0.2$, and 2.4% in comparison to Mellenberg data at $z/z_{max} = 0.135$. For 10 MV maximum differences were of around 3.2% at $z/z_{max} = 0.05$ and 2.2% at $z/z_{max} = 0.08$ to experimental data obtained by Gerbi and Khan and Mellenberg respectively. Despite those differences to our calculated data, it is important to note that differences between the experimental data are even larger at the corresponding depths. We can see from figure 4–13 that the over-response of Markus chamber also decreases with increasing depth in phantom, similarly to what it is observed for ^{60}Co and 25 MV

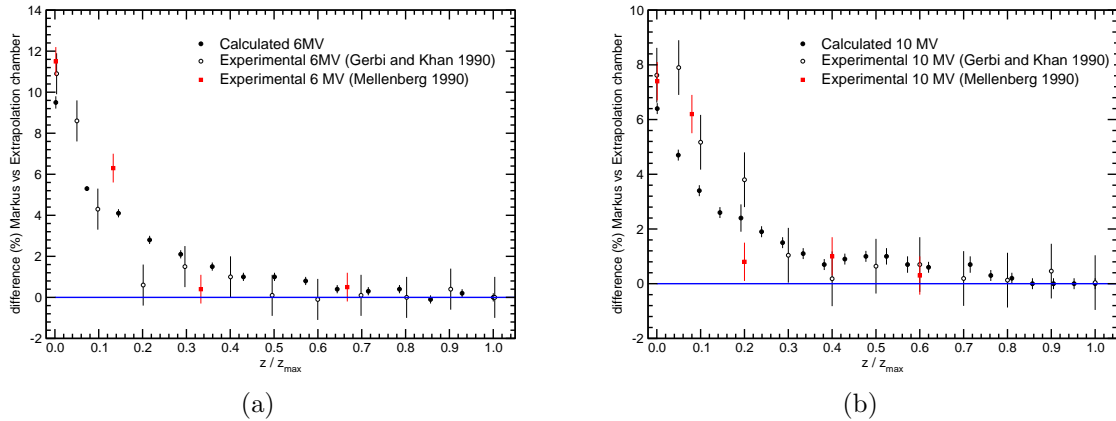


Figure 4–13: Markus chamber over-response for 6 MV (a) and 10 MV (b) beams when compared to the extrapolated values obtained with the ExCh 2. Monte Carlo calculated data (black solid circles) are compared to experimental data obtained by Gerbi and Khan and Mellenberg. In this study extrapolated data were calculated with $s = 0.1$ mm for the ExCh 2. The blue base line represents no over-response.

beams. Since any parallel plate chamber is not expected to over-respond for depths $z \geq z_{max}$, extrapolation chamber responses as a function of electrode separation must be constant for depths beyond z_{max} . In order to evaluate this behaviour, figure 4–14 shows the response of the extrapolation chambers ($\%D_{gas}$) investigated in this study (ExCh 1 and ExCh 2) as a function of the plate separations at the depth $z = 0.5$ cm for a ^{60}Co beam in polystyrene phantom.

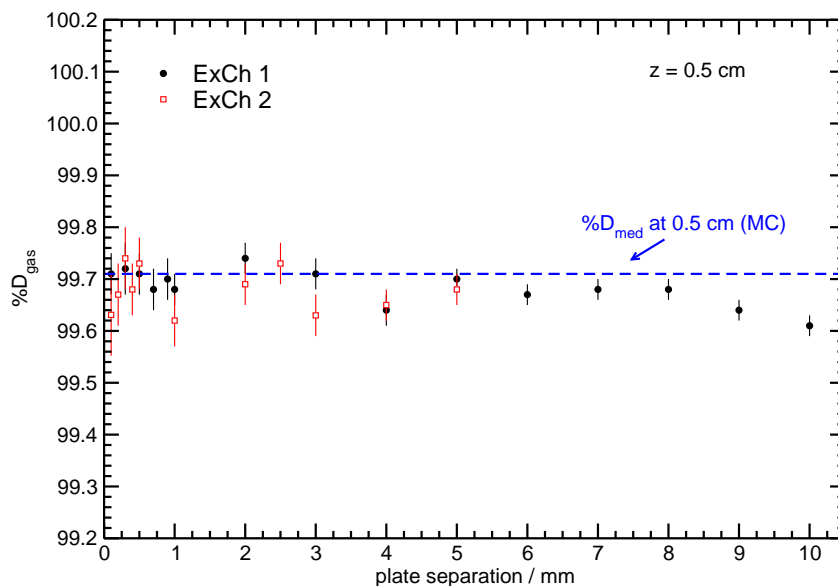


Figure 4-14: Extrapolation chambers responses ($\%D_{gas}$) as a function of the electrode separations with the EPOM at $z = 0.5$ cm depth in polystyrene phantom in a ^{60}Co beam. For each plate separation, s , the responses of the chambers are normalized to their maximum reading at $z = 0.4$ cm. The dashed blue line corresponds to the calculated percentage dose ($\%D_{med}$) value of $99.71\% \pm 0.02\%$ at the corresponding depth in polystyrene.

For each electrode separation, s , the dose to the air cavity of the chamber (D_{gas}) was normalized by its corresponding value at the depth of maximum dose. The ^{60}Co photon beam was chosen for being the lower photon beam energy and where parallel plate chambers present the greatest over-response in the build-up region as we have already shown in the previous results.

We can see from figure 4-14 that even for ^{60}Co beam, the response of the extrapolation chambers are actually independent of the electrode separation for the depth $z = 0.5$ cm and it is quite flat with maximum variations of 0.2%. Weighted

mean values over the different plate separations response provided $99.67\% \pm 0.01\%$ for the ExCh1 and $99.68\% \pm 0.01\%$ for the ExCh 2. The value of the percentage dose ($\%D_{med}$) in polystyrene at $z = 0.5$ cm of $99.71\% \pm 0.02\%$ is also shown (blue dashed line) for comparisons with the $\%D_{gas}$ at the corresponding depth. Maximum differences between $\%D_{med}$ and $\%D_{gas}$ were of 0.1% with $s = 10$ mm for the ExCh 1 and 0.09% with $s = 1$ mm for the ExCh 2.

Figure 4–15 shows percentage depth dose (PDD) curves obtained from extrapolated percentage depth ionizations (PDI's) in plastic phantoms in 6 MV (4–15(a)) and 10 MV (4–15(b)) photon beams. Data are from the literature for experimental measurements in plastic phantoms and also from our calculated $\%D_{gas}(z)$ for the extrapolation chambers with $s = 0.1$ using `egs_chamber` user code. Percentage depth doses (PDD's) in polystyrene were also calculated for the two mega-voltage beams for comparison with PDD's obtained from PDI's.

Experimental values from Butson et al [115] correspond to extrapolated measurements made with a radiochromic film with an effective point of measurement of 0.175 mm water equivalent thickness at the surface of a solid water phantom. The PDD curve presented by Pena et al [64] was obtained from PDI's measurements in water with a PTW 30001 cylindrical ionization chamber multiplied by a depth-dependent $D_{water}/D_{chamber}$ Monte Carlo conversion factor. All the other experimental PDD curves were built from extrapolated PDI's measurements with extrapolation chambers in solid water [1, 2, 29, 30, 64].

The results for the 6 MV beam in figure 4–15(a) shows that experimental data obtained by different authors are in fair agreement with our extrapolated

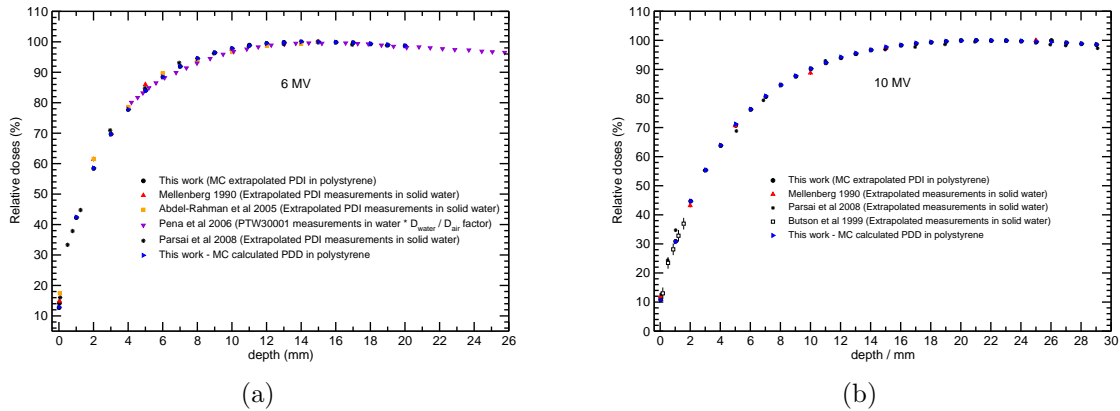


Figure 4–15: Percentage depth dose PDD curves for 6 MV (a) and 10 MV (b) photon beams. Data from Pena *et al* correspond to PDI’s measurements obtained with a PTW30001 ion chamber and multiplied by a Monte Carlo depth dependent conversion factor (D_w/D_{ch}). Extrapolated measurements in solid water with a radiochromic film was used by Butson *et al*. All the other experimental data as well as our calculated results (black circles) are from extrapolated PDI’s with extrapolation chambers. Monte Carlo calculated PDD’s are also plotted (blue triangle right) for comparison.

($s = 0.1$ mm) $\%D_{gas}(z)$ values calculated with the ExCh 1 extrapolation chamber. Comparison of our extrapolated $\%D_{gas}(z)$ calculations with the experimental data from Abdel-Rahman *et al* and Mellenberg *et al* shows a maximum difference of around 3.2% of D_{max} at $z = 2$ mm depth. Maximum differences of about 1.5% at $z = 7.4$ mm and 1.9% at $z = 1.25$ mm were also found when comparing our data to Pena *et al* and Parsai *et al* respectively. We also have a good agreement when we compare our extrapolated $\%D_{gas}(z)$ calculations in polystyrene for the 6 MV beam with the calculated PDD in polystyrene with maximum difference of 0.2% of D_{max} which are within maximal statistical uncertainties of 0.2%.

Analysis for the 10 MV beam in figure 4–15(b) shows a maximum difference of 3.8% of D_{max} between our calculations for the extrapolated $\%D_{gas}(z)$ and the result

measured by Parsai *et al* at $z = 1.03$ mm in the plastic phantom. Comparison to experimental data from Mellenberg *et al* and Butson *et al* shows maximum differences of 1.3% at $z = 10$ mm and 1.7% at $z = 1.6$ mm respectively. The calculated PDD curve in polystyrene for the 10 MV beam also showed a fair agreement with our calculated $\%D_{gas}(z)$ curve in polystyrene with a maximum difference of 0.5% of D_{max} which is also smaller than the correspondent combined uncertainty of 0.7%.

Table 4–7 summarizes the comparison between our calculations and the experimental data obtained by Gerbi and Khan and Nilson and Montelius for accessing $\%D_{med}$ at the surface of polystyrene phantom using extrapolation chambers. The table also shows Monte Carlo calculated $\%D_{med}$ curves at depths in the phantom corresponding to the effective point of measurement of the chambers for comparison. As we have already pointed out in section 1.3 the term surface dose as used by previous authors refers to the dose at the inside chamber front’s window (EPOM).

The experimental and calculated data shown in table 4–7 represent in this sense $\%$ dose values at depths corresponding to the respective water equivalent windows thickness of the chamber which are $z = 0.01$ mm and $z = 0.03$ mm for the ExCh 1 and ExCh 2 respectively. Comparison of calculated and experimental normalized responses shows a maximum difference of 3% for the ExCh 2 extrapolation chamber in 25 MV beam. However it is important to mention that the experimental data were obtained by Gerbi and Khan in a 24 MV Varian 2500 accelerator while our calculated results are for a 25 MV Elekta SL25. The smallest difference of 0.1% was found for the 10 MV beam also using the ExCh 2 extrapolation chamber. The last column of table 4–7 shows the calculated $\%D_{med}$ at the corresponding depths

Table 4–7: Surface ($z = \text{EPOM}$) relative doses in polystyrene phantom for a $10 \times 10 \text{ cm}^2$ field in ^{60}Co , 6 MV, 10 MV and 25 MV beams. The first column shows the experimental values considered to be extrapolated by Nilson and Montelius [1] ($z = 0.01 \text{ mm}$) and Gerbi and Khan [2] ($z = 0.03 \text{ mm}$). The values calculated with the `egs_chamber` user code (second column) for the respective chambers in polystyrene using 0.1 mm plate separation were considered as the extrapolated values for the respective chambers. The percentage dose to the medium ($\%D_{med}$) values were also calculated with the same MC code and are shown in the last column at the corresponding depths (front window) of the chambers for comparison.

	Experimental % ionization	Calculated % D_{gas}	Calculated % D_{med}
^{60}Co			
ExCh 1	16.1	17.2 ± 0.1	17.1 ± 0.1
ExCh 2	21.2	19.2 ± 0.1	19.20 ± 0.02
6 MV			
ExCh 1	11.2	12.7 ± 0.1	12.9 ± 0.2
ExCh 2	15.2	14.2 ± 0.1	13.92 ± 0.01
10 MV			
ExCh 2	11.0	10.9 ± 0.1	10.6 ± 0.2
25 MV*			
ExCh 2	16.4	13.4 ± 0.1	12.56 ± 0.02

* This experimental value from Gerbi and Khan is for a 24 MV Varian 2500 accelerator while the corresponding simulations are for a 25 MV Elekta SL25.

in polystyrene phantom and are closer to our Monte Carlo extrapolated $\%D_{gas}$ than the experimental values reported by the authors.

The results presented in this subsection confirm that uncalibrated extrapolation chambers can be used as an alternative dosimeter when calibrated chambers are not available even in regions where charged particle equilibrium is not fulfilled. However these chambers must be used within the range of electrode separations where it can be considered as a Bragg-Gray cavity. For the extrapolation chambers and energy beams investigated here that was achieved for plate separations less than 1 mm.

4.2.3 Parallel plate chamber dose conversion factors

In this subsection Monte Carlo correction factors for parallel plate chambers at the surface and in the build-up region of photon beams will be presented and discussed.

Buildup dose to water conversion factors

Figure 4–16 shows our Monte Carlo calculated dose conversion factor (D_w/D_{ch}) for the four parallel plate chambers investigated in this study as a function of depth z in water phantom in ^{60}Co beam.

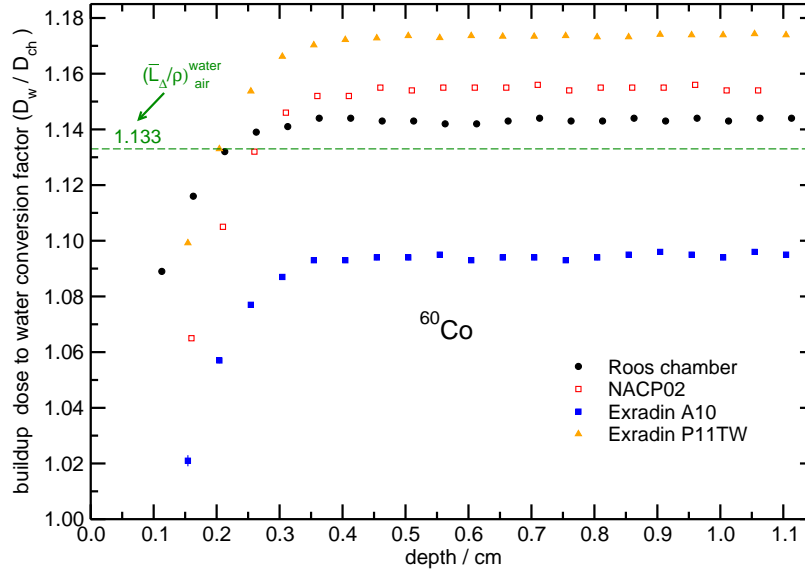


Figure 4–16: Dose to water conversion factor (D_w/D_{ch}) as a function of depth in the buildup region of a water phantom in ^{60}Co beam. Factors are calculated for the Roos (black circles), NACP02 (open red squares), Exradin A10 (solid blue squares) and Exradin P11TW (orange triangles) parallel plate chambers. The water-to-air restricted stopping-power ratio (at reference depth) is also shown for comparison.

We can see that for all chambers the dose conversion factor becomes constant for depths close and beyond the depth of maximum dose. That behaviour was expected since in those depths the chambers are in zones where transient charged particle equilibrium is fulfilled.

As discussed before in section 2.2, dose to water conversion factors, D_w/D_{ch} , must be equal the water-to-air stopping-power ratios modified by the perturbation factors, which for parallel plate chambers corresponds to the wall (P_{wall}) and replacement (P_{repl}) corrections. We can see from the plots in figure 4–16 that the conversion factors (D_w/D_{ch}) for the Roos chamber are the closest to the water-to-air

stopping-power ratio, $(\bar{L}_\Delta/\rho)_{air}^{water}$, of 1.133 in ^{60}Co beam for depths beyond the depth of maximum dose. This implies that the perturbation factors for this chamber must be close to unity in that region. Since P_{fl} is assumed to be unity for well guarded parallel plate chambers, P_{wall} is the most important component on the departure of D_w/D_{ch} from water-to-air stopping-power ratios. Averages over the doses ratios D_w/D_{ch} as well as perturbation factors from depths z between 0.5 cm and 1.1 cm were calculated for each chamber and are shown in table 4–8.

Table 4–8: Dose ratio D_w/D_{ch} and perturbation factors for parallel plate chambers in ^{60}Co beam. The values were averaged over the depths $0.5 \text{ cm} \leq z \leq 1.1 \text{ cm}$ in a $30 \times 30 \times 30 \text{ cm}^3$ water phantom.

Mean values for $0.5 \text{ cm} \leq z \leq 1.1 \text{ cm}$			
	D_w/D_{ch}	P_{wall}	P_{repl}
Roos	1.1434 ± 0.0002	1.0076 ± 0.0002	1.0012 ± 0.0002
NACP02	1.1546 ± 0.0002	1.0155 ± 0.0002	1.0034 ± 0.0002
Exradin A10	1.0943 ± 0.0002	0.9625 ± 0.0002	1.0032 ± 0.0002
Exradin P11TW	1.1735 ± 0.0001	1.0299 ± 0.0001	1.0054 ± 0.0001

Averaging over the wall perturbation factors for the Roos chamber at depths $0.5 \text{ cm} \leq z \leq 1.1 \text{ cm}$ provides a mean value of 1.0076 ± 0.0002 which is in agreement with the values of 1.0087, 1.0088, 1.0080 and 1.0074 obtained at reference depth ($z = 5.0 \text{ cm}$) by Mainegra-Hing et al [124], Buckley and Rogers [75], Zink and Wulff [59] and Muir and Rogers [60] respectively. Similarly, our mean value of 1.0012 ± 0.0002

for the P_{fl} after the buildup region is also close to the values of 1.005 and 1.006 calculated at reference depths by Zink and Wulff [53] and Muir and Rogers [60] respectively.

For the NACP02 chamber the average value for D_w/D_{ch} of 1.1546 ± 0.0002 is also closer to the stopping-power ratio than the values obtained with the other two chambers. The mean value for P_{wall} of 1.0155 ± 0.0002 evaluated for the depths beyond z_{max} also shows good agreement with the value 1.0204 calculated by Mainegra-Hing et al [124] at reference depth for that chamber.

Making averages of D_w/D_{ch} for the Exradin A10 and P11TW chambers after the buildup region provided the farthest values from the water to air stopping-power ratio. This also implies in values for the wall perturbation factors which are farther from unity when compared to those obtained with the other chambers as shown in table 4–8. This can be understood taking into account the different materials that compose the chamber walls (table 3–3) and how close they are to the surrounding phantom material. In this sense, the Roos chamber walls composed by polymethylmethacrylate (PMMA) water equivalent plastic have provided the smallest wall correction between the chambers investigated. On the other side, the largest values of P_{wall} for the Exradin A10 chamber can be understood looking at the air-equivalent plastic (C552) and polyoxymethylene materials that compose its walls. The values for P_{wall} averaged over $0.5 \text{ cm} \leq z \leq 1.1 \text{ cm}$ of 0.9625 ± 0.0002 for the Exradin A10 and 1.0299 ± 0.0001 for P11TW also agree with the values of 0.9621 and 1.0280 obtained by Mainegra-Hing et al [124] respectively for those chambers at reference depth.

Figure 4–17 shows build-up dose to water conversion factors for the four parallel plate chambers investigated in 6 MV photon beam.

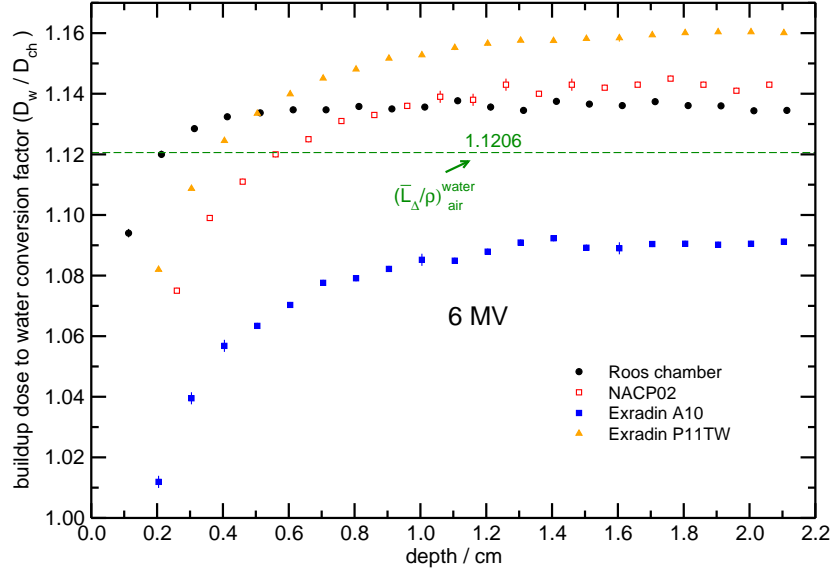


Figure 4–17: Dose to water conversions factors (D_w/D_{ch}) for parallel plate chambers in the buildup region of a 6 MV beam. Values of D_w and D_{ch} were calculated as a function of depth z for each chamber in a $30 \times 30 \times 30 \text{ cm}^3$ water phantom. The water-to-air restricted stopping-power ratio (at reference depth) is also shown for comparison.

Values of D_w/D_{ch} conversion factors for the Roos chamber goes from 1.094 ± 0.001 at $z = 0.113 \text{ cm}$ to 1.137 ± 0.001 at $z = 1.513 \text{ cm}$ (z_{max}) in the buildup region of the 6 MV beam. This implies a variation for D_w/D_{ch} with depth of around 3.8% relative to the value at $z = z_{max}$. The values obtained for the NACP02, Exradin A10 and P11TW chambers show variations with depth of around 6%, 7% and 6.5% respectively. As expected, D_w/D_{ch} also becomes constant for depths $z \geq z_{max}$. Similar

to what was observed in ^{60}Co beam, Exradin A10 and P11TW present the farthest values of D_w/D_{ch} from the water-to-air restricted stopping power ratio (≈ 1.1206) in 6 MV photon beam.

Figure 4–18 also shows the ratios D_w/D_{ch} for parallel plate chambers in the buildup region of a 10 MV photon beam as a function of depth in water phantom.

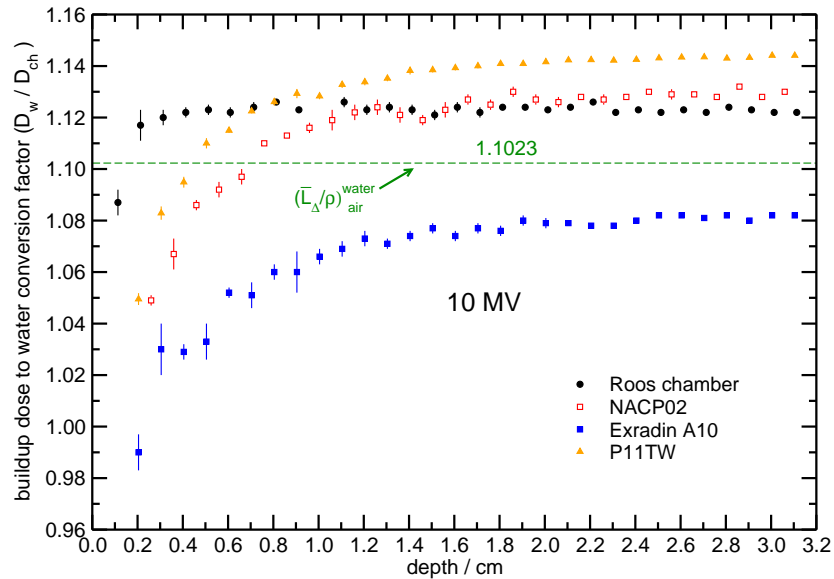


Figure 4–18: Dose to water conversion factors D_w/D_{ch} for Roos, NACP02, Exradin A10 and P11TW parallel plate chambers as a function of depth in the buildup region of a 10 MV beam. Calculations were done in a $30 \times 30 \times 30 \text{ cm}^3$ water phantom. The water-to-air restricted stopping-power ratio (at reference depth) is also shown for comparison.

The conversion factor becomes depth independent for depths greater than equal z_{max} ($\approx 2.3 \text{ cm}$ on average). Variations with depth were as large as 3.1%, 6.9%, 8.2% and 8% relative to the value of the conversions factor at z_{max} for the Roos, NACP02,

Exradin A10 and P11TW chambers respectively. Values of D_w/D_{ch} for the Roos and NACP02 chamber are also the closest to the mean restricted water-to-air stopping power ratio for 10 MV (≈ 1.1023).

Dose to water conversion factors D_w/D_{ch} as a function of depth for a 25 MV beam are shown in figure 4–19.

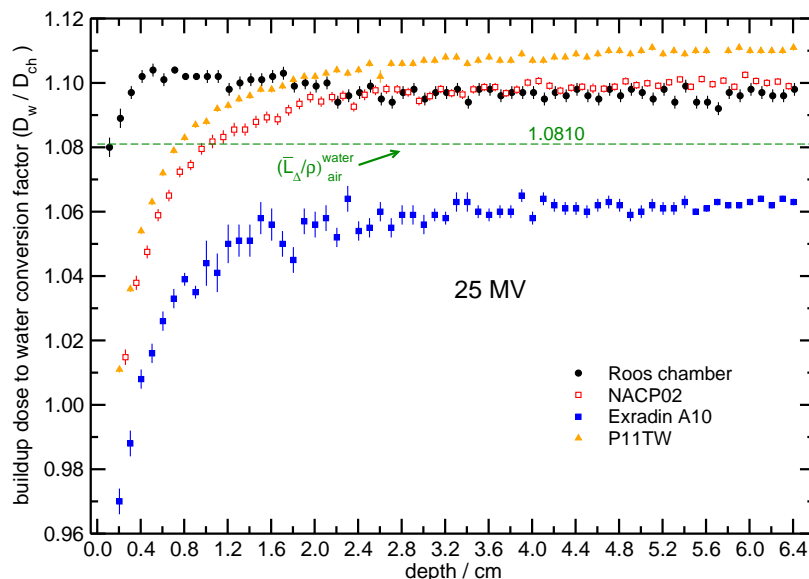


Figure 4–19: Dose to water conversion factors D_w/D_{ch} for Roos, NACP02, Exradin A10 and P11TW parallel plate chambers as a function of depth in the buildup region of a 25 MV beam. Calculations were done in a $30 \times 30 \times 30 \text{ cm}^3$ water phantom. The water-to-air restricted stopping-power ratio (at reference depth) is also shown for comparison.

Values are approximately constant for depths beyond $z_{max} \approx 3.7 \text{ cm}$. The largest variation with depth was observed for the Exradin P11TW chamber, which goes from 1.011 ± 0.001 at $z = 0.204 \text{ cm}$ to 1.1075 ± 0.0008 at $z = 3.7 \text{ cm}$. Variations

with depth for the Roos, NACP02 and Exradin A10 chambers were around 1.3%, 7.6% and 8.5% respectively. The curves show the same tendency presented for other energy beams with D_w/D_{ch} values for the Roos and NACP02 chambers close to $(\bar{L}_\Delta/\rho)_{air}^{water} = 1.0810$ for 25 MV photon beams.

As it would be expected, for all photon beams investigated, dose to water conversion factors are constant for depths beyond the depth of maximum dose (z_{max}) where transient charged particle equilibrium has been fulfilled. Average over the values of D_w/D_{ch} , P_{wall} and P_{repl} for depths $z \geq z_{max}$ are shown on table 4–9.

Analysis of the mean values for the perturbation factors after the build-up regions in table 4–8 and table 4–9 shows that our results obtained for parallel plate chambers are in good agreement with the results presented in figure 4–7 for the cylindrical chamber NE2571. Values of P_{repl} obtained for the four chambers in ^{60}Co , 6 MV, 10 MV and 25 MV beams are closer to unity than those found for the wall perturbation factor. This also confirms that P_{wall} is the major component of the overall perturbation factor and therefore is the most important component, after the stopping power, of the beam quality correction factor.

Polynomial fit curves of the form:

$$\frac{D_w}{D_{ch}} = A_0 + A_1(z) + A_2(z)^2 + A_3(z)^3 + \dots + A_n(z)^n \quad (4.7)$$

are proposed for providing buildup dose to water conversion factor for each chamber and for the four energy beams investigated. The best polynomial (degree) for fitting the data of D_w/D_{ch} as a function of depth was chosen according to the calculated values of χ^2/df . In this sense, polynomial fits with values of χ^2/df close to unity and

Table 4–9: Dose ratio D_w/D_{ch} and perturbation factors for parallel plate chambers in 6, 10 and 25 MV beams. The values were averaged over the depths beyond the depths of maximum dose (z_{max}) for each beam in a 30 x 30 x 30 cm³ water phantom. Depths of maximum dose were found to be on average 1.5 cm, 2.3 cm and 3.7 cm for 6, 10 and 25 MV beams respectively.

Mean values for $z \geq z_{max}$			
	D_w/D_{ch}	P_{wall}	P_{repl}
6 MV			
Roos	1.1355 ± 0.0005	1.0110 ± 0.0006	1.0003 ± 0.0005
NACP02	1.1430 ± 0.0005	1.0177 ± 0.0004	1.0029 ± 0.0005
Exradin A10	1.0902 ± 0.0005	0.9704 ± 0.0004	1.0033 ± 0.0005
Exradin P11TW	1.1593 ± 0.0002	1.0315 ± 0.0002	1.0039 ± 0.0004
10 MV			
Roos	1.1226 ± 0.0005	1.0128 ± 0.0005	1.0013 ± 0.0006
NACP02	1.1290 ± 0.0005	1.0180 ± 0.0003	1.0019 ± 0.0006
Exradin A10	1.0807 ± 0.0004	0.9758 ± 0.0004	1.0008 ± 0.0006
Exradin P11TW	1.1431 ± 0.0002	1.0311 ± 0.0002	1.0014 ± 0.0005
25 MV			
Roos	1.0961 ± 0.0003	1.0120 ± 0.0002	1.0007 ± 0.0005
NACP02	1.0995 ± 0.0002	1.0151 ± 0.0002	1.0008 ± 0.0004
Exradin A10	1.0618 ± 0.0002	0.9808 ± 0.0003	1.0002 ± 0.0005
Exradin P11TW	1.1088 ± 0.0004	1.0256 ± 0.0003	0.9990 ± 0.0004

with the less number of parameters were considered to be the most appropriate one for fitting the data.

The fit parameters A_0, A_1, \dots, A_n , as well as the root mean square deviation of the data from the fit are given in table 4–10 for the four parallel plate chambers investigated in the buildup region of ^{60}Co , 6, 10 and 25 MV photon beams. Results from table 4–10 show that for the most part of the chambers and energies investigated (44% of the cases) a 6th degree polynomial fit is adequate for providing D_w/D_{ch} values as a function of depth in water in the buildup region for $0.1 \text{ cm} < z \leq z_{max}$. In 25% and 31% of the cases a seventh and a fifth degree polynomial fits respectively provide the best values for the dose to water conversion factors.

Therefore, table 4–10 can be used for assessing the response of the four parallel plate chambers investigated in this study and commonly used radiotherapy clinics. With the data provided here more accurate data at non-reference conditions such as in the build-up region of photon beams can now be assessed.

Table 4–10: Fitting parameters for equation 4.7 for providing D_w/D_{ch} conversion factors in the buildup region of ^{60}Co , 6 MV, 10 MV and 25 MV beams. The corresponding rms deviation of the data from the fit are given in percentage in the last column. The fits are valid for depths $z \geq 0.113$ cm, and 0.26 cm for the Roos and NACP02 chambers respectively. For the Exradin A10 and P11TW fits are valid for depths $z \geq 0.204$ cm. The fits also apply until depths z of 1.1 cm, 2.1 cm, 3.1 cm and 6.4 cm for ^{60}Co , 6 MV, 10 MV and 25 MV beams respectively.

Chambers	A_0	A_1	A_2	A_3	A_4	A_5	A_6	A_7	rms % deviation
^{60}Co									
Roos	0.9789	1.4241	-4.6499	7.1779	-5.2736	1.4855	-	-	0.08
NACP	0.6959	4.0228	-14.4213	27.0544	-28.0352	15.2388	-3.4006	-	0.08
A10	0.784	2.465	-7.509	10.958	-7.690	2.086	-	-	0.1
P11TW	0.8323	2.8797	-9.6051	15.6502	-11.729	1.2658	3.1858	-1.3056	0.03
6 MV									
Roos	1.0327	0.7742	-2.4515	4.1187	-3.9351	2.1409	-0.6165	0.0728	0.07
NACP02	0.947	0.790	-1.490	1.551	-0.900	0.272	-0.0335	-	0.1
A10	0.924	0.605	-0.967	0.790	-0.316	0.0490	-	-	0.1
P11TW	0.957	0.9755	-2.3426	3.2486	-2.6645	1.2686	-0.3231	0.034	0.02
10 MV									
Roos	1.062	0.330	-0.641	0.594	-0.283	0.067	-0.006	-	0.2
NACP02	0.978	0.356	-0.356	0.178	-0.044	0.004	-	-	0.2
A10	0.950	0.292	-0.292	0.151	-0.039	0.004	-	-	0.4
P11TW	0.959	0.615	-0.934	0.756	-0.330	0.074	-0.006	-	0.1
25 MV									
Roos	1.076	0.080	-0.082	0.037	-0.008	0.001	-4e-05	-	0.2
NACP02	0.956	0.309	-0.310	0.171	-0.054	0.010	-0.001	4e-05	0.1
A10	0.930	0.253	-0.208	0.087	-0.019	0.002	-1e-04	-	0.3
P11TW	0.973	0.261	-0.217	0.093	-0.021	0.002	-1e-4	-	0.2

Surface dose to water conversion factors

Figure 4–20 shows dose to water conversion factors (D_w/D_{ch-SW}) for the Exradin A10 chamber at depths close to the surface ($0.03 \text{ mm} \leq z \leq 1.03 \text{ mm}$) of the phantom in photon beams. The factors were obtained from the ratio between the dose in the air cavity of the chamber in solid water phantom (D_{ch-SW}) and the dose to water (D_w) at the corresponding depth of the inside front face of the chamber.

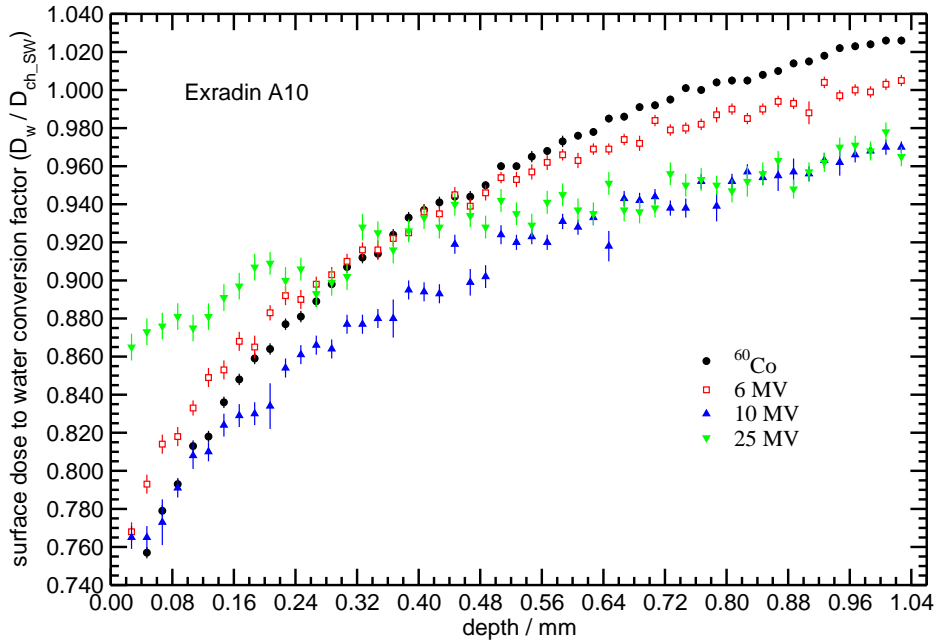


Figure 4–20: Surface dose to water conversion factor (D_w/D_{ch-SW}) as a function of depth within $0.03 \text{ mm} \leq z \leq 1.03 \text{ mm}$ for the Exradin A10 ion chamber. Curves are for ^{60}Co , 6 MV, 10 MV and 25 MV beams.

We can see from figure 4–20 that the dose to water conversion factors vary significantly with depth close to the surface of the phantom for all energy beams. The

plots also show that variation with depth decreases with increasing the energy beam. Percentage difference between the values of D_w/D_{ch} at $z = 0.03$ mm and $z = 1.03$ mm with respect the value at $z = 1.03$ mm were around 29%, 24%, 21% and 10% for ^{60}Co , 6 MV, 10 MV and 25 MV beams respectively. A possible explanation for that can be the scattering of contaminant electrons in the side walls of the chamber which in turn contributes to increase the dose in the air cavity of the chamber. This effect is less important for higher energy beams at the first layers of the phantom where the contaminant electrons are more forward directed, where the dose to the chamber is not larger than the dose to water as compared to lower energy beams. With increasing depth in the range $0.03 \text{ mm} \leq z \leq 1.03 \text{ mm}$, both doses to the water and to the chamber also increase although the contribution of electrons from the side wall for higher energy beams is still less important than it is for lower energy beams. On the other hand, the contribution of contaminant electrons for lower energy beams becomes less important with depth and then the dose to water increases more than the dose to the chamber.

Figure 4-21 also shows surface ($0.03 \text{ mm} \leq z \leq 1.03 \text{ mm}$) dose to water conversion factors (D_w/D_{ch-SW}) for the Exradin P11TW ion chamber in photon beams. The curves show similar behaviour to that observed for the Exradin A10 chamber. Maximum percentage differences with respect the value at $z = 1.03$ mm were as large as 28%, 24%, 22% and 11% for ^{60}Co , 6 MV, 10 MV and 25 MV respectively.

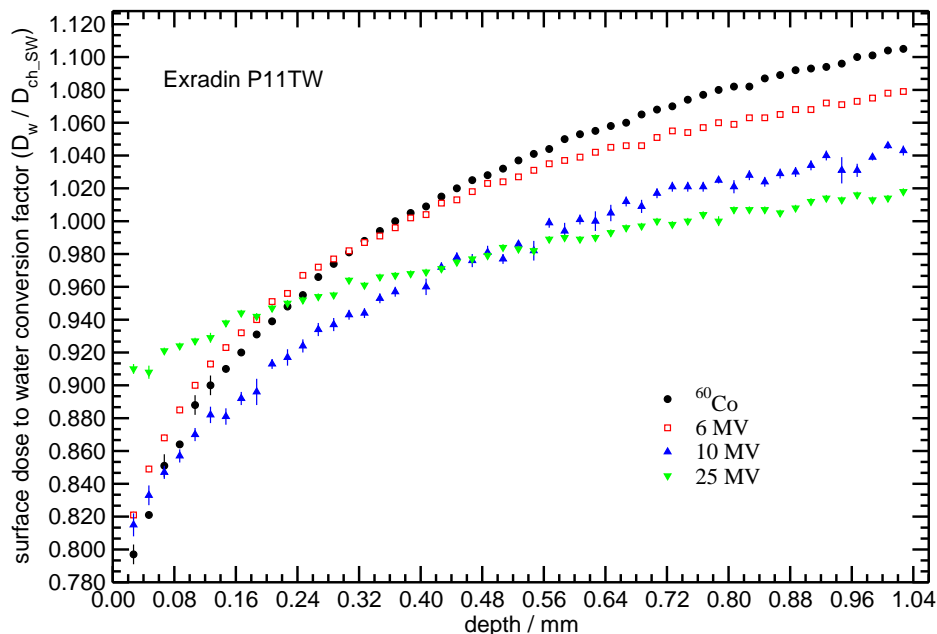


Figure 4–21: Surface dose to water conversion factor (D_w/D_{ch-SW}) as a function of depth within $0.03 \text{ mm} \leq z \leq 1.03 \text{ mm}$ for the Exradin P11TW ion chamber. Curves are for ^{60}Co , 6 MV, 10 MV and 25 MV beams.

Figure 4–22 compares the results for D_w/D_{ch-SW} obtained by the Exradin A10 and P11TW ionization chambers in the four energy photon beams investigated. The values of the dose to water conversion factors are also compared to water-to-air restricted stopping-power ratios calculated as a function of depth within $0.03 \text{ mm} \leq z \leq 1.03 \text{ mm}$. We can see from the plots that for all energy beams the correction needed for converting the dose to the chamber in solid water (D_{ch-SW}) to dose to water (D_w) are larger (far from $(\bar{L}_\Delta/\rho)_{air}^{water}$) for the Exradin A10 than the P11TW

ion chambers in the same depth range between 0.03 mm and 1.03 mm. This can be understood taking into account the wall materials of those chambers are basically polystyrene-equivalent plastic (D400) for the P11TW and air-equivalente plastic for the A10 as shown in table 3–3. This implies that wall corrections will be much larger for the Exradin A10 than those for the P11TW ones.

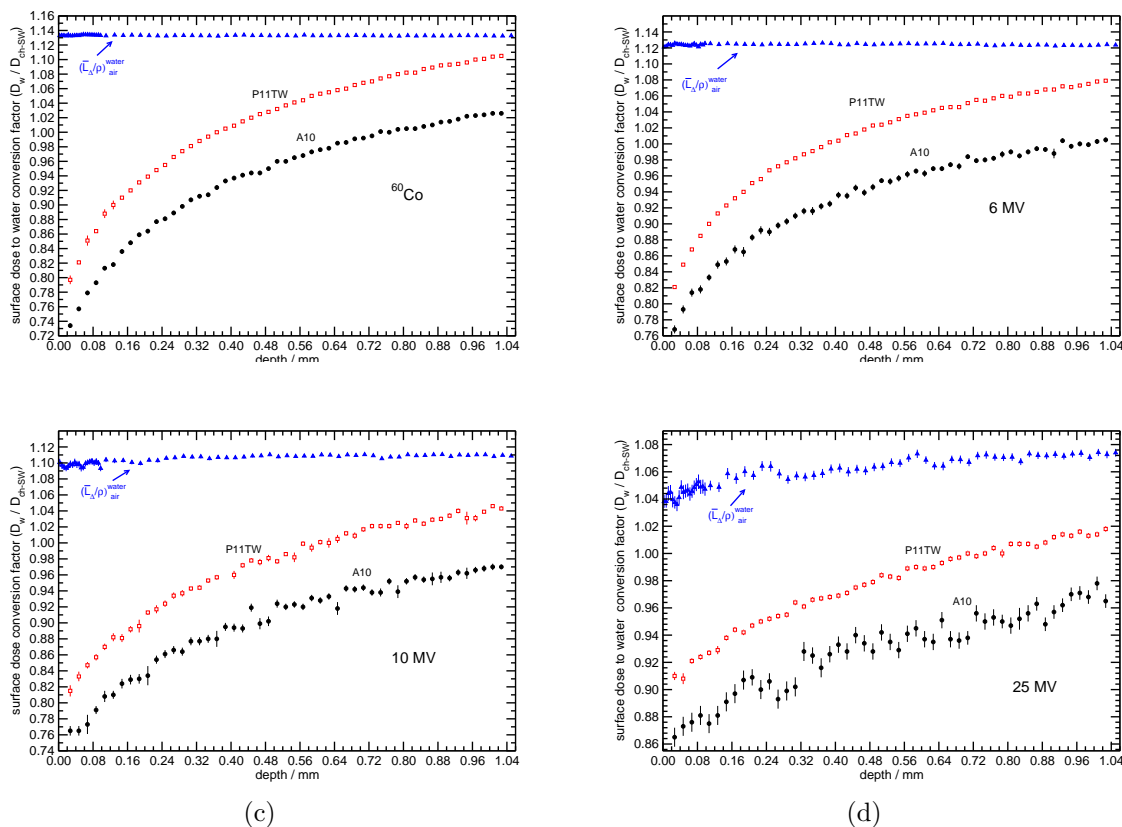


Figure 4–22: Comparison of surface ($0.03 \text{ mm} \leq z \leq 1.03 \text{ mm}$) dose to water conversion factors (D_w/D_{ch-SW}) for the Exradin A10 and P11TW chambers in ^{60}Co (a), 6 MV (b), 10 MV (c), and 25 MV (d). Values of $(\bar{L}_\Delta/\rho)_{air}^{water}$ as a function of depth are also plotted for comparison.

Table 4–11 shows the fit parameters for equation 4.7 for providing surface dose to water conversion factors (D_w/D_{ch-SW}) for the Exradin A10 and P11TW chambers at depths z between 0.03 mm and 1.03 mm. The fit are valid for using those parallel plate chambers in solid water phantom in photon beams of ^{60}Co , 6 MV, 10 MV and 25 MV.

Table 4–11: Fitting parameters for equation 4.7 for providing surface dose to water conversion factors as a function depth for the Exradin A10 and P11TW parallel plate chambers. The fits are valid for using those chambers at depths z within $0.03 \text{ mm} \leq z \leq 1.03 \text{ mm}$ in solid water phantom in ^{60}Co , 6 MV, 10 MV and 25 MV photon beams.

Chambers	A_0	A_1	A_2	A_3	A_4	A_5	A_6	A_7	rms % deviation
^{60}Co									
Exradin A10	0.714	1.046	-1.824	1.720	-0.630	-	-	-	0.3
Exradin P11TW	0.749	2.002	-9.778	33.18	-67.445	78.503	-48.169	12.06	0.2
6 MV									
Exradin A10	0.756	0.849	-1.511	1.435	-0.528	-	-	-	0.4
Exradin P11TW	0.787	1.51	-5.521	12.886	-16.997	11.519	-3.111	-	0.1
10 MV									
Exradin A10	0.743	0.743	-0.805	0.547	-0.140	-	-	-	0.6
Exradin P11TW	0.801	0.715	-1.113	0.995	-0.359	-	-	-	0.4
25 MV									
Exradin A10	0.861	0.207	-0.061	-0.210	0.174	-	-	-	0.7
Exradin P11TW	0.901	0.295	-0.446	0.433	-0.168	-	-	-	0.2

The most appropriate fit (polynomial degree) was also chosen according to best χ^2/df obtained and considering the polynomial with the lowest number of parameters. Table 4–11 shows that a fourth degree polynomial fit is appropriate for providing D_w/D_{ch-SW} conversion factors at depths $0.03 \text{ mm} \leq z \leq 1.03 \text{ mm}$ for the most part (75%) of the chambers and energy beams investigated. Only for the Exradin P11TW chamber in ^{60}Co and 6 MV beams a seventh and a sixth degree polynomials respectively were found to be the best option for fitting the data.

Values of D_w/D_{ch-SW} calculated with equation 4.7 and fit parameters given in table 4–11 for the Exradin A10 and P11TW at skin depth ($z = 0.07 \text{ mm}$) are shown in table 4–12 for the four photon beams investigated.

Table 4–12: Dose ratios D_w/D_{ch-SW} for the Exradin A10 and P11TW ion chambers positioned with their EPOM at the skin depth ($z = 0.07 \text{ mm}$) in a solid water phantom. Values were obtained with equation 4.7 and fit parameters given in table 4–11 for each photon beam.

D_w/D_{ch-SW} at $z = 0.07 \text{ mm}$		
Photon beam	A10	P11TW
^{60}Co	0.778 ± 0.003	0.851 ± 0.002
6 MV	0.809 ± 0.004	0.870 ± 0.001
10 MV	0.783 ± 0.006	0.846 ± 0.004
25 MV	0.875 ± 0.007	0.919 ± 0.002

We can see from the table 4–12 that corrections are larger (far from $(\bar{L}_\Delta/\rho)_{air}^{water}$) for the Exradin A10 ion chamber than those ones for the P11TW for all energy photon beams investigated. Percentage differences between the D_w/D_{ch-SW} ratios for the two chambers compared to the values obtained for the P11TW were around 8.6%, 7%, 7.4% and 4.8% for ^{60}Co , 6 MV, 10 MV and 25 MV.

Figure 4–23 shows the beam quality correction factor, k_{Q,Q_0} , as a function of depth at superficial depths $0.03 \text{ mm} \leq z \leq 1.03 \text{ mm}$ for the Exradin A10 chamber.

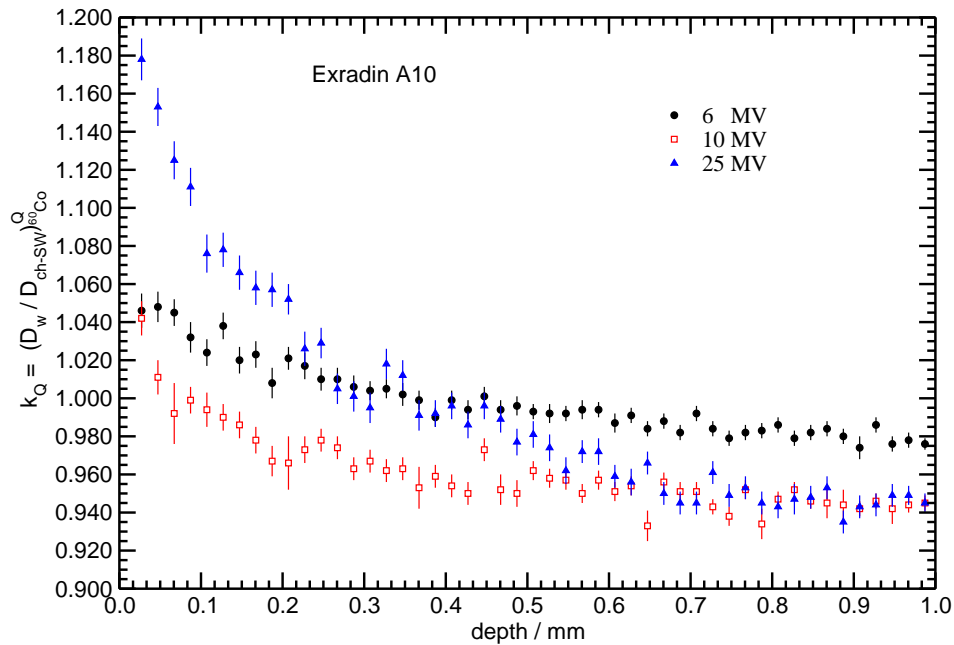


Figure 4–23: The beam quality correction factors, k_{Q,Q_0} , as a function of depth calculated as the ratio in two beam qualities (Q and ^{60}Co) of D_w/D_{ch-SW} for the Exradin A10 chamber. Values are shown for different depths within $0.03 \text{ mm} \leq z \leq 1.03 \text{ mm}$ at the surface of the phantom in 6 MV, 10 MV and 25 MV photon beams.

The values were obtained by making the ratio, in two qualities (Q and ^{60}Co), of dose to water (D_w) and dose to the air cavity of the chamber in solid water phantom (D_{ch-SW}). In this sense the curves are shown for the three mega-voltage photon beams used in this study. We can see from the plots in figure 4–23 that the largest variation with depth for k_Q was observed for the 25 MV beam. A maximum variation of 25% with respect the value at 1 mm depth was found for that energy beam. For 6 MV and 10 MV beams maximum variations with depth were around 6.8% and 10.3% respectively in the same depth range.

Figure 4–24 also shows k_Q values as a function of depth for the Exradin P11TW chamber for 6, 10 and 25 MV beams. The same methodology used previously for the A10 was also used for the P11TW chamber. We can see from figure 4–24 that the largest variation of k_Q with depth at the surface of the phantom was also observed for the 25 MV beam. Percentage difference between the values at $z = 0.03$ mm and $z = 1.03$ mm was found to be 24% for that energy beam. For 6 and 10 MV maximum variations were around 5.5% and 8.4% respectively.

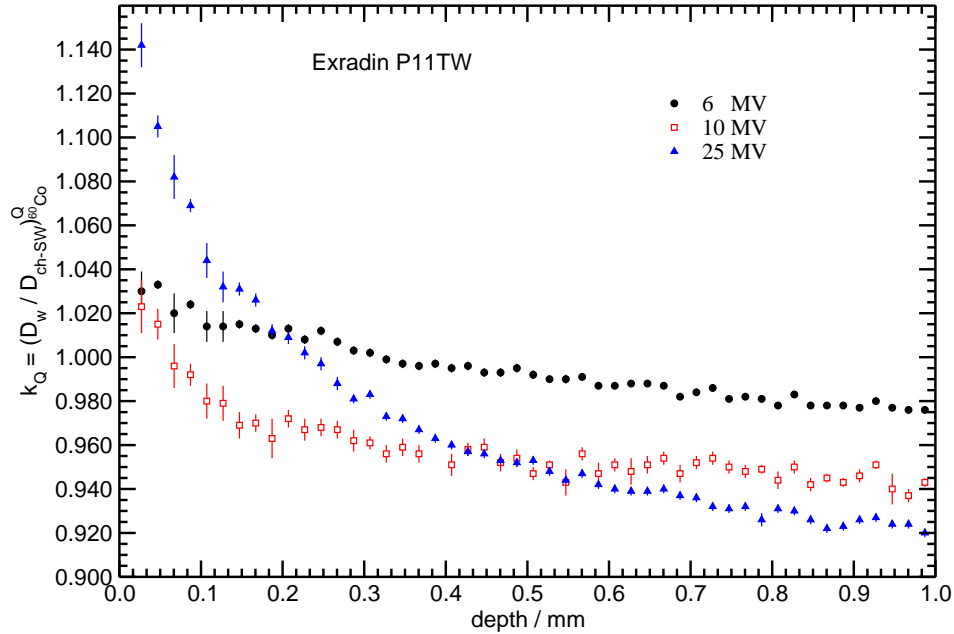
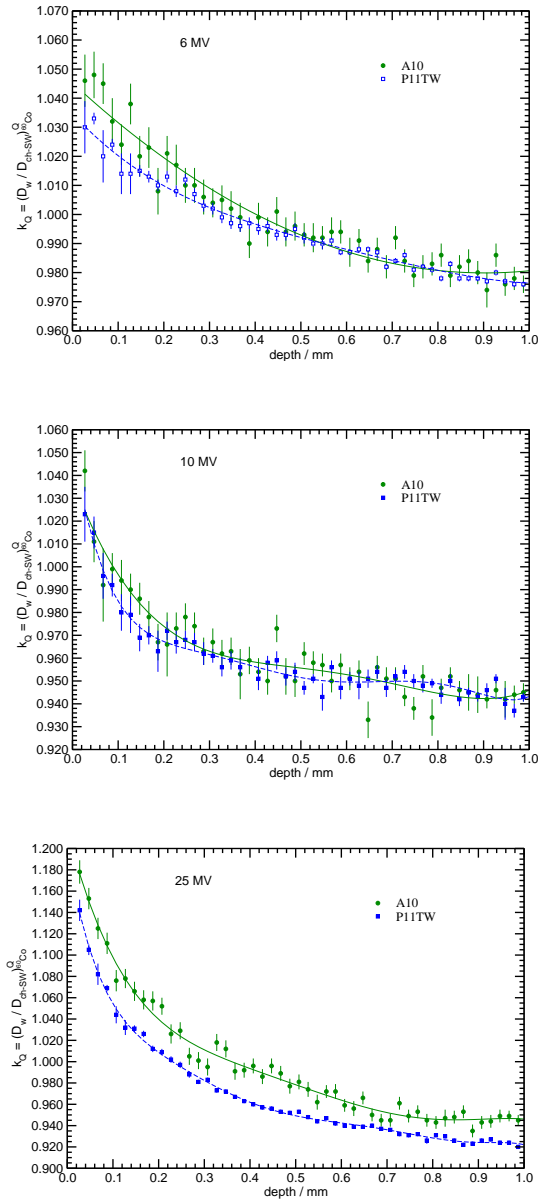


Figure 4–24: Same as shown in figure 4–23 but now for the Exradin P11TW ion chamber.

Figure 4–25 compares the values of k_Q in each energy beam for the two chambers together. Polynomial fits according to equation 4.7 are also shown in figure 4–25 for each chamber in the three energy photon beams for providing k_Q values within the range $0.03 \text{ mm} \leq z \leq 1.03 \text{ mm}$ at the surface of the phantom. The fit parameters for each chamber as well as the rms deviations of the data from the fit in percentage are given in table 4–13.



(c)

Figure 4-25: Comparison of the values of k_Q as a function of depth obtained for the A10 (solid green circles) and P11TW (open blue squares) ion chambers in 6 MV (a), 10 MV (b) and 25 MV (c) beams. Polynomial fits for the A10 (solid green line) and P11TW (dashed blue line) are shown for providing k_Q values within the range $0.03 \text{ m} \leq z \leq 1.03 \text{ mm}$.

Table 4–13: Fitting parameters for equation 4.7 for providing k_Q values at the surface of water phantom from measurements with the Exradin A10 and P11TW ion chambers in solid water. The fit is valid for using the chambers in depths $0.03 \text{ mm} \leq z \leq 1.03 \text{ mm}$. The rms deviation of the data from the fits are given in percentage in the last column.

Chambers	A_0	A_1	A_2	A_3	A_4	A_5	A_6	A_7	rms %deviation
6 MV									
Exradin A10	1.045	-0.145	0.080	-	-	-	-	-	0.5
Exradin P11TW	1.035	-0.170	0.283	-0.281	0.110	-	-	-	0.2
10 MV									
Exradin A10	1.038	-0.537	1.373	-1.585	0.657	-	-	-	0.7
Exradin P11TW	1.052	-1.139	6.278	-18.26	28.02	-21.43	6.418	-	0.4
25 MV									
Exradin A10	1.217	-1.644	5.377	-9.47	8.061	-2.595	-	-	0.7
Exradin P11TW	1.197	-2.5	15.34	-56.82	121	-145	90.71	-23.01	0.3

Results summarized in table 4–11 and table 4–13 allows one to calculate beam quality correction factors near the surface ($0.03 \text{ mm} \leq z \leq 1.03 \text{ mm}$) of water phantoms using the Exradin A10 and P11TW chambers which have the thinnest window thickness between the chambers investigated. Therefore these factors allow a direct determination of absorbed dose to water from measurements with the chambers in solid water phantoms without water-proofing caps. Values of absorbed dose to water at skin depths can also be assessed using the data provided in this study.

CHAPTER 5

Conclusions

This work presented a detailed study of correction factors for ionization chambers at reference conditions as well as an investigation of parallel plate chambers response in the build-up region of photon beams. Results obtained with the NE2571 confirms the use of Monte Carlo simulations to provide perturbation and beam quality correction factors for this ionization chamber in radiotherapy. The proposed methodology of using phase-space files in PENELOPE code presented a significant efficiency gain and can be applied for a variety of ionization chambers and energy beams used in clinics.

Results obtained with the EGSnrc system suggests that parallel plate chambers can be used to assess surface doses in radiotherapy once dose conversion factors are accurately provided. The set of data for the four parallel plate chambers investigated in this study provides useful informations for dosimetry at the surface and in the build-up region of photon beams. In this sense the results presented here represent an important contribution in radiation dosimetry at non-reference conditions. This also encourages further investigations for other ionization chambers and radiation beams.

Therefore, the results presented here are expected to contribute with improving dosimetry protocols and therefore to guarantee the quality of life of radiotherapy patients.

Appendix A: MATLAB program for calculating average restricted stopping power ratios

```
1 %This program calculates the Spencer-Attix (SA) water to air stopping-power
2 % ratio, which includes the track-end terms for electrons with energies
3 %  $E < \Delta$ . The equation that defines the SA stopping-power can be found
4 % in the original paper from Nahum (Phys.Med.Biol. 23,24-38,1978) or in the
5 % paper from Borg et al (Med.Phy. 27(8),1804-1813, 2000).
6 %%%%%%%%%%%%%%%%%%%%%%%%%%%%%%%%%%%%%%%%%%%%%%%%%%%%%%%%%%%%%%%%%%%%%%%%%
7 %           BEGIN
8 %
9 %%%%%%%%%%%%%%%%%%%%%%%%%%%%%%%%%%%%%%%%%%%%%%%%%%%%%%%%%%%%%%%%%%%%%%%%%
10 %load -ascii csp_air;   Unrestricted stopping powers to air
11 %load -ascii csp_water; Unrestricted stopping powers to water
12 %load -ascii rsp_air;   Restricted stopping powers to air
13 %load -ascii rsp_water; Restricted stopping powers to air
14 %load -ascii fluelec_err;
15 delta=10000.0;
16 spdelta_air=0.0000;
17 spdelta_water=0.0000;
18 energy = 0.0;
19 Dw = 0.000;
20 Dg = 0.000;
21 dDw = 0.0000;
22 dDg = 0.0000;
23 num_err=0.00000;
```

```

23 den_err=0.00000;
24 sum_en_spr_dflu2_w = 0.00000;
25 sum_en_spr_dflu2_g = 0.00000;
26 error=0.00000;
27 a=0.00000;
28 spe_air=zeros(length(fluelec_err),2);
29 spe_water=zeros(length(fluelec_err),2);
30 %%%%%%%%%%%%%%%%%%%%%%%%%%%%%%%%%%%%%%%%%%%%%%%%%%%%%%%%%%%%%%%%%%%%%%%%%
31 %Storing the Unrestricted stopping-power for energies E < delta in each medium
32 %%%%%%%%%%%%%%%%%%%%%%%%%%%%%%%%%%%%%%%%%%%%%%%%%%%%%%%%%%%%%%%%%%%%%%%%%
33 for i=1:length(csp_water)
34     energ=csp_water(i,1);
35     if energ==delta,
36         spdelta_water=csp_water(i,2);
37     else
38         for j=2:length(csp_water)
39             b=csp_water(j-1,1);
40             c=csp_water(j,1);
41             if delta~>=b,
42                 if b<delta && delta<c,
43                     Em = delta;
44                     E1=csp_water(j-1,1);
45                     E2=csp_water(j,1);
46                     S1=csp_water(j-1,2);
47                     S2=csp_water(j,2);
48                     spdelta_water=(S2*(E1-Em)-S1*(E2-Em))/(E1-E2);
49                 end
50             end

```

```

51         end
52     end
53 end
54 for i=1:length(csp_air)
55     energ=csp_air(i,1);
56     if energ==delta,
57         spdelta_air=csp_air(i,2);
58     else
59         for j=2:length(csp_air)
60             b=csp_air(j-1,1);
61             c=csp_air(j,1);
62             if delta~=b,
63                 if b<delta && delta<c,
64                     Em = delta;
65                     E1=csp_air(j-1,1);
66                     E2=csp_air(j,1);
67                     S1=csp_air(j-1,2);
68                     S2=csp_air(j,2);
69                     spdelta_air=(S2*(E1-Em)-S1*(E2-Em))/(E1-E2);
70                 end
71             end
72         end
73     end
74 end
75 %%%%%%%%%%%%%%%%%%%%%%%%%%%%%%%%%%%%%%%%%%%%%%%%%%%%%%%%%%%%%%%%%%%%%%%%%
76 %   The dose to the medium (Dw) term that goes in the numerator of the
77 %   SA stopping power equation.
78 %%%%%%%%%%%%%%%%%%%%%%%%%%%%%%%%%%%%%%%%%%%%%%%%%%%%%%%%%%%%%%%%%%%%%%%%%

```

```

79 %Filling out the array spe_water (Ener x Sto-Power) with SP values whose
80 %ENERGY IS THE SAME AS THOSE ONES IN THE fluelec_err VECTOR.
81 %The vector fluelec_err is read to verify if its energy is equal the energy
82 %of the sp's (restricted and unrestricted).If this is true, the stop-pow
83 %value is picked up and a vector Ener x Sto-Power is built (spe).
84 %It is also checked if E > delta.
85 for i=1:length(fluelec_err)
86     a=fluelec_err(i,1);
87     if a>delta,
88         for j=1:length(rsp_water)
89             b=rsp_water(j,1);
90             if a==b,
91                 spe_water(i,1)=fluelec_err(i,1);
92                 spe_water(i,2)=rsp_water(j,2);
93             end
94         end
95     else
96         for j=1:length(csp_water)
97             b=csp_water(j,1);
98             if a==b,
99                 spe_water(i,1)=delta;
100                spe_water(i,2)=spdelta_water;
101            end
102        end
103    end
104 end
105 %Reading the fluelec_err vector to verify if its ENERGY IS BETWEEN TWO
106 %ENERGIES of the spr's. If this is true, the stop-pow value is interpolated

```

```

107 %and the vector spe_water is filled out. It is also checked if E > delta.
108 for i=1:length(fluelec_err)
109     a=fluelec_err(i,1);
110     if a>delta,
111         for j=2:length(rsp_water)
112             b=rsp_water(j-1,1);
113             c=rsp_water(j,1);
114             if a~b,
115                 if b<a && a<c,
116                     spe_water(i,1)=fluelec_err(i,1);
117                     Em = spe_water(i,1);
118                     E1=rsp_water(j-1,1);
119                     E2=rsp_water(j,1);
120                     S1=rsp_water(j-1,2);
121                     S2=rsp_water(j,2);
122                     spe_water(i,2)=(S2*(E1-Em)-S1*(E2-Em))/(E1-E2);
123                 end
124             end
125         end
126     else
127         for j=2:length(csp_water)
128             b=csp_water(j-1,1);
129             c=csp_water(j,1);
130             if a~b,
131                 if b<a && a<c,
132                     spe_water(i,1)=delta;
133                     spe_water(i,2)=spdelta_water;
134                 end

```

```

135         end
136     end
137 end
138 %Calculating the dose to the medium (water)
139     Dw = Dw + fluelec_err(i,2)*spe_water(i,2);
140     %The sum of each error squared
141     sum_en_spr_dflu2_w = sum_en_spr_dflu2_w + (spe_water(i,2)*fluelec_err(i,3))^2;
142
143 end
144
145 %Calculation of the error dDw.
146 dDw = sqrt(sum_en_spr_dflu2_w);
147 %%%%%%%%%%%%%%%%%%%%%%%%%%%%%%%%%%%%%%%%%%%%%%%%%%%%%%%%%%%%%%%%%%%%%%%%%
148 % The dose to the gas (Dg) term that goes in the denominator of the
149 % SA stopping power equation.
150 %%%%%%%%%%%%%%%%%%%%%%%%%%%%%%%%%%%%%%%%%%%%%%%%%%%%%%%%%%%%%%%%%%%%%%%%%
151 %Filling out the array spe_air (Ener x Sto-Power) with SP values whose
152 %ENERGY IS THE SAME IN THE ARRAY fluelec_err. It is also checked if
153 %E > delta.
154 for i=1:length(fluelec_err)
155     a=fluelec_err(i,1);
156     if a>delta,
157         for j=1:length(rsp_air)
158             b=rsp_air(j,1);
159             if a==b,
160                 spe_air(i,1)=fluelec_err(i,1);
161                 spe_air(i,2)=rsp_air(j,2);
162             end

```

```

163         end
164     else
165         for j=1:length(csp_air)
166             b=csp_air(j,1);
167             if a==b,
168                 spe_air(i,1)=delta;
169                 spe_air(i,2)=spdelta_air;
170             end
171         end
172     end
173 end
174 %Reading the flue to verify if its ENERGY IS BETWEEN TWO ENERGIES of the
175 %sp files.%If this is true, the stop-pow value is interpolated and the
176 %vector spe_air is filled out. It is also checked if E > delta.
177 for i=1:length(fluelec_err)
178     a=fluelec_err(i,1);
179     if a>delta,
180         for j=2:length(rsp_air)
181             b=rsp_air(j-1,1);
182             c=rsp_air(j,1);
183             if a~b,
184                 if b<a && a<c,
185                     spe_air(i,1)=fluelec_err(i,1);
186                     Em = spe_air(i,1);
187                     E1=rsp_air(j-1,1);
188                     E2=rsp_air(j,1);
189                     S1=rsp_air(j-1,2);
190                     S2=rsp_air(j,2);

```

```

191             spe_air(i,2)=(S2*(E1-Em)-S1*(E2-Em))/(E1-E2);
192         end
193     end
194 end
195 else
196     for j=2:length(csp_air)
197         b=csp_air(j-1,1);
198         c=csp_air(j,1);
199         if a~=b,
200             if b<a && a<c,
201                 spe_air(i,1)=delta;
202                 spe_air(i,2)=spdelta_air;
203             end
204         end
205     end
206 end
207 %Calculating the dose to the gas (air)
208 Dg = Dg + fluelec_err(i,2)*spe_air(i,2);
209 %The sum of each error squared
210 sum_en_spr_dflu2_g = sum_en_spr_dflu2_g + (spe_air(i,2)*fluelec_err(i,3))^2;
211 end
212 %Calculation of the error dDg.
213 dDg = sqrt(sum_en_spr_dflu2_g);
214
215 %%%%%%%%%%%%%%%%%%%%%%%%%%%%%%%%%%%%%%%%%%%%%%%%%%%%%%%%%%%%%%%%%%%%%%%%%
216 % Finally the average restricted stopping power by Dw/Dg
217 %%%%%%%%%%%%%%%%%%%%%%%%%%%%%%%%%%%%%%%%%%%%%%%%%%%%%%%%%%%%%%%%%%%%%%%%%
218 asp=(Dw)/(Dg);

```

```
219 num_err = sqrt((Dw*dDg)^2+(Dg*dDw)^2);
220 den_err = (Dg)^2;
221 error = (num_err)/(den_err);
222 fprintf('Average Stopping-Power =%g\n',asp);
223 fprintf('Err_SP =%g\n',error);
```

REFERENCES

- [1] B. Nilsson and A. Montelius, Fluence perturbation in photon beams under nonequilibrium conditions, *Med. Phys.* **13**, 191 – 195 (1986).
- [2] B. J. Gerbi and F. M. Khan, Measurement of dose in the buildup region using fixed-separation plane-parallel ionization chambers, *Med. Phys.* **17**, 17 – 26 (1990).
- [3] ICRU, Prescribing, Recording and Reporting Photon Beam Therapy (Supplement to ICRU Report 50), ICRU Report 62, ICRU, Washington D.C., 1999.
- [4] G. Ibbott, C.-M. C. Ma, D. W. O. Rogers, S. Seltzer, and J. Williamson, Fifty years of AAPM involvement in radiation dosimetry, *Med. Phys.* **35**, 1418 – 1427 (2008).
- [5] IAEA, *Absorbed Dose Determination in External Beam Radiotherapy: An International Code of Practice for Dosimetry Based on Standards of Absorbed Dose to Water*, volume 398 of *Technical Report Series*, IAEA, Vienna, 2001.
- [6] P. R. Almond, P. J. Biggs, B. M. Coursey, W. F. Hanson, M. S. Huq, R. Nath, and D. W. O. Rogers, The AAPM's TG-51 Protocol for Clinical Reference Dosimetry of High-Energy Beams, *Med. Phys.* (abstract) **26**, 1058 (1999).
- [7] D. W. O. Rogers, The advantages of absorbed-dose calibration factors, *Med. Phys.* **19**, 1227 – 1239 (1992).
- [8] P. Andreo, Absorbed dose beam quality factors for the dosimetry of high-energy photon beams, *Phys. Med. Biol.* **37**, 2189 – 2211 (1992).
- [9] IAEA, *Absorbed Dose Determination in Photon and Electron Beams; An International Code of Practice*, volume 277 of *Technical Report Series*, IAEA, Vienna, 1987.
- [10] AAPM TG-21, A protocol for the determination of absorbed dose from high-energy photon and electron beams, *Med. Phys.* **10**, 741 – 771 (1983).

- [11] D. J. La Russa and D. W. O. Rogers, Accuracy of Spencer-Attix cavity theory and calculations of fluence correction factors for the air kerma formalism, *Med. Phys.* **36**, 4173 – 4183 (2009).
- [12] L. V. Spencer and F. H. Attix, A theory of cavity ionization, *Radiat. Res.* **3**, 239 – 254 (1955).
- [13] D. J. La Russa and D. W. O. Rogers, Accuracy of EGSnrc calculations of the response of various ion chambers to ^{60}Co beams, *Med. Phys.* **35**, 5629 – 5640 (2008).
- [14] J. Borg, I. Kawrakow, D. W. O. Rogers, and J. P. Seuntjens, Monte Carlo study of correction factors for Spencer-Attix cavity theory at photon energies at or above 100 keV, *Med. Phys.* **27**, 1804 – 1813 (2000).
- [15] J. Fisher, C. Scott, R. Stevens, B. Marconi, L. Champion, G. M. Freedman, F. Asrari, M. Pilepich, J. D. Gagnon, and G. Wong, Randomized phase {III} study comparing best supportive care to biafine as a prophylactic agent for radiation-induced skin toxicity for women undergoing breast irradiation: Radiation therapy oncology group (RTOG) 97-13, *Int. J. Radiat. Oncol. Biol. Phys.* **48**, 1307 – 1310 (2000).
- [16] N. Lee, C. Chuang, J. M. Quivey, T. L. Phillips, P. Akazawa, L. J. Verhey, and P. Xia, Skin toxicity due to intensity-modulated radiotherapy for head-and-neck carcinoma, *Int. J. Radiat. Oncol. Biol. Phys.* **53**, 630 – 637 (2002).
- [17] M. Back, M. Guerrieri, C. Wratten, and A. Steigler, Impact of Radiation Therapy on Acute Toxicity in Breast Conservation Therapy for Early Breast Cancer, *Clinical Oncology* **16**, 12 – 16 (2004).
- [18] L. E. Court and R. B. Tishler, Experimental Evaluation of the Impact of Different Head-and-Neck Intensity-Modulated Radiation Therapy Planning Techniques on Doses to the Skin and Shallow Targets, *Int. J. Radiat. Oncol. Biol. Phys.* **69**, 607 – 613 (2007).
- [19] E. P. Saibishkumar, M. A. MacKenzie, D. Severin, A. Mihai, J. Hanson, H. Daly, G. Fallone, M. B. Parliament, and B. S. Abdulkarim, Skin-Sparing Radiation Using Intensity-Modulated Radiotherapy After Conservative Surgery in Early-Stage Breast Cancer: A Planning Study, *Int. J. Radiat. Oncol. Biol. Phys.* **70**, 485 – 491 (2008).

- [20] B. S. Hoppe, B. Laser, A. V. Kowalski, S. C. Fontenla, E. Pena-Greenberg, E. D. Yorke, D. M. Lovelock, M. A. Hunt, and K. E. Rosenzweig, Acute Skin Toxicity Following Stereotactic Body Radiation Therapy for Stage I NonSmall-Cell Lung Cancer: Who's at Risk?, *International Journal of Radiation Oncology Biology Physics* **72**, 1283 – 1286 (2008).
- [21] W. SOUTHWOOD, The thickness of the skin., *Plastic and reconstructive surgery* **15**, 423–429 (1955).
- [22] C. von Essen, Radiation tolerance of the skin., *Acta radiologica: therapy, physics, biology* **8**, 311 – 330 (1969).
- [23] J. Hopewell, The Skin: Its Structure and Response to Ionizing Radiation, *International Journal of Radiation Biology* **57**, 751 – 773 (1990).
- [24] ICRU, Report85: Fundamental Quantities and Units for Ionizing Radiation, *J of the ICRU* **11**, 1 – 33 (2011).
- [25] A. W. Ham and D. H. Cormack, *Histology*, Lippincott, Philadelphia, 1979.
- [26] C. R. Ehemann, M. C. McFee, S. M. Selden, and G. G. Eichholz, Measuring the skin dose from radioactively contaminated gold rings using LiF thermoluminescent powder, *Health Phys.* **56**, 547 (1989).
- [27] S. Alashrah, S. Kandaiya, N. Maalej, and A. El-Taher, Skin dose measurements using radiochromic films, TLDS and ionisation chamber and comparison with Monte Carlo simulation, *Radiation Protection Dosimetry* **162**, 338–344 (2014).
- [28] D. E. Velkley, D. J. Manson, J. A. Purdy, and J. G. D. Oliver, Build-up region of megavoltage photon radiation sources, *Med. Phys.* **2**, 14 – 19 (1975).
- [29] D. E. Mellenberg, Determination of build-up region over-response corrections for a Markus-type chamber, *Med. Phys.* **17**, 1041 – 1044 (1990).
- [30] W. Abdel-Rahman, J. P. Seuntjens, F. Verhaegen, F. Deblois, and E. B. Podgorsak, Validation of Monte Carlo calculated surface doses for megavoltage photon beams, *Med. Phys.* **32**, 286 – 298 (2005).
- [31] E. I. Parsai, D. Shvydka, D. Pearson, M. Gopalakrishnan, and J. J. Feldmeier, Surface and build-up region dose analysis for clinical radiotherapy photon beams, *Applied Radiation and Isotopes* **66**, 1438 – 1442 (2008).

- [32] S. T. Hsu, J. M. Moran, Y. Chen, R. Kulasekere, and P. L. Roberson, Dose discrepancies in the buildup region and their impact on dose calculations for IMRT fields, *Med. Phys.* **37**, 2043 – 2053 (2010).
- [33] T. Kron, A. Elliot, T. Wong, G. Showell, B. Clubb, and P. Metcalfe, X-ray surface dose measurements using TLD extrapolation, *Med. Phys.* **20**, 703 – 711 (1993).
- [34] S. Stathakis, J. S. Li, K. Paskalev, J. Yang, L. Wang, and C.-M. Ma, Ultra-thin TLDs for skin dose determination in high energy photon beams, *Phys. Med. Biol.* **51**, 3549 – 3567 (2006).
- [35] S. F. Kry, S. A. Smith, R. Weathers, and M. Stovall, Skin dose during radiotherapy: a summary and general estimation technique, *J of App Clin Med Phys* **13**, 20 – 34 (2012).
- [36] B. Bjärngård, P. Vadash, and T. Zhu, Doses near the surface in high-energy x-ray beams, *Med. Phys.* **22**, 465 – 468 (1995).
- [37] N. Jornet, M. Ribas, and T. Eudaldo, In vivo dosimetry: Intercomparison between p-type based and n-type based diodes for the 16-25 MV energy range, *Med. Phys.* **27**, 1287 – 1293 (2000).
- [38] M. J. Butson, A. Rozenfeld, J. N. Mathur, M. Carolan, T. P. Y. Wong, and P. E. Metcalfe, A new radiotherapy surface dose detector: The MOSFET, *Med. Phys.* **23**, 655 – 658 (1996).
- [39] S. Devic, J. Seuntjens, W. Abdel-Rahman, M. Evans, M. Olivares, E. B. Podgorsak, T. Vuong, and C. G. Soares, Accurate skin dose measurements using radiochromic film in clinical applications, *Med. Phys.* **33**, 1116 – 1124 (2006).
- [40] B. Demir, M. Okutan, A. Akir, E. Gksel, and H. Bilge, The Effect of Oblique Electron Beams to the Surface Dose Under the Bolus, *Medical Dosimetry* **34**, 311 – 316 (2009).
- [41] G. A. Cho, A. Ralston, M. M. Tin, D. Martin, S. Pickard, J.-H. Kim, and R. Tse, In vivo and phantom measurements versus Eclipse TPS prediction of near surface dose for SBRT treatments, *Journal of Physics: Conference Series* **489**, 012008 (2014).

- [42] J. A. Rawlinson, D. Arlen, and D. Newcombe, Design of parallel plate ion chambers for buildup measurements in megavoltage photon beams, *Med. Phys.* **19**, 641 – 648 (1992).
- [43] S. C. Klevenhagen, Determination of absorbed dose in high-energy electron and photon radiation by means of an uncalibrated ionization chamber, *Phys. Med. Biol.* **36**, 239 (1991).
- [44] C. E. Zankowski and E. B. Podgorsak, Calibration of photon and electron beams with an extrapolation chamber, *Med. Phys.* **24**, 497 – 503 (1997).
- [45] G. Failla, The measurement of tissue dose in terms of the same unit for all ionizing radiations, *Radiology* **29**, 202 – (1937).
- [46] D. J. Manson, D. Velkley, J. A. Purdy, and G. D. Oliver, Measurements of Surface Dose Using Build-Up Curves Obtained with an Extrapolation Chamber, *Radiology* **115**, 473–474 (1975), PMID: 806935.
- [47] T. P. Selvam, P. R. B. Saull, and D. W. O. Rogers, Monte Carlo modelling of the response of NRC's $^{90}\text{Sr}/^{90}\text{Y}$ primary beta standard, *Med. Phys.* **32**, 3084 – 3094 (2005).
- [48] J. Baro, J. Sempau, J. M. Fernandez-Varea, and F. Salvat, PENELOPE: an algorithm for Monte Carlo simulation of the penetration and energy loss of electrons and positrons in matter, *Nucl. Inst. Meth. B* **100**, 31 – 46 (1995).
- [49] J. Sempau, J. M. Fernandez-Varea, E. Acosta, and F. Salvat, Experimental benchmarks of the Monte Carlo code PENELOPE, *Nucl. Inst. Meth. B* **207**, 107 – 123 (2003).
- [50] D. W. O. Rogers, Fifty years of Monte Carlo simulations for medical physics, *Phys. Med. Biol.* **51**, R287 – R301 (2006).
- [51] I. Kawrakow, E. Mainegra-Hing, D. W. O. Rogers, F. Tessier, and B. R. B. Walters, The EGSnrc Code System: Monte Carlo simulation of electron and photon transport, NRC Technical Report PIRS-701 v4-2-3-2, National Research Council Canada, Ottawa, Canada. <http://www.irs.inms.nrc.ca/inms/irs/EGSnrc/EGSnrc.html>, 2011.
- [52] J. Wulff, J. T. Heverhagen, and K. Zink, Monte-Carlo-based perturbation and beam quality correction factors for thimble ionization chambers in high-energy photon beams, *Phys. Med. Biol.* **53**, 2823 – 2836 (2008).

- [53] K. Zink and J. Wulff, Monte Carlo calculations of beam quality correction factors k_Q for electron dosimetry with a parallel-plate Roos chamber, *Phys. Med. Biol.* **53**, 1595 – 1607 (2008).
- [54] J. Wulff, K. Zink, and I. Kawrakow, Efficiency improvements for ion chamber calculations in high energy photon beams, *Med. Phys.* **35**, 1328– 1336 (2008).
- [55] B. R. Muir and D. W. O. Rogers, Monte Carlo calculations of k_Q , the beam quality conversion factor, *Med. Phys.* **37**, 5939 – 5950 (2010).
- [56] J. Wulff, J. T. Heverhagen, K. Zink, and I. Kawrakow, Investigation of systematic uncertainties in Monte Carlo-calculated beam quality correction factors, *Phys. Med. Biol.* **55**, 4481 – 4493 (2010).
- [57] B. R. Muir, M. R. McEwen, and D. W. O. Rogers, Beam quality conversion factors for parallel-plate ionization chambers in MV photon beams, *Med. Phys.* **39**, 1618 – 1631 (2012).
- [58] F. Erazo and A. M. Lallena, Calculation of beam quality correction factors for various thimble ionization chambers using the Monte Carlo code PENELOPE, *Physica Medica* **29**, 163 – 170 (2013).
- [59] K. Zink and J. Wulff, Beam quality corrections for parallel-plate ion chambers in electron reference dosimetry, *Phys. Med. Biol.* **57**, 1831–1854 (2012).
- [60] B. R. Muir and D. W. O. Rogers, Monte Carlo calculations for reference dosimetry of electron beams with the PTW Roos and NE2571 ion chambers, *Med. Phys.* **40**, 121722 (16pp) (2013).
- [61] K. Zink, D. Czarnecki, H. K. Looe, P. von Voigts-Rhettz, and D. Harder, Monte Carlo study of the depth-dependent fluence perturbation in parallel-plate ionization chambers in electron beams, *Med. Phys.* **41** (2014).
- [62] B. R. Muir and D. W. O. Rogers, Monte Carlo calculations of electron beam quality conversion factors for several ion chamber types, *Med. Phys.* **41**, 111701 (15pp) (2014).
- [63] F. Erazo, L. Brualla, and A. M. Lallena, Electron beam quality k_{Q,Q_0} factors for various ionization chambers: a Monte Carlo investigation with PENELOPE, *Phys. Med. Biol.* **59**, 6673 – 6691 (2014).

- [64] J. Pena, F. Sánchez-Doblado, R. Capote, J. A. Terrón, and F. Gómez, Monte Carlo correction factors for a Farmer 0.6 cm³ ion chamber dose measurement in the build-up region of the 6 MV clinical beam, *Phys. Med. Biol.* **51**, 1523 – 1532 (2006).
- [65] F. Salvat, J. M. Fernández-Varea, and J. Sempau, PENELOPE-2008: A Code System for Monte Carlo Simulation of Electron and Photon Transport, Technical report, OECD Nuclear Energy Agency, Issy-les-Moulineaux, France, 2008.
- [66] F. H. Attix, *Introduction to Radiological Physics and Radiation Dosimetry*, Wiley, New York, 1986.
- [67] H. E. Johns and J. R. Cunningham, *The physics of radiology*, 4th ed., Charles C. Thomas, Springfield, Illinois, 1983.
- [68] D. W. O. Rogers and J. E. Cygler, editors, *Clinical Dosimetry Measurements in Radiotherapy*, Medical Physics Publishing, Madison, Wisconsin, 2009.
- [69] A. E. Nahum, Cavity theory, stopping power ratios, correction factors, in *Clinical Dosimetry Measurements in Radiotherapy*, edited by D. W. O. Rogers and J. E. Cygler, Medical Physics Publishing, Madison, Wisconsin, 2009.
- [70] W. H. Bragg, *Studies in Radioactivity*, The Macmillan Co., London, 1912.
- [71] L. H. Gray, The absorption of penetrating radiation, *Proc. Roy. Soc.* **A122**, 647 – 668 (1929).
- [72] L. H. Gray, An ionization method for the absolute measurement of γ -ray energy, *Proc. Roy. Soc.* **A156**, 578 – 596 (1936).
- [73] D. W. O. Rogers, The physics of the AAPM's TG-51 protocol, in *Clinical Dosimetry Measurements in Radiotherapy*, edited by D. W. O. Rogers and J. E. Cygler, pages 239 – 296, Medical Physics Publishing, Madison, Wisconsin, 2009.
- [74] F. M. Khan, *The Physics of Radiation Therapy*, Lipincott Williams and Wilkins, Baltimore, Maryland, 3rd edition, 2003.
- [75] L. A. Buckley and D. W. O. Rogers, Wall correction factors, P_{wall} , for parallel-plate ionization chambers, *Med. Phys.* **33**, 1788 – 1796 (2006).

- [76] L. L. W. Wang and D. W. O. Rogers, Calculation of the replacement correction factors for ion chambers in megavoltage beams by Monte Carlo simulation, *Med. Phys.* **35**, 1747 – 1755 (2008).
- [77] L. L. W. Wang and D. W. O. Rogers, Study of the effective point of measurement for ion chambers in electron beams by Monte Carlo simulation, *Med. Phys.* **36**, 2034 – 2042 (2009).
- [78] P. R. Almond, P. J. Biggs, B. M. Coursey, W. F. Hanson, M. S. Huq, R. Nath, and D. W. O. Rogers, AAPM's TG-51 protocol for clinical reference dosimetry of high-energy photon and electron beams, *Med. Phys.* **26**, 1847 – 1870 (1999).
- [79] I. Kawrakow, On the effective point of measurement in megavoltage photon beams, *Med. Phys.* **33**, 1829 – 1839 (2006).
- [80] L. A. DeWerd, S. D. Davis, L. J. Bartol, and F. Grenzow, Ionization chamber instrumentation, in *Clinical dosimetry measurements in radiotherapy*, edited by D. W. O. Rogers and J. E. Cygler, Medical Physics Publishing, Madison, Wisconsin, 2009.
- [81] P. Andreo, A comparison between calculated and experimental k_Q photon beam quality correction factors, *Phys. Med. Biol.* **45**, L25 – L38 (2000).
- [82] M. Boutillon and A. M. Perroche-Roux, Re-evaluation of the W value for electrons in dry air, *Phys. Med. Biol.* **32**, 213 – 219 (1987).
- [83] J. Sempau, P. Andreo, J. Aldana, J. Mazurier, and F. Salvat, Electron beam quality correction factors for plane-parallel ionization chambers: Monte Carlo calculations using the PENELOPE system, *Phys. Med. Biol.* **49**, 4427 – 4444 (2004).
- [84] M. H. Kalos and P. A. Whitlock, *Monte Carlo methods*, Wiley, New York, 1986.
- [85] D. W. O. Rogers and A. F. Bielajew, Monte Carlo techniques of electron and photon transport for radiation dosimetry, in *The Dosimetry of Ionizing Radiation, Vol III*, edited by K. R. Kase, B. E. Bjärngard, and F. H. Attix, pages 427 – 539, Academic Press, 1990.
- [86] I. Kawrakow, Accurate condensed history Monte Carlo simulation of electron transport. I. EGSnrc, the new EGS4 version, *Med. Phys.* **27**, 485–498 (2000).

- [87] I. Kawrakow, On the efficiency of photon beam treatment head calculations, *Med. Phys.* **32**, 2320 – 2326 (2005).
- [88] B. R. B. Walters, I. Kawrakow, and D. W. O. Rogers, History by history statistical estimators in the BEAM code system, *Med. Phys.* **29**, 2745 – 2752 (2002).
- [89] I. Kawrakow, D. W. O. Rogers, and B. Walters, Large efficiency improvements in BEAMnrc using directional bremsstrahlung splitting, *Med. Phys.* **31**, 2883 – 2898 (2004).
- [90] E. S. M. Ali and D. W. O. Rogers, Efficiency improvements of x-ray simulations in EGSnrc user-codes using Bremsstrahlung Cross Section Enhancement (BCSE), *Med. Phys.* **34**, 2143 – 2154 (2007).
- [91] I. Kawrakow and B. R. B. Walters, Efficient photon beam dose calculations using DOSXYZnrc with BEAMnrc, *Med. Phys.* **33**, 3046 – 3056 (2006).
- [92] I. Kawrakow and M. Fippel, Investigation of variance reduction techniques for Monte Carlo photon dose calculation using XVMC, *Phys. Med. Biol.* **45**, 2163 – 2184 (2000).
- [93] D. Sheikh-Bagheri and D. W. O. Rogers, Variance reduction by selective bremsstrahlung splitting, *Med. Phys.* **23**, 808 (abstract) (1996).
- [94] D. Sheikh-Bagheri and D. W. O. Rogers, Selective bremsstrahlung splitting: A robust method to improve the efficiency of photon beam simulations of linacs, *Med. Phys.* (in preparation).
- [95] J. Ramos-Mendez, J. Perl, B. Faddegon, J. Schumann, and H. Paganetti, Geometrical splitting technique to improve the computational efficiency in Monte Carlo calculations for proton therapy, *Med. Phys.* **40**, 041718, 10pp (2013).
- [96] D. W. O. Rogers, B. A. Faddegon, G. X. Ding, C.-M. Ma, J. Wei, and T. R. Mackie, BEAM: A Monte Carlo code to simulate radiotherapy treatment units, *Med. Phys.* **22**, 503 – 524 (1995).
- [97] I. Kawrakow, E. Mainegra-Hing, F. Tessier, and B. R. B. Walters, The EGSnrc C++ class library, Technical Report PIRS-898 (rev A), National Research Council of Canada, Ottawa, Canada. <http://www.irs.inms.nrc.ca/EGSnrc/PIRS898/>, 2009.

- [98] J. Seuntjens and D. W. O. Rogers, Monte Carlo applications in measurement dosimetry, in *Clinical Dosimetry Measurements in Radiotherapy*, edited by D. W. O. Rogers and J. E. Cygler, pages 147 – 180, Medical Physics Publishing, Madison, Wisconsin, 2009.
- [99] M. J. Berger, Monte Carlo Calculation of the penetration and diffusion of fast charged particles, in *Methods in Comput. Phys.*, edited by B. Alder, S. Fernbach, and M. Rotenberg, volume 1, pages 135 – 215, Academic, New York, 1963.
- [100] J. M. Fernández-Varea, R. Mayol, J. Baró, and F. Salvat, On the theory and simulation of multiple elastic scattering of electrons, *Nuclear Instruments and Methods* **B73**, 447 – 473 (1993).
- [101] B. A. Faddegon, I. Kawrakow, Y. Kubyshev, J. Perl, J. Sempau, and L. aszlo Urban, The accuracy of EGSnrc, Geant4 and PENELOPE Monte Carlo systems for the simulation of electron scatter in external beam radiotherapy, *Phys. Med. Biol.* **54**, 6151 – 6163 (2009).
- [102] J. Sempau, E. Acosta, J. Baro, J. M. Fernandez-Varea, and F. Salvat, An algorithm for Monte Carlo simulation of coupled electron-photon transport, *Nucl. Inst. Meth. B* **132** (1997).
- [103] D. W. O. Rogers, I. Kawrakow, J. P. Seuntjens, B. R. B. Walters, and E. Mainegra-Hing, NRC user codes for EGSnrc, NRC Technical Report PIRS-702 (rev C), National Research Council of Canada, Ottawa, Canada. <http://www.irs.inms.nrc.ca/EGSnrc/PIRS702/>, 2011.
- [104] E. Mainegra-Hing, N. Reynaert, and I. Kawrakow, Novel approach for the Monte Carlo calculation of free-air chamber correction factors, *Med. Phys.* **35**, 3650 – 3660 (2008).
- [105] E. Mainegra-Hing and I. Kawrakow, Variance reduction techniques for fast Monte Carlo CBCT scatter correction calculations, *Phys. Med. Biol.* **55**, 4495 – 4507 (2010).
- [106] D. W. O. Rogers, B. Walters, and I. Kawrakow, BEAMnrc Users Manual, NRC Technical Report PIRS-509(A) revL, National Research Council of Canada, Ottawa, Canada. <http://www.irs.inms.nrc.ca/BEAM/beamhome.html>, 2011.

- [107] B. R. B. Walters and D. W. O. Rogers, DOSXYZnrc Users Manual, NRC Report PIRS 794 (2002).
- [108] L. A. Buckley, I. Kawrakow, and D. W. O. Rogers, CSnrc: correlated sampling Monte Carlo calculations using EGSnrc, *Med. Phys.* **31**, 3425 – 3435 (2004).
- [109] C.-M. Ma and A. E. Nahum, Calculation of absorbed dose ratios using correlated Monte Carlo sampling, *Med. Phys.* **20**, 1189 – 1199 (1993).
- [110] A. Badal and J. Sempau, A package of Linux scripts for the parallelization of Monte Carlo simulations, *Computer Physics Communications* **175**, 440 – 450 (2006).
- [111] G. Mora, A. Maio, and D. W. O. Rogers, Monte Carlo simulation of a typical ^{60}Co therapy source, *Med. Phys.* **26**, 2494 – 2502 (1999).
- [112] D. Sheikh-Bagheri and D. W. O. Rogers, Monte Carlo calculation of nine megavoltage photon beam spectra using the BEAM code, *Med. Phys.* **29**, 391 – 402 (2002).
- [113] N. I. Kalach and D. W. O. Rogers, Which accelerator photon beams are “clinic-like” for reference dosimetry purposes?, *Med. Phys.* **30**, 1546 – 1555 (2003).
- [114] E. G. A. Aird and F. T. Farmer, The design of a thimble chamber for the Farmer dosimeter, *Phys. Med. Biol.* **17**, 169 – 174 (1972).
- [115] M. J. Butson, P. K. N. Yu, and P. E. Metcalfe, Extrapolated surface dose measurements with radiochromic film, *Med. Phys.* **26**, 485 – 488 (1999).
- [116] I. Kawrakow, egspc: the EGSnrc C++ class library, Technical Report PIRS-899, National Research Council of Canada, Ottawa, Canada, 2005.
- [117] D. W. O. Rogers and C. L. Yang, Corrected relationship between $\%dd(10)_x$ and stopping-power ratios, *Med. Phys.* **26**, 538 – 540 (1999).
- [118] J. R. Cunningham and M. R. Sontag, Displacement corrections used in absorbed dose determinations, *Med. Phys.* **7**, 672 – 676 (1980).
- [119] K. A. Johansson, L. O. Mattsson, L. Lindborg, and H. Svensson, Absorbed-dose determination with ionization chambers in electron and photon beams

- having energies between 1 and 50 MeV, in *IAEA Symposium Proceedings*, pages 243 – 270, IAEA–SM–222/35, IAEA, Vienna, 1978.
- [120] M. S. Huq, P. Andreo, and H. Song, Comparison of the IAEA TRS-398 and AAPM TG–51 absorbed dose to water protocols in the dosimetry of high-energy photon and electron beams, *Phys. Med. Biol.* **46**, 2985 – 3006 (2001).
- [121] L. A. Buckley and D. W. O. Rogers, Wall correction factors, P_{wall} , for thimble ionization chambers, *Med. Phys.* **33**, 455 – 464 (2006).
- [122] M. R. McEwen, Measurement of ionization chamber absorbed dose k_Q factors in megavoltage photon beams, *Med. Phys.* **37**, 2179 – 2193 (2010).
- [123] D. W. O. Rogers, Fundamentals of Dosimetry Based on Absorbed-Dose Standards, in *Teletherapy Physics, Present and Future*, edited by J. R. Palta and T. R. Mackie, pages 319 – 356, AAPM, Washington DC, 1996.
- [124] E. Mainegra-Hing, I. Kawrakow, and D. W. O. Rogers, Calculations for plane-parallel ion chambers in ^{60}Co beams using the EGSnrc Monte Carlo code, *Med. Phys.* **30**, 179 – 189 (2003).